

UC San Diego

UC San Diego Electronic Theses and Dissertations

Title

First-Principles Investigations of Interfacial Dynamics in Nano-Materials

Permalink

<https://escholarship.org/uc/item/36p8q75q>

Author

Chen, Amanda Amy

Publication Date

2023

Peer reviewed|Thesis/dissertation

UNIVERSITY OF CALIFORNIA SAN DIEGO

First-Principles Investigations of Interfacial Dynamics in Nano-Materials

A Dissertation submitted in partial satisfaction of the requirements
for the degree Doctor of Philosophy

in

Chemical Engineering

by

Amanda Amy Chen

Committee in charge:

Professor Tod Pascal, Chair
Professor Joshua Figueroa
Professor Francesco Paesani
Professor Nicole Steinmetz
Professor Andrea Tao

2023

Copyright

Amanda Amy Chen, 2023

All rights reserved.

The Dissertation of Amanda Amy Chen is approved, and it is acceptable in quality and form for publication on microfilm and electronically.

University of California San Diego

2023

TABLE OF CONTENTS

DISSERTATION APPROVAL PAGE.....	iii
TABLE OF CONTENTS.....	iv
LIST OF FIGURES.....	viii
LIST OF TABLES.....	xi
LIST OF ABBREVIATIONS.....	xii
ACKNOWLEDGEMENTS.....	xiv
VITA.....	xvi
PUBLICATIONS.....	xvii
ABSTRACT OF THE DISSERTATION.....	xviii
CHAPTER 1 : General Introduction.....	1
1.1. PREFACE.....	1
1.2. RESEARCH MOTIVATION AND INTRODUCTION.....	1
CHAPTER 2 : Computations Overview.....	4
2.1. MOLECULAR DYNAMICS (MD).....	4
2.2. QUANTUM MECHANICS (QM).....	5
2.3. GRAND CANONICAL MONTE CARLO (GCMC).....	6
CHAPTER 3 : The Phase Diagram of Carbon Dioxide from Correlation Functions and a Many-body Potential.....	8
3.1. ABSTRACT.....	8
3.2. INTRODUCTION.....	9
3.3. THEORETICAL APPROACH BACKGROUND.....	11
3.3.1. Two-Phase Thermodynamic (2PT) Method for rapid evaluation of the Entropy and Gibbs Energy.....	11
3.3.1.1. Calculation of the Density of State (DoS) function.....	13

3.3.1.2. Obtaining Thermodynamic Properties from the 2PT Method.....	14
3.3.2. Partial atomic charges from the Charge Equilibration (QEq) Method.....	17
3.4. COMPUTATIONAL DETAILS.....	20
3.4.1. Description of Initial Systems.....	20
3.4.2. The Flexible-EPM2 Carbon Dioxide Forcefield.....	20
3.4.3. FEPM2 Molecular Dynamics Simulations.....	21
3.4.4. FEPM2 Thermodynamics of the Solid and Liquid Phases.....	22
3.4.5. FEPM2 Thermodynamics of the Gas Phase.....	22
3.4.6. Construction of the CO ₂ -Fq Forcefield.....	23
3.4.7. CO ₂ -Fq MD Solid/Liquid Simulations and Thermodynamics.....	27
3.4.8. CO ₂ -Fq Thermodynamics of the Gas Phase.....	28
3.4.9. Determination of the Phase Boundaries.....	29
3.4.10. Determining the Critical Point from the Vapor-Liquid Coexistence curve.....	29
3.5. RESULTS AND DISCUSSION.....	30
3.5.1. Molecular charge distribution in the condensed phase using the CO ₂ -Fq model.....	30
3.5.2. Spectral Density function of CO ₂	32
3.5.3. The Thermodynamic Properties of Carbon Dioxide.....	34
3.5.3.1. Thermodynamics of Crystalline CO ₂	34
3.5.3.2. Carbon Dioxide Thermodynamic properties at Vapor-Liquid Coexistence (VLE) conditions and Critical Point.....	37
3.5.4. The Carbon Dioxide Phase Diagram based on phase stability and the 2PT method...40	
3.6. CONCLUSIONS AND OUTLOOK.....	43
3.7. ACKNOWLEDGEMENTS.....	44
CHAPTER 4 : Sub-Nanometer Confinement Enables Facile Condensation of Gas Electrolyte for Low-Temperature Batteries.....	45
4.1. ABSTRACT.....	45
4.2. INTRODUCTION.....	46
4.3. THEORETICAL AND COMPUTATIONAL ANALYSIS.....	48

4.3.1. Computational Investigation.....	48
4.3.2. Computational Details.....	56
4.3.2.1. Grand Canonical Monte-Carlo (GCMC) simulations in determining the loading curves.....	56
4.3.2.2. MD simulations of FM/UiO-66 and UiO-66 systems.....	56
4.3.2.3. MD simulations of bulk FM systems.....	57
4.3.2.4. Self-diffusion constant.....	57
4.4. EXPERIMENTAL ANALYSIS.....	58
4.4.1. The adsorption behavior of FM in UiO-66.....	58
4.4.2. Electrochemical properties of MOF-polymer membranes (MPM) in liquefied FM solution.....	59
4.4.3. Cell performance with MPM confined FM electrolyte.....	62
4.5. CONCLUSION.....	64
4.6. ACKNOWLEDGEMENTS.....	65
CHAPTER 5 : Curvature-Selective Nanocrystal Surface Ligation Using Sterically-Encumbered Metal-Coordinating Ligands.....	66
5.1. ABSTRACT.....	66
5.2. INTRODUCTION.....	67
5.3. THEORETICAL AND COMPUTATIONAL ANALYSIS.....	69
5.3.1. Investigation of CNAr ^{Mes2} on Au.....	69
5.3.2. Investigation of CNXyl, CNAr ^{Dipp2} , and CNAr ^{Tripp2} on Au.....	73
5.3.3. Computational Details.....	76
5.3.3.1. Parameterization of the ligand C≡N/AuNS Interactions.....	77
5.3.3.2. Description of Systems in MD Simulations.....	82
5.3.3.3. Equilibrium MD Simulations and Vibrational Spectral Analysis.....	83
5.3.3.4. Radial Distribution Function Analysis.....	85
5.3.3.5. Ligand Solvation Free Energy Calculations.....	85
5.3.3.6. Free Energy of Isocyanide Binding to Solvated AuNSs.....	86

5.3.3.7. Computation of Normalized Descriptors.....	87
5.4. EXPERIMENTAL ANALYSIS.....	88
5.4.1. Investigation of selective binding by m-terphenyl-based anchoring groups.....	88
5.4.2. Investigation of liquid-liquid extraction (LLE).....	90
5.5. CONCLUSIONS.....	92
5.6. ACKNOWLEDGMENTS.....	92
CHAPTER 6 : Conclusion.....	94
REFERENCES.....	95

LIST OF FIGURES

- Figure 3.1** The distribution of molecular charges using the CO₂-Fq forcefield for (a) a solid and (b) a liquid at 100atm, 240K. The simulation data (solid lines) are fitted to Gaussian functions (dashed green lines). The dashed black lines indicate the standard deviations (solid: $1\sigma = 0.028$; liquid: $1\sigma = 0.034$). 31
- Figure 3.2** The dielectric constant values of 0.5 ns simulation of liquid CO₂ (240K and 100atm) using (a) the CO₂-Fq forcefield and (b) the FEPM2 forcefield. The experimental dielectric constant at these conditions is ~ 1.5 31
- Figure 3.3** The CO₂ total VAC function of (a) FEPM2 solid/liquid density systems at 240K, 100atm, (b) FEPM2 gas density system at 1atm, 250K and (c) CO₂-Fq solid/liquid density systems at 240K, 100atm. The zoomed inset of (c) demonstrates the VAC function details within 0 – 4 ps. 33
- Figure 3.4** The per-molecule CO₂ DoS functions of (a) translational, (b) rotational, and (c) vibrational motion for FEPM2 model and the CO₂-Fq model (d, e and f respectively), for the liquid at 240K and 100atm. 33
- Figure 3.5** Probability distribution of the C-O bond lengths of crystalline CO₂ from equilibrium MD simulations at 150 – 180K and 1atm, using the FEPM2 (a) and CO₂-Fq (b) forcefields. We fit the simulation data (solid lines) to Gaussian functions (dashed lines). 37
- Figure 3.6** (a) The density – temperature relationship along the VLE curve and the critical point of CO₂ simulated with the FEPM2 and CO₂-Fq models (solid data points). Dashed curves are cubic spline fits to the calculated data. (b) The translational (trans) and the rotational (rot) fluidicity factors of FEPM2 model along the VLE curve. 38
- Figure 3.7** The thermodynamics of CO₂ described by the FEPM2 and CO₂-Fq models at 100atm as the system undergoes a 1st order phase transition. 41
- Figure 3.8** The CO₂ phase diagram, based on the Gibbs energy of the isolated solid, liquid and gas phases, using the FEPM2 (a) and the CO₂-Fq (b) models. 42
- Figure 4.1** Schematic showing the mechanism of nano-confinement effects for lowering the equilibrium pressure of liquefied gas, where MOFs were employed as the porous hosts to condense the gas molecules under a lower P_v than P_{sat} , attributed to the driving force of the sub-nanometer confinement of MOFs.[137] 47
- Figure 4.2** Schematic showing the adsorption behavior of FM in UiO-66 at different conditions. 49

Figure 4.3 Simulation structure of UiO-66. The simulation structure for (a) UiO-66, compositing of (b) $[\text{Zr}_6\text{O}_4(\text{OH})_4]$ clusters and (c) BDC linkers.	52
Figure 4.4 Simulated adsorption isotherms of UiO-66 confined CH_4 and CO_2 at room temperature, compared to other published data.[149, 150] We find overall excellent agreement with published data, validating our current simulation approach.	52
Figure 4.5 Simulated (SIM) adsorption isotherms of UiO-66 confined FM at different temperatures and experimental (EXP) results at 25 °C.....	53
Figure 4.6 The densities comparison between adsorbed FM inside UiO-66 and free FM in bulk FM systems. The solid curves represent the FM densities inside UiO-66 and the dashed curves indicate the bulk FM densities, at the stated temperatures.	53
Figure 4.7 Simulated translational diffusion coefficients. Simulated translational diffusion coefficients of (a) bulk FM, and (b, c, d) adsorbed FM (ads. FM) in UiO-66 at different temperatures and pressures.	54
Figure 4.8 Phase transition comparison between bulk FM taken from NIST database, simulated (SIM) bulk FM and simulated (SIM) adsorbed (ads.) FM in UiO-66 systems, where the orange and the red points represent as the phase transitions of bulk FM and adsorbed FM (ads. FM) in UiO-66, respectively.	55
Figure 4.9 Mass change of liquefied FM soaked UiO-66.....	59
Figure 4.10 Electrochemical properties of MPM-based LGE..	61
Figure 4.11 Cell performance of Li// CF_x cells.....	63
Figure 4.12 Nyquist impedance. Nyquist impedance of Li// CF_x cells mixed with 20 wt. % UiO-66 using Celgard and MPM at (a) vapor pressure and (b) 70 psi at -40 °C.....	64
Figure 5.1 Nanocurvature selectivity enabled by surface-ligand sterics.	68
Figure 5.2 $\text{CNAr}^{\text{Mes}_2}$ binding to Au nanocrystals.	70
Figure 5.3 Initial AuNS structure used in MD simulations. The diameter is ~5 nm and edge length, L, is ~1.7 nm. The distances from the AuNS center of mass to the Au(001) surfaces, the Au(111) surfaces, the Au(001/111) edges, the Au(111/111) edges, and the corners of Au(001/111/111) facets, are 24.5 Å, 21.5 Å, 26 Å, 26 Å, 27 Å, respectively.....	71
Figure 5.4 Free energy of binding of $\text{CNAr}^{\text{Mes}_2}$ to (a) Au(001) slab and (b) Au(curved) slab. All calculations employed Metadynamics accelerated sampling in CHCl_3 at 298K. The	

distance, Z, was computed between the carbon of $\text{CNAr}^{\text{Mes}2}$ $\text{C}\equiv\text{N}$ group and the bottom of the Au-slab (Z coordinate = 0 Å).....	72
Figure 5.5 (a) Initial snapshot of 64 $\text{CNAr}^{\text{Mes}2}$ molecules randomly distributed in a box containing 4484 water molecules (red) and 1096 CHCl_3 molecules (blue). (b) Final snapshot after equilibrium MD simulation at 298K and 1atm, showing $\text{CNAr}^{\text{Mes}2}$ ligands transferring to the organic CHCl_3 phase.	72
Figure 5.6 Surface-ligand steric pressure by design.	74
Figure 5.7 Final snapshot from equilibrium MD simulations in vacuum at 298K of (left to right) CNXyl , $\text{CNAr}^{\text{Dipp}2}$, $\text{CNAr}^{\text{Tripp}2}$ on a 5nm AuNS.....	82
Figure 5.8 Simulated $\text{C}\equiv\text{N}$ vibrational spectrum of $\text{CNAr}^{\text{Mes}2}$ as a free molecule in CHCl_3 (green) and as a bound-molecule to the AuNSs surface (blue)..	84
Figure 5.9 Experimental investigation on nanocurvature selectivity by surface-ligand sterics..	89
Figure 5.10 Size-selective LLE of AuNS dispersions.	91

LIST OF TABLES

Table 3.1 FEPM2 force field parameters for CO ₂	21
Table 3.2 The intra-molecular energies of CO ₂	24
Table 3.3 The inter-molecular binding energies of the CO ₂ dimer.....	26
Table 3.4 CO ₂ -Fq forcefield parameters.	27
Table 3.5 CO ₂ vibration frequencies from experiment and FEPM2/CO ₂ -Fq MD simulations....	34
Table 3.6 Equations and data used for thermodynamic properties calculation. Empirical thermodynamic data from References [90, 104].....	35
Table 3.7 The thermodynamic properties of crystalline CO ₂ at 1 atm, 50K/100K/150K. The subscripts of trans, rot, and vib represent as the translation, rotation, and vibration modes of 2PT, respectively. S _q is the quantum entropy obtained from 2PT analysis.....	36
Table 3.8 Thermodynamic properties of CO ₂ along the VLE curve using the FEPM2 and CO ₂ -Fq models compared to experiments.....	39
Table 4.1 Simulation parameters applied in MD/GCMC computations.....	49
Table 4.2 Quantification of ionic conductivity value comparison between MPM and commercial Celgard membranes at different pressures at -40°C.....	62
Table 5.1 Solvation free energies difference of various Isocyanide ligands in CHCl ₃ and water, and cohesive free energy (self-solvation energy) from Free Energy Perturbation calculations.	75
Table 5.2 Values of computational descriptors for various isocyanide ligands.....	75
Table 5.3 The CNXyl, CNAr ^{Dipp2} , CNAr ^{Tripp2} , and CNAr ^{Mes2} - gold interaction energies via QM calculations.	78
Table 5.4 Composition of simulation cells used in various MD simulations. The associated figures are indicated.	82
Table 5.5 Simulated and experimental isocyanide stretching frequencies, $\nu(\text{CN})$, of Au-bound and free CNAr ^{Mes2}	84

LIST OF ABBREVIATIONS

The following Table demonstrates the abbreviations defined in this dissertation.

Abbreviation	Meaning
LAMMPS	Large-scale Atomic/Molecular Massively Parallel Simulator
QE	Quantum Espresso
CO ₂	Carbon Dioxide
QEq theory	Charge Equilibration theory
MOFs	Metal-Organic frameworks
FM	fluoromethane
MPMs	MOF-polymer membranes
MD	molecular dynamics
2PT	Two-Phase Thermodynamics
FEPM2	flexible Elementary Physical Model 2
QM	quantum mechanics
SCCO ₂	supercritical carbon dioxide
EPM2	Elementary Physical Model 2
DoS	Density of States
PD	point dipole
FC	fluctuating charge
VLE	vapor-liquid coexistence
LJ	Lennard-Jones
CG	conjugated gradient
UNB	universal nonbonded
GLE	Generalized Langevin equation
f-factor	fluidicity-factor
trans	translation

rot	rotation
vib	vibration
LIBs	lithium-ion batteries
LGE	liquefied gas electrolytes
FTIR	Fourier transform-infrared
GCMC	Grand Canonical Monte-Carlo
EC	ethylene carbonate
DEC	diethyl carbonate
EMC	ethyl methyl carbonate
CF _x	Fluorinated graphite
Nano-CT	nano-computed tomography
AuNSs	Gold Nanospheres
CNAr ^{Mes2}	Ar ^{Mes2} = 2,6-(2,4,6-Me ₃ C ₆ H ₂) ₂ C ₆ H ₃
TEM	Transmission electron microscopy
OD	optical density
CNXyl	2,6-dimethylphenyl isocyanide
LLE	liquid-liquid extraction
CNAr ^{Dipp2}	Ar ^{Dipp2} = 2,6-(2,6-(<i>i</i> -Pr) ₂ C ₆ H ₃) ₂ C ₆ H ₃); <i>i</i> -Pr = <i>iso</i> -propyl
CNAr ^{Tripp2}	Ar ^{Tripp2} = 2,6-(2,4,6-(<i>i</i> -Pr) ₃ C ₆ H ₂) ₂ C ₆ H ₃
SBR	site-binding ratio
EBF	edge-binding factor
SF	solubility factor
SPF	solvent partition factor
ZPE	zero-point energy
SERS	surface-enhanced Raman spectroscopic
FEP	Free Energy Perturbation

ACKNOWLEDGEMENTS

I would like to express my great gratitude on my thesis advisor, Prof. Tod Pascal, for his support of the computational modeling and the theoretical instruction. His suggestions inspire my imagination and motivation on my individual study. Besides, I would also like to thank our ATLAS research group coworkers, Pedram Abbasi, Sasawat Jamnuch, Robert Ramji, and Alexandria Do, for their support and brainstorm in developing computational skills on various academic areas.

I am grateful to the University of California San Diego - Materials Research Science and Engineering Center (MRSEC). MRSEC provides opportunities for me to collaborate with the lab teams of Prof. Andrea Tao, Prof. Joshua Figueroa, Prof. Zheng Chen, and Prof. Jesse Jokerst. I want to put special thanks for Yufei Wang, Krista Balto, Guorui Cai, and Jiajing Zhou, the corresponding lab members from the collaborative groups. Due to the collaboration, more in-depth research studies can be adopted and explored.

Chapter 3, in full, is a modified version of the published materials – Amanda A. Chen, Alexandria Do, and Tod A. Pascal. “The Phase Diagram of Carbon Dioxide from Correlation Functions and a Many-body Potential” (2021), on The Journal of Chemical Physics. The dissertation author is the primary author who conducts the investigation and analyzation on this work.

Chapter 4, in full, is a modified version of the published materials - Guorui Cai, Yijie Yin, Dawei Xia, Amanda A. Chen, John Holoubek, Jonathan Scharf, Yangyuchen Yang, Ki Hwan Koh1, Mingqian Li, Daniel M. Davies, Matthew Mayer, Tae Hee Han, Ying Shirley Meng, Tod A. Pascal, and Zheng Chen. “Sub-Nanometer Confinement Enables Facile Condensation of Gas

Electrolyte for Low-Temperature Batteries” (2021), on Nature Communications. The dissertation author is the primary researcher who leads the computational analysis in this work.

Chapter 5, in full, is a modified version of the published materials - Yufei Wang*, Amanda A. Chen*, Krista P. Balto*, Yu Xie, Joshua S. Figueroa, Tod A. Pascal, and Andrea R. Tao. “Curvature-Selective Nanocrystal Surface Ligation Using Sterically-Encumbered Metal-Coordinating Ligands” (2022), on ACS Nano. The dissertation author is the co-first author who conducts the computational investigation on this work.

VITA

2018 - Present *University of California San Diego*

Doctor of Philosophy, Chemical Engineering

2017 - 2018 *University of California San Diego*

Master, Chemical Engineering

2013 - 2017 *National Cheng Kung University*

Bachelor, Chemical Engineering

PUBLICATIONS

H. Liu, J. Holoubek, H. Zhou, A. Chen, N. Chang, Z. Wu, S. Yu, Q. Yan, X. Xing, Y. Li, T.A. Pascal, P. Liu. “Ultra-high coulombic efficiency electrolyte enables Li||SPAN batteries with superior cycling performance”, *Materials Today*, 42, 17-28. (2021)

G. Cai, Y. Yin, D. Xia, A.A. Chen, J. Holoubek, J. Scharf, Y. Yang, K.H. Koh, M. Li, D.M. Davies, M. Mayer, T.H. Han, Y.S. Meng, T.A. Pascal, and Z. Chen. “Sub-Nanometer Confinement Enables Facile Condensation of Gas Electrolyte for Low-Temperature Batteries”, *Nature Communications*, 12(1), 1-11 (2021)

J. Zhou, M.N. Creyer, A. Chen, W. Yim, R.P.M. Lafleur, T. He, Z. Lin, M. Xu, P. Abbasi, J. Wu, T.A. Pascal, F. Caruso, and J.V. Jokerst. “Stereoselective growth of small molecule patches on nanoparticles” *Journal of the American Chemical Society*, 143(31), 12138-12144 (2021)

A.A. Chen, A. Do, T.A. Pascal. “The Phase Diagram of Carbon Dioxide from Correlation Functions and a Many-body Potential”. *The Journal of Chemical Physics*, 155(2), 024503. (2021)

J. Holoubek, K. Kim, Y. Yin, Z. Wu, H. Liu, M. Li, A. Chen, H. Gao, G. Cai, T.A. Pascal, P. Liu, and Z. Chen. “Electrolyte Design Implications of Ion-Pairing in Low-Temperature Li Metal Batteries”, *Energy & Environmental Science*, 15(4), 1647-1658. (2022)

Y. Wang*, A.A. Chen*, K.P. Balto*, Y. Xie, J.S. Figueroa, T.A. Pascal, and A.R. Tao, “Curvature-Selective Nanocrystal Surface Ligation Using Sterically-Encumbered Metal-Coordinating Ligands”, *ACS Nano*, 16(8), 12747-12754. (2022)

ABSTRACT OF THE DISSERTATION

First-Principles Investigations of Interfacial Dynamics in Nano-Materials

by

Amanda Amy Chen

Doctor of Philosophy in Chemical Engineering

University of California San Diego, 2023

Professor Tod Pascal, Chair

Most scenarios in our daily life can be related to thermodynamic principles. The investigation of thermodynamic phenomena, including heat transfer, chemical reactions, and dynamics, are explored to develop various appliances that play a fundamental role in our current lives. Therefore, thermodynamics are the foundation of our modern life framework.

However, it is impractical to “manually” put all thermodynamic theories together to predict the outcomes. Therefore, computer simulations have been developed to simulate those complicated models for practical applications. In this research study, we used computer simulations with core thermodynamic disciplines to resolve the challenges encountered in the industry and also the threat from climate change. With the lab collaboration, this work provided not only the theoretical consequences but also the experimental supports in practical uses.

Along with the computational and experimental bases, we explored the fields on generating the appropriate forcefield models, investigating the materials characteristics inside the Metal-Organic frameworks, and analyzing the curvature-selective ligand adsorption toward nanoparticles. Considerations of larger systems applied in real life are a natural extension, and insights on the behavior of theoretical functions are being explored.

CHAPTER 1 : General Introduction

1.1. Preface

Thermodynamic principles are the backbone of daily human life. The behavior of systems from as small as a nanoparticle to as large as the universe can be attributed to the correlation between thermodynamic rules. With conceptual understanding of the theoretical connection between the thermodynamics and the corresponding phenomenon, it is possible for researchers to predict the spontaneity, the yield, the optimized operation conditions, etc. of a process via computational approaches.

Instead of building a real instrument and paying for chemicals, computational simulations provide a relatively low-cost and safe approach to investigate a process and explore a solution to a scenario. Software packages such as Large-scale Atomic/Molecular Massively Parallel Simulator (LAMMPS) [1], Q-Chem 5.2 [2], Quantum Espresso (QE) [3, 4], etc. are developed to simulate a system performance via the molecular interactions, dynamics, and electronic structures.

This research work centers on the investigation of nanoscale system characteristics via the thermodynamics disciplines using computational simulations. The research flow is built from a single-component system (Chapter3) to a multi-component system (Chapter4 and Chapter5), providing a trend from broad foundations into specific frameworks.

1.2. Research Motivation and Introduction

This research study is motivated from the concerns on the growing threat of climate change and the challenges encountered in the industrial development, such as efficient battery design and

selective adsorption control toward nanoparticles. Here, computer simulations with a thermodynamics backbone are adopted to provide insights on the theoretical scenarios and to explore the strategic foresight on mapping out the future.

From the threat of global warming, the characteristics of greenhouse gases, especially Carbon Dioxide (CO₂), draw attention from researchers. Environmentally, the growing levels of CO₂ has been found to be a dominate impact factor on global warming phenomenon. [5, 6] Industrially, CO₂'s non-toxic, recyclable, and cheap properties allow it to be widely applied as an extracting solvent, anti-solvent, solvent to homogenize systems, etc. [7-12] To appropriately simulate CO₂ characteristics, we generated a CO₂ forcefield with many-body potential and Charge Equilibration (QEq) theory [13], which demonstrated good agreement with experimental / theoretical data, as detailed in Chapter3.

Despite the buildup of an appropriate forcefield for CO₂, climate change is a much more complicated process in reality. The removal of heat-trapping gases can be proceeded via physical or chemical approaches, which have been investigated by scientists using modern technology. To date, gases capture/storage and energy conversion/storage techniques using such the high-selectivity Metal-Organic framework membranes[14-16], electrochemical catalysts[17, 18], nanoparticles[19, 20], etc. catch growing attention not only toward the removal of greenhouse gases, but also on the reduction of greenhouse gases amount released from human daily life. This implies that in addition to characterizing a single-component system (Chapter3), it is also critical to examine the multi-component cases to put models in practical uses.

To directly reduce the amount of heat-trapping gases released from daily human life, efforts have been made to improve the energy conversion/storage technology in batteries. The more

efficient energy conversion and storage, the lower amount of undesired side products that will be emitted to atmosphere. Therefore, the investigation of the battery compositions/materials becomes critical to improve the battery performance. One novel approach applied in the battery design is to adopt Metal-Organic frameworks (MOFs) in the battery cell. Benefits of MOFs' tunable pore size, uniform pore environment, and controllable integration [21, 22], MOFs has been widespread used in the industry. In Chapter4, a study of MOFs-based membranes was investigated, and the results revealed that the fluoromethane (FM), which was introduced as the liquefied gas electrolyte, was well-confined inside MOFs and thus the possible explosion of a battery was avoided. Besides, as a type of heat trapping gas, the use of FM provides a possible solution to convert the undesired gas in atmosphere into the major chemicals in the energy conversion/storage devices. Moreover, due to the chemical properties of FM, the battery was able to be operated at even low-temperature.

On the other hand, the investigation of nanoparticles is also pivotal in wide applications, such as the CO₂ electrochemical reduction process[19], recyclable catalysts uses [23], drug delivery fields [24], etc. However, there are challenges in the control of membrane design with nanoparticles. Therefore, in Chapter5, we explored the curvature-selective adsorption characteristic of ligands on nanoparticles via controlling the ligand steric effect, which can be further applied to control the nanoparticle assembly and provide insight into nanoparticle-based designs.

Combined, this research work investigated both environmental and industrial challenges via computational approaches with a thermodynamic backbone. Besides the computer simulations, experimental data, collected from the collaboration with Prof. Andrea Tao, Prof. Joshua Figueroa, and Prof. Zheng Chen, strengthened this research work on practical uses.

CHAPTER 2 : Computations Overview

2.1. Molecular Dynamics (MD)

Molecular Dynamics (MD) simulation, which was first introduced using simple gases by Alder and Wainwright [25], and further adopted in a protein case by McCammon et al. [26], is an approach to investigate atoms/molecules motions of a system. Studies in MD simulations have since been developed in lots of fields, such as drug delivery [27], fundamental adsorption [28], and battery electrolyte [29], etc. As a widely used tool in analyzing the systemic dynamics, efforts have been put to enhance the MD simulation performance via Machine Learning (ML) [30] technology, which allows a reduction in the runtime with a factor of ~10 using OpenMPI, ~100 using MPI, and ~400 using a hybrid OpenMPI/MPI condition. The improvement in the efficiency enables scientists to explore the molecular motions in a relatively short time via MD simulations.

Prior proceeding a MD model, the natural properties of atoms and the corresponding inter-/intra- molecular characteristics (mass, bond, angle, dihedral, improper, and van der Waals (VDW) interaction, etc.), so called “forcefield”, must be known. Studies have been done for developing forcefields in most materials - such as the Universal forcefield (UFF) [31], Amber forcefield [32], and DREIDING forcefield [33]. In addition, forcefields for specific chemicals – such as TIP3P forcefield in water [34] and EPM2 forcefield in Carbon Dioxide (CO₂) [35] have been developed as well. Besides, it is noted that the results of a MD model are not only relevant to the materials properties, but also relevant to the systemic conditions. A MD model is supposed to be done with sufficient duration time to well-reproduce the natural processes. In addition, the cell size of a MD model must be appropriate, which is large enough to ensure the interactions to be well-modeled

and is small enough to avoid high cost in computation time. With better understandings of the MD models, relatively fast and accurate simulations can be done.

In this research work, we first introduced the procedure to generate an appropriate forcefield and the accuracy was confirmed by the MD simulations using various systemic conditions in different circumstances (Chapter 3). In Chapter 4 and Chapter 5, we adopted the MD simulations to provide insight on multi-component systems and the results were consistent with the experimental findings. In brief, MD simulations are able to describe the material properties and explore the molecular motions in Nano-Materials.

2.2. Quantum Mechanics (QM)

Quantum Mechanics (QM) adopts fundamental concepts of atoms to explain the behavior of a system and is attributed to the diffraction, coherence, and discreteness phenomena. [36] The diffraction phenomenon is relevant to the characteristics of wave functions, which had been illustrated by Davisson and Germer in 1927 toward the electrons scattering analysis [37] and by L. de Broglie's theoretical conjecture on electrons.[38] Coherence is a concept relevant to the phase stability and can be connected to the coherence vector in photons.[39] Discreteness, which is the phenomena where QM derives its name, describes properties by a set of discrete values. The discreteness phenomenon was first established by Franck and Hertz toward the discreteness of atom energy levels [40], which was further explained by P.M. Koch et al.'s study in analyzing the hydrogen atomic states. [41]

With the theoretical features, QM computations are able to provide the probabilities on whether a phenomenon will happen in a system. A particle's wave function, which is associated

with the probability amplitude for each points in a space, can be hybridized with mathematical formulas and principles, such as Schrödinger equation [42], M. Born's statistical interpretation [43], and Fourier transforms [44], etc. to describe the state of a system. To date, a wide range of studies have been investigated using QM principles and were applied in the laser [45], electron microscope [46], and magnetic resonance imaging (MRI) [47], etc. fields. Moreover, the combination between QM computations and artificial intelligence (AI) provides a direction for future work. [48]

In following chapters, we adopted QM computations in generating the forcefield for MD simulations (Chapter 3), analyzing the fluoromethane (FM) characteristics (Chapter 4), and determining the inter-/intra-molecular forces (Chapter 5). Results revealed that QM computations provided reasonable data in investigating the behavior of molecules in a model. Furthermore, with proper parameterization using QM data, MD simulations were able to show the consistency with experiments.

2.3. Grand canonical Monte Carlo (GCMC)

Grand canonical Monte Carlo (GCMC) simulation is a tool to investigate the number of molecules inside a simulation cell at a specific condition by defining constant values toward volume (V), temperature (T), and chemical potential (μ) properties. As a statistical mechanism, GCMC is relevant to a series of attempts on the deletion and insertion of a molecule between a reservoir and a system. In a GCMC process, the properties of the system for each attempt in inserting/deleting a molecule into/from a simulation cell is computed, and the result is further used to determine whether the rejection or the acceptance of the attempt will be adopted. Equilibrium

is achieved once the attempt to inset/delete a molecule into/from a system is less favorable, at which the number of molecules at a specific condition is determined.

In brief, GCMC simulation investigates the adsorption process of a system. By employing GCMC, a wide range of fields relevant to the adsorption phenomenon, such as the hydrogen physisorption on nanotubes [49], the carbon capture using Metal-Organic frameworks (MOFs) [50], and the removal of hydrogen sulfide (H_2S) from streams by zeolites [51], etc. , can be explored. In addition, with the proper control in GCMC and the selection of materials, the simulation can also provide insight on the selectivity characteristics at various conditions. [52]

In Chapter 4, GCMC simulations were applied to determine the adsorption capacity of fluoromethane (FM), carbon dioxide (CO_2), and methane (CH_4), in Metal-Organic frameworks (MOFs). Based on the GCMC optimized loading data, the translational diffusion coefficients were further calculated via MD simulations. Both GCMC and MD results revealed the volatile molecules are well-confined inside the MOFs, suggesting a future direction on the MOFs development.

CHAPTER 3 : The Phase Diagram of Carbon Dioxide from Correlation Functions and a Many-body Potential

Chapter3 was reproduced from A.A. Chen, A. Do, T.A. Pascal. “The Phase Diagram of Carbon Dioxide from Correlation Functions and a Many-body Potential”. *The Journal of Chemical Physics*, 155(2), 024503. (2021), with the permission of AIP Publishing.

3.1. Abstract

The phase stability and equilibria of carbon dioxide are investigated from 125–325 K and 1–10000 atm using extensive molecular dynamics (MD) simulations and the Two-Phase Thermodynamics (2PT) method. We devise a direct approach for calculating phase diagrams, in general, by considering the separate chemical potentials of the isolated phase at specific points on the P–T diagram. The unique ability of 2PT to accurately and efficiently approximate the entropy and Gibbs energy of liquids allows for assignment of phase boundaries from relatively short (~ 100 ps) MD simulations. We validate our approach by calculating the critical properties of the flexible elementary physical model 2, showing good agreement with previous results. We show, however, that the incorrect description of the short-range Pauli force and the lack of molecular charge polarization lead to deviations from experiments at high pressures. We, thus, develop a many-body, fluctuating charge model for CO₂, termed CO₂-Fq, from high level quantum mechanics (QM) calculations that accurately capture the condensed phase vibrational properties of the solid (including the Fermi resonance at 1378 cm^{-1}) as well as the diffusional properties of the liquid, leading to overall excellent agreement with experiments over the entire phase diagram. This work

provides an efficient computational approach for determining phase diagrams of arbitrary systems and underscores the critical role of QM charge reorganization physics in molecular phase stability.

3.2. Introduction

Carbon dioxide is an essential chemical, both environmentally and industrially. Human driven climate change has been largely attributed to the growing concentration of CO₂ in the atmosphere[53]: data from the Intergovernmental Panel on Climate Change and research studies [5, 6] indicate that CO₂ has the highest Radiative Forcing value, and is the greatest contributor to global warming and the greenhouse effect. Industrially, there is widespread use of supercritical carbon dioxide (SCCO₂), which has superior mass transfer properties, is non-toxic, cheap, and easy to recycle.[7] In heavy metal extraction, SCCO₂ is widely applied as the extracting solvent due to its high removal efficiency.[8] In the synthesis of Rhodium, Silver, and Copper nanoparticles, SCCO₂ provides a unique environment to homogenize these systems.[9-11] Additionally, SCCO₂ can serve as a highly selective anti-solvent in polymer synthesis, since most organic solvents show high mutual solubility with SCCO₂. [12]

In all these industrially and environmental processes, knowledge of the chemical and physical properties of CO₂ at various temperature / pressure conditions is essential, especially at extreme (high temperature and pressure) conditions. Experimental studies at these extreme conditions usually involve shock experiments,[54-56] yet these are challenging to perform in a laboratory setting as it requires highly specialized equipment. Computer simulations, employing Molecular Dynamics (MD) and/or Monte-Carlo approaches, are complementary techniques that are in principle more straightforward to perform than experiments. These simulations have been

aided by the development of efficient, empirical forcefields, fitted to reproduce the properties of homogenous phases, as well as phase equilibria. Of particular note is the Elementary Physical Model 2 (EPM2),[57] which was developed to predict the liquid-vapor coexistence curve and critical properties of CO₂. The performance of the EPM2 over the entire phase diagram has not previously been reported, however.

Evaluating of the entire phase diagram is important since it is the ultimate metric for determining the accuracy and transferability of interaction potentials. Various computational approaches have been employed to meet this challenge, ranging from simulations in the Gibbs ensemble,[58] calculations of the latent heat across the phase boundaries and application of the Clausius-Clapeyron equation,[59] Thermodynamic Integration calculations,[60] phase-coexistence simulations,[61] and recent attempts using advanced ensemble sampling and order parameters.[62] Yet in spite of these advances, calculating the full P-T phase diagram is still a computationally expensive proposition. Moreover, while evaluation of the relative Gibbs energy of the various phases is essential, calculations of other useful thermodynamic potentials, such as entropy and heat capacity, are either difficult to obtain in the former or require additional, extensive simulations to obtain the latter.

In this study, we develop an approach for rapidly determining phase diagrams, based on explicit calculations of the entropy, enthalpy and Gibbs energy of competing phases in isolation, using the Two-phase thermodynamic (2PT) model. [63-66] The attractiveness of this approach is that it allows for the generation of the P-T phase diagram from short MD simulations, usually ~ 20ps after equilibration. Our previous work has shown that the 2PT method predicts the properties of CO₂ along the saturated vapor-liquid coexistence curve in good agreement with experiments, using the EPM2 model. Here, we expand on that study and show that by considering the

thermodynamic properties of the CO₂ crystal, one can obtain good agreement compared to experiments along the entire P-T phase diagram at little extra computational cost. Moreover, our approach allows for the straightforward elaboration of the separate entropic and enthalpic energies across the phase boundaries, gaining further insights into the nature of phase transitions. Finally, we develop a new Quantum-Mechanics (QM) based, fluctuating charge forcefield, termed CO₂-Fq, which leads to improved performance over the phase diagram and allow us to quantify the role of intermolecular charge renormalization on phase stability.

3.3. Theoretical Approach Background

3.3.1. Two-Phase Thermodynamic (2PT) Method for rapid evaluation of the Entropy and Gibbs Energy

Details of the 2PT method have been published elsewhere,[64, 65, 67] so we summarize the salient points here and introduce an overview in Section 3.3.1.1 and Section 3.3.1.2. In 2PT, we represent the thermodynamics of a condensed phase liquid as a linear combination of two subsystems:

$$Q = fQ^{\text{gas}} + (1-f)Q^{\text{solid}} \quad , \quad (3.1)$$

where Q^{gas} represents the thermodynamics of a hard-sphere gas, in the limit that all the modes are diffusive and Q^{solid} is the thermodynamics of a Debye vibrating crystal, in the limit that all the modes are vibrational. In principle, the thermodynamic properties of these two subsystems can be obtained exactly from statistical mechanics.[68] In practice, we obtain the Q^{gas} at constant density, and temperature from the Carnahan-Starling equation of state,[69, 70] while Q^{solid} is obtained from the frequency dependent reweighting of the Density of States function (DoS, also known as the

spectral density), as a Fourier transform of the velocity autocorrelation function [71] in MD simulations.

This superposition theory is based on early work by Eyring and Ree.[72] Lin and coworkers showed that the partition (or “fluidicity”) factor f in Equation 3.1, which determines the relative weight of each subsystems, can be obtained self-consistently from an MD simulation as a ratio of the computed self-diffusion constant to that of a hard-sphere fluid at the same temperature and density.[64] When applied to molecular systems, recent work has shown that in the limit of independent molecular motions, the total system thermodynamics can be obtained from linear combinations of the thermodynamics resulting from (self-)diffusional, librational (both solid-like translations and rotations) and internal vibrational contributions.[65, 73, 74] A recent extension by Desjarlais showed that the frequency dependent distribution DoS of the gas-subsystem can be better approximated using a Gaussian memory function, which leads to improved results compared to experiments.[66]

The ultimate utility of the 2PT method in the current context is that it has the correct asymptotic behavior (by construction), so it can be applied equally in determining the thermodynamic properties of solids, liquids and gases within the same computational framework. Previous work has shown 2PT to be efficient (only required $\sim 10 - 20$ ps trajectories), with acceptable accuracy compared to more exact, but computationally expensive, Thermodynamic Integration and Free Energy Perturbation schemes.[67] These advantages are leveraged presently to calculate the entire phase diagram of CO_2 , from independent MD simulations of the three competing phases at specific temperatures and pressures.

3.3.1.1. Calculation of the Density of State (DoS) function

The density of state function, $S(\nu)$, is defined as the sum of the contribution from mass weighted atomic densities of all atoms in the system: [64, 65]

$$S(\nu) = \frac{2}{kT} \sum_{j=1}^N \sum_{k=1}^3 m_j S_j^k(\nu) , \quad (3.2)$$

where N is the total number of atoms in the system, m_j is the mass of atom j , $S_j^k(\nu)$ is the spectral density of atom j in k^{th} coordinate (In Cartesian coordinate, $k = x, y, z$). By applying a Fourier transform to Equation 3.2, we obtain the frequency-dependent spectrum:

$$S_j^k(\nu) = \lim_{\tau \rightarrow \infty} \frac{1}{2\tau} \left| \int_{-\tau}^{\tau} v_j^k(t) \exp(-i2\pi\nu t) dt \right|^2 , \quad (3.3)$$

where $v_j^k(t)$ is the velocity of atom j in k direction at time t .

The density of state function, $S(\nu)$, is calculated by combining Equations 3.2 and 3.3:

$$S(\nu) = \frac{1}{kT} \sum_{j=1}^N \sum_{k=1}^3 \lim_{\tau \rightarrow \infty} \frac{m_j}{\tau} \left| \int_{-\tau}^{\tau} v_j^k(t) \exp(-i2\pi\nu t) dt \right|^2 , \quad (3.4)$$

$$\begin{aligned} \int_0^{\infty} S(\nu) d\nu &= \frac{1}{2} \int_{-\infty}^{\infty} S(\nu) d\nu \\ &= \frac{1}{kT} \sum_{j=1}^N \sum_{k=1}^3 m_j \overline{v_j^k(t)^2} \\ &= \frac{1}{kT} \sum_{j=1}^N \sum_{k=1}^3 kT = 3N , \end{aligned} \quad (3.5)$$

where the integration of $S(\nu)$ is equal to the total number degree of freedom of the system in Equation 3.5.

The relationship between the density of state function, $S(\nu)$, the velocity correlation function, $C(t)$, and self-diffusion coefficient, D is given by Equations 3.6 – 3.8:

$$S(\nu) = \frac{2}{kT} \lim_{\tau \rightarrow \infty} \int_{-\tau}^{\tau} C(t) \exp(-i2\pi\nu t) dt , \quad (3.6)$$

$$D = \frac{1}{3} \int_{-\infty}^{\infty} C(t) dt = \frac{1}{6mN} \int_{-\infty}^{\infty} C(t) dt , \quad (3.7)$$

$$S(0) = \frac{2}{kT} \int_{-\infty}^{\infty} C(t) dt = \frac{12mND}{kT}, \quad (3.8)$$

For a polyatomic molecule system, the DoS function is decomposed into translation, rotation, and vibration motions, which are assumed to be independent, so that we can write the total DoS as a sum of the individual DoS functions:

$$S(v) = S_{trans}(v) + S_{rot}(v) + S_{vib}(v), \quad (3.9)$$

We calculate $S_{trans}(v)$ and $S_{rot}(v)$ by integrating over the respective functions:

$$S_{trans}(v) = \frac{1}{kT} \sum_{j=1}^M \sum_{k=1}^3 \lim_{\tau \rightarrow \infty} \frac{m_j}{\tau} \left| \int_{-\tau}^{\tau} v_j^k(t) \exp(-i2\pi vt) dt \right|^2, \quad (3.10-a)$$

$$S_{rot}(v) = \frac{1}{kT} \sum_{j=1}^M \sum_{k=1}^3 \lim_{\tau \rightarrow \infty} \frac{I_j^k}{\tau} \left| \int_{-\tau}^{\tau} \omega_j^k(t) \exp(-i2\pi vt) dt \right|^2, \quad (3.10-b)$$

where the M is total number of molecules in the system, m_j is the mass of molecule j . I_j^k , v_j^k and ω_j^k are the principle moments of inertia, the center of mass velocity and the angular velocity of molecule j in the k^{th} dimension, respectively. [63, 65]

3.3.1.2. Obtaining Thermodynamic Properties from the 2PT Method

The 2PT method approximate the total DoS into a linear combination of the DoSs of a solid and gas subsystem. This builds upon an early idea of Ree and Eyring[72] and early work by Wilson and co-workers[71]. The main idea is that the thermodynamics of each subsystem can be obtained straightforwardly using statistical thermodynamics and standard numerical techniques, with the only variable being the fraction of the liquid state that is “purely diffusive”, i.e. resides in the gas subsystem.

To start, we first consider the solid subsystem, and see that we can obtain the canonical partition function, Q , from the $S(v)$, assuming a Debye vibrating crystal: [64]

$$\ln Q = \int_0^{\infty} dv S(v) \ln q(v), \quad (3.11)$$

where $q = (\exp(-\beta hv/2))/(1 - \exp(-\beta hv/2))$, $\beta = 1/kT$ is the thermodynamic temperature, and h is Plank's constant. The energy, E , entropy, S , Helmholtz free energy, A , constant volume heat capacity, C_v can then be obtained by numerical integration with the appropriate weighting functions: [63, 65]

$$E^S = E_o + T\beta^{-1}(\partial \ln Q / \partial T)_{N,V} = E_o + \beta^{-1} \int_0^\infty dv S(v) W_E(v), \quad (3.12-a)$$

$$S^S = k \ln Q + \beta^{-1}(\partial \ln Q / \partial T)_{N,V} = k \int_0^\infty dv S(v) W_S(v), \quad (3.12-b)$$

$$A^S = E_o - \beta^{-1} \ln Q = E_o + \beta^{-1} \int_0^\infty dv S(v) W_A(v), \quad (3.12-c)$$

$$C_v^S = (\partial E / \partial T), \quad (3.12-d)$$

$$W_E^S(v) = \beta hv/2 + \beta hv / (\exp(\beta hv) - 1), \quad (3.13-a)$$

$$W_S^S(v) = \beta hv / (\exp(\beta hv) - 1) - \ln[1 - \exp(-\beta hv)], \quad (3.13-b)$$

$$W_A^S(v) = \ln[(1 - \exp(\beta hv)) / (\exp(-\beta hv/2))], \quad (3.13-c)$$

$$W_{C_v}^S(v) = [(\beta hv)^2 \exp(\beta hv)] / [\exp(-\beta hv) - 1]^2, \quad (3.13-d)$$

For the gas subsystem, the DoS decays monotonically with frequency. Lin and co-workers found that for polyatomic molecules systems, the properties and weighting functions of gas portion can be decomposed into translation (trans), rotation (rot) and vibration (vib) motion, shown in Equation 3.14.

$$S^g(v) = S_{trans}^g(v) + S_{rot}^g(v) + S_{vib}^g(v), \quad (3.14)$$

where the superscript g means gas-like portion.

Besides, in 2PT model, it is assumed that all diffusive motion is included in gas-like portion, thus $S(0) = S^g(0)$, and all vibration motion is included in solid-like mode, indicating $S_{vib}(v) = S_{vib}^S(v)$. Based on these assumptions, the entropy of gas-like portion is further determined by $S(0)$ and its fluidicity factor, f .

$$S_m^g(v) = S_m(0)/\{1 + [(\pi v S_m(v))/(6f_m M)]^2\}, \quad (3.15)$$

where the m means translation, rotation or vibration mode, $S_m(0)$ is the zero point entropy on m mode and f_m is the fluidicity factor which is determined by Equations 3.16 and 3.17.

$$2\Delta_m^{-9/2} f_m^{15/2} - 6\Delta_m^{-3} f_m^5 - \Delta_m^{-3/2} f_m^{7/2} + 6\Delta_m^{-3/2} f_m^{5/2} + 2f_m - 2 = 0, \quad (3.16)$$

$$\Delta_m = [(2S_m(0))/(9M)][\pi kT/m]^{1/2}[N/V]^{1/3}[6/\pi]^{2/3}, \quad (3.17)$$

Thus, the total energy, entropy, free energy, and heat capacity relation can be derived as Equation 3.18.

$$E_m = \beta^{-1}[\int_0^\infty dv S_m^S(v) W_{m,E}^S(v) + \int_0^\infty dv S_m^g(v) W_{m,E}^g(v)], \quad (3.18-a)$$

$$S_m = k[\int_0^\infty dv S_m^S(v) W_{m,S}^S(v) + \int_0^\infty dv S_m^g(v) W_{m,S}^g(v)], \quad (3.18-b)$$

$$A_m = \beta^{-1}[\int_0^\infty dv S_m^S(v) W_{m,A}^S(v) + \int_0^\infty dv S_m^g(v) W_{m,A}^g(v)], \quad (3.18-c)$$

$$C_{v_m} = k[\int_0^\infty dv S_m^S(v) W_{m,C_v}^S(v) + \int_0^\infty dv S_m^g(v) W_{m,C_v}^g(v)], \quad (3.18-d)$$

To obtain the weighting function of gas-like portion, the hard sphere particle assumption is applied, and the values are calculated by Equation 3.19.

$$W_{rot,E}^g(v) = W_{trans,E}^g(v) = W_{trans,C_v}^g(v) = W_{rot,C_v}^g(v) = 0.5, \quad (3.19-a)$$

$$W_{trans,S}^g(v) = \frac{1}{3}\left(\frac{S^{HS}}{k}\right), \quad (3.19-b)$$

$$W_{rot,S}^g(v) = \frac{1}{3}\left(\frac{S^R}{k}\right), \quad (3.19-c)$$

$$W_{rot,A}^g(v) = W_{rot,E}(v) - W_{rot,S}(v), \quad (3.19-d)$$

where S^{HS} is the hard sphere entropy and S^R is the rotation entropy at ideal gas state, which are defined in Equation 3.20.

$$\frac{S^{HS}}{k} = \frac{5}{2} + \ln\left[\left(\frac{2\pi mkT}{h^2}\right)^{\frac{3}{2}}\left(\frac{V}{f_{trans}N}\right)z(y)\right] + y(3y - 4)/(1 - y)^2, \quad (3.20-a)$$

$$\frac{S^R}{k} = 1 + \ln\left(\frac{T}{\sigma\theta_r}\right), \quad (3.20-b)$$

with $y = f_{trans}^{5/2} / \Delta_{rot}^{3/2}$, $z(y)$ = the compressibility factor, $\theta_r = h^2 / (8\pi I_r k)$ and σ = the symmetry number. The reference entropy, E_o , is obtained by Equation 3.21. [63]

$$E_o = E^{MD} - \beta^{-1} 3N (1 - 0.5f_{trans} - 0.5f_{rot}) , \quad (3.21)$$

Based on the previous equations, properties of a system are determined by summing up the gas and solid contributions.

3.3.2. Partial atomic charges from the Charge Equilibration (QEq) Method

Traditional empirical forcefield are usually based on partial atomic charges that are fixed, with the total electrostatic energy obtained by Coulomb's law. While various approaches have been developed to obtain these atomic charges, in modern forcefields they are usually based on 1) population analysis of the QM wavefunction or electron density for isolated, gas-phase molecules or fragments; or 2) empirically fitted to reproduce the high order electrostatic moments (i.e., dipole, quadrupole, octupole, etc.) of the molecule. The choice of fixed atomic charges introduces some conceptual difficulties for performing simulations under conditions not explicitly considered during the charge parameterization, although modern forcefield can mitigate this somewhat by optimizing the two-body van der Waals potential. Indeed, applying this strategy, the properties of condensed phase systems using fixed charges can be reasonable under normal temperature and pressure (NTP) conditions. Specifically, in the case of CO₂, this strategy has led to the development of the EPM2 model, optimized to reproduce the critical properties.

Despite its attractiveness, the ability of fixed charge potentials to reliably predict the equilibrium thermodynamics far from NTP is not guaranteed and is in fact frequently compromised. This is partly due to the fact that highly compressed systems can minimize their

total energy by redistributing the electron clouds around the atoms (i.e., the Pauli force), an effect that may not be correctly represented by analytic functions with power series decays, such as frequently used Lennard Jones 12-6 potentials. One approach for approximating QM charge reorganization physics is the application of polarizable forcefields. These can be generally classified as either inducible point dipole (PD), [75] classical Drude oscillators [76] or fluctuating charge (FC) [77] approaches. PD models, such as the AMOEBA [78] forcefield for example, have been successful in simulating biological systems [79], and, more recently, ionic liquids [80].

In this work, we consider FC models, due to their inherent simplicity and intuitiveness. FC models aim to address the fundamental problem of assigning partial charges to atoms within a molecule, while simultaneously minimizing the electrostatic energy, under constraints of fixed overall system charge. The most popular schemes are based on the electronegativity equalization principle of Sanderson [81], which incorporates Mulliken electronegativities [82] χ and idempotential J . [13]. Here, the total electrostatic energy $E(q)$ of an atom is represented as a Taylor series expansion of the charge q :

$$\begin{aligned}
 E(q) &= E_0 + q \chi + \frac{1}{2} q^2 J + \dots, \\
 \chi_i &= \left(\frac{\partial E}{\partial q} \right) = \frac{1}{2} (IP_i + EA_i) = -\mu_i, \\
 J_i &= \left(\frac{\partial^2 E}{\partial q^2} \right) = (IP_i - EA_i), \tag{3.22}
 \end{aligned}$$

where IP is the ionization potential, EA is the electron affinity and μ is the chemical potential. The subscript i represents as the i th atom and the difference between IP and EA represents as the idempotential, J . Equation 3.22, in effect, represents the many-body, quantum mechanical electron density in a highly simplified basis. The coulomb interactions are either calculated by means of an

analytic screened coulomb function in the popular EEM scheme [83], as the overlap of Slater-type ns orbitals in QEq [13, 84, 85], or more recently, as overlaps of 1s Gaussian type orbitals with atomic polarization, as follows: [86, 87]

$$J_{i,j}(\vec{r}) = \frac{1}{r} \operatorname{erf}\left(\sqrt{\frac{\alpha_i \alpha_j}{\alpha_i + \alpha_j}} r\right), \quad (3.23)$$

where $J_{i,j}(\vec{r})q_iq_j$ is the electrostatic energy, i and j represent as the atomic indices, and α is the width of the Gaussian distribution: $\alpha = 0.2314/R^2$ (R is the atomic radius). We use Equation 3.23 to calculate the electrostatic energy in the CO₂-Fq model.

We note that the many-body nature of FC models arises from the fact that the computed partial atomic charges are obtained self-consistently and include contributions from the self-energy as well as the interactions with other neighboring atoms. These charges are usually recalculated every step, and so varies smoothly as the local environment around the atom changes during an MD simulation. In principle, there are only two universal parameters for each element (χ and J) that can be used to reproduce the electrostatic energy of arbitrary systems. In practice, these parameters are somewhat system specific, and we present a new parameter set for CO₂, which we combine with various other potential energy surfaces derived from high level QM calculations, to produce the CO₂-Fq forcefield.

3.4. Computational Details

3.4.1. Description of Initial Systems

For simulations employing the FEPM2 forcefield, the initial structure of a CO₂ crystal was obtained from the ICSD [88, 89] (database code ICSD 16428), with the cubic space group 205 (Pa-3) and lattice constant $a=5.624 \text{ \AA}$. We generated a 4x4x4 supercell (256 molecules) with the initial simulation cell of 22.496 \AA in x, y and z directions. To represent the liquid phase, we generated an amorphous CO₂ structure (256 molecules), initially at a density of 1.185 g/cm³ and an initial simulation cell of 23.86 x 23.86 x 27.84 \AA^3 . For simulations of the saturated vapor/liquid at the vapor-liquid coexistence (VLE) conditions, an amorphous structure with 252 molecules was used, with initial densities obtained from the NIST database.[90] Gas systems, which are not at saturated vapor condition, contained more molecules (512 amorphous molecules) to provide enough molecule-collisions to converge the thermodynamics. When using the CO₂-Fq forcefield, a smaller crystal cell, with 108 CO₂ molecules in 3x3x3 structure (16.872 \AA in x, y and z directions), was used. In the corresponding liquid simulations, we used a cell with 108 amorphous molecules at all conditions except for the VLE condition, where we used a cell with 125 molecules.

3.4.2. The Flexible-EPM2 Carbon Dioxide Forcefield

The FEPM2 parameters are shown in **Table 3.1**. The valence interactions (i.e. the C-O bond stretching and angle bending motions) are modeled as harmonic springs, which is normally sufficient to provide a similar potential energies surface compared to QM for small displacements [57]:

$$\begin{aligned}
E_{valence} &= E_{bonds} + E_{angles} \\
&= K_b (x - x_0)^2 + K_\Theta (\Theta - \Theta_0)^2,
\end{aligned}
\tag{3.24}$$

where x_0 is the equilibrium C-O bond length and Θ_0 is the equilibrium O-C-O angle. The value of the K_b and K_Θ force constants are taken from our previous work [63] and Ref [57], respectively. The van der Waals interactions are described with a Lennard-Jones 12-6 potential (LJ),

$$E_{vdw}^{LJ12-6} = 4\epsilon_{ij} \left[\left(\frac{\sigma_{ij}}{r_{ij}} \right)^{12} - \left(\frac{\sigma_{ij}}{r_{ij}} \right)^6 \right],
\tag{3.25}$$

with interaction energies ϵ and equilibrium distances σ taken from our previous work.[63]

3.4.3. FEPM2 Molecular Dynamics Simulations

All MD simulations were performed using the LAMMPS[1] engine. For the FEPM2 model, we initiated our simulations with 500 steps of conjugated gradient (CG) minimization. Afterwards, 10ps Langevin dynamics was applied, to heat up a system to a defined temperature. This was followed by iso-thermo / iso-baric dynamics (NPT) at the relevant pressure. To ensure equilibrium conditions, we then conducted twice 5ns of Langevin dynamics, followed by another

Table 3.1 FEPM2 force field parameters for CO₂

Atom	Charge (e)	Van der Waals (LJ)		Bond (Harmonic)		Angle (Harmonic)			
		ϵ (K)	σ (Å)	x_0 (Å)	K_b (kcal/mol/Å ²)	Θ_0 (degree)	K_Θ (kcal/mol/radian ²)		
C	0.6512	C 28.13	2.757	C-O	1.149	1284	O-C-O	180	147.8
O	-0.3256	O 80.51	3.033						

3ns of canonical (NVT) dynamics using a Nose-Hoover thermostat. For simulations involving the gas-phase systems, we did not perform NPT dynamics for maintaining the density property. The real space cutoffs for the Lennard-Jones and coulomb potentials were 9Å and 10Å, respectively. The long-range electrostatic were calculated with the particle-particle particle-mesh approach, with force tolerance of 10^{-4} . We verified that this force tolerance was adequate by performing simulations with force tolerances of 10^{-6} and 10^{-8} , which produced identical results.

3.4.4. FEPM2 Thermodynamics of the Solid and Liquid Phases

After equilibration, we ran an additional 200ps NVT simulation, with the trajectory (atomic positions and velocities) saved every 4fs. The thermodynamics were then obtained from an in-house code that implements the 2PT method.[91] Uncertainties in our measurements were obtained from statistical average from 10 independent simulation of 200ps each.

3.4.5. FEPM2 Thermodynamics of the Gas Phase

Two different procedures were employed to obtain the thermodynamics of the gas phases. First, we considered a low-density gas with a large number (512) of molecules and calculated the thermodynamics using the 2PT method over a 2ns sampling window. We verified that this approach has enough molecular collisions to converge the VAC and produce converged thermodynamics. Second, we considered a high-density gas near the vapor-liquid coexistence condition, and approximated the Gibbs energies based on simulation results of the saturated vapor thermodynamics and the ideal gas equation:

$$S = S_{sat} - R \ln \left(\frac{P}{P_{sat}} \right)$$

$$E = E_{sat} \quad , \quad (3.26)$$

where S , P , E , and R are denoted as entropy, pressure, internal energy, and gas constant, respectively, S_{sat} and E_{sat} are the entropy and internal energy respectively of a saturated vapor system at a certain temperature condition. In this work, we adopted the second procedure (high-density gas computations) as the gas reference to determine the vapor–liquid coexistence phase transition curve since we found it to be more computationally robust.

3.4.6. Construction of the CO₂-Fq Forcefield

We obtained the intra- / inter- molecular parameters of CO₂ from quantum mechanics calculations via the Q-Chem 5.2 package [2] at the aug-cc-pVTZ/MP2 level of theory. The C-O bond stretching was obtained by fitting the QM energies (**Table 3.2**) to a Morse potential,

$$E_{bond} = D_e [1 - \exp(-\alpha(r - r_0))]^2, \quad (3.27)$$

with bond energy D_e , equilibrium distance r_0 and curvature α .

The O-C-O angle bending was obtained by fitting the QM energies to a harmonic potential,

$$E_{angle} = K_{\Theta} (\Theta - \Theta_0)^2, \quad (3.28)$$

with force constant K_{Θ} and equilibrium angle Θ_0 .

Table 3.2 The intra-molecular energies of CO₂

Intra-molecular energies			
C-O Bond stretching			
C-O Bond	QM	CO ₂ -Fq	FEPM2
Å	kcal/mol	kcal/mol	kcal/mol
1.109	4.8796	5.2077	2.0544
1.119	3.3385	3.6207	1.1556
1.129	2.1141	2.3451	0.5136
1.134	1.6145	1.8185	0.2889
1.139	1.1866	1.3632	0.1284
1.149	0.5370	0.6581	0
1.154	0.3108	0.4042	0.0321
1.159	0.1476	0.2136	0.1284
1.164	0.0453	0.0843	0.2889
1.169	0.0018	0.0145	0.5136
1.17	0	0.0075	0.5662
1.171	0.0005	0.0028	0.6215
1.172	0.0032	0.0004	0.6792
1.173	0.0081	0.0002	0.7396
1.174	0.0153	0.0023	0.8025
1.179	0.0839	0.0460	1.1556
1.184	0.2057	0.1439	1.5729
1.189	0.3791	0.2943	2.0544

O-C-O Angle bending			
O-C-O Angle	QM	CO ₂ -Fq	FEPM2
Radian	kcal/mol	kcal/mol	kcal/mol
3.1416	0	0	0
3.1590	0.0168	0.0169	0.0450
3.1765	0.0670	0.0678	0.1801
3.1939	0.1509	0.1525	0.4052
3.2114	0.2683	0.2711	0.7204
3.2289	0.4195	0.4235	1.1256
3.2638	0.8233	0.8301	2.2061
3.2812	1.0764	1.0842	2.8814
3.3161	1.6854	1.6941	4.5022
3.4034	3.8201	3.8118	10.1300

Table 3.2 The intra-molecular energies of CO₂ (Continued)

1.194	0.6023	0.4955	2.6001
1.204	1.1917	1.0441	3.8841
1.209	1.5547	1.3884	4.6224
1.219	2.4099	2.2097	6.2916
1.229	3.4281	3.1981	8.2176
1.239	4.5984	4.3430	10.4004
1.249	5.9111	5.6338	12.84

QM, CO₂-Fq, and FEPM2 denote as quantum-mechanics, CO₂-Fq, and FEPM2 energies, respectively. All QM energies were calculated via Q-Chem 5.2 package [2] at aug-cc-pVTZ/MP2 level.

The van der Waals interactions were obtained from fitting the QM binding energies of three different dimer configurations to the universal nonbonded (UNB) function [92, 93] (**Table 3.3**),

$$E_{vdw} = -D_e \exp\left[-\beta\left(\frac{r-R_e}{L}\right)\right] \sum_{n=0}^5 \alpha_n \left(\frac{r-R_e}{L}\right)^n, \quad (3.29)$$

where the R_e , D_e , and L are the equilibrium distances, the binding energies, and the scaling lengths, respectively. In keeping with a previous study,[92] the parameters series (β , α_0 , α_1 , α_2 , α_3 , α_4 , α_5) were defined as (1.00348500, 1.0, 1.02009000, 0.01678480, 0.00327294, 0.00365706, 0.00106613). We employed the UNB functional form here as it gave better fits to the QM binding energies compared to the more popular Lennard Jones, Exponential-6 or Morse potentials. The QEq parameters for carbon and oxygen in Equation 3.22 were fitted to reproduce the gas phase quadrupole moment of CO₂ from QM. During the MD simulation, the atomic charges were updated every timestep using an iterative (maximum of 10 iterations) conjugate gradient scheme [94], with a charge tolerance of 10^{-6} . In practice, the charges were found to converge after two iterations.

Table 3.3 The inter-molecular binding energies of the CO₂ dimer

Inter-molecular energies											
T-shape configuration				Line-up configuration				Parallel configuration			
R	QM	CO ₂ -Fq	FEP2	R	QM	CO ₂ -Fq	FEP2	R	QM	CO ₂ -Fq	FEP2
Å	kcal/mol	kcal/mol	kcal/mol	Å	kcal/mol	kcal/mol	kcal/mol	Å	kcal/mol	kcal/mol	kcal/mol
3.6	1.7474	1.561333	2.94449	4.2	32.601	35.5614	210.558	2	84.7424	74.4625	203.333
3.8	-0.268	-0.31182	-0.0921	4.5	9.125	9.3574	32.882	2.5	12.8211	12.2982	12.4787
4	-0.9592	-1.00926	-0.9625	5	0.6893	0.6459	2.1365	2.7	5.69	5.7454	4.3881
4.1	-1.0619	-1.12759	-1.07903	5.2	0.1145	0.1230	0.7699	3	1.5154	1.6789	0.8685
4.2	-1.0787	-1.15913	-1.0976	5.3	-0.0089	0.0259	0.4693	3.2	0.5576	0.6787	0.2445
4.3	-1.0442	-1.13579	-1.06199	5.4	-0.0741	-0.0166	0.2909	3.5	0.0802	0.1503	-0.0142
4.4	-0.9812	-1.07963	-0.9983	5.5	-0.1034	-0.0281	0.1852	3.7	0.0024	0.0608	-0.0436
4.6	-0.8229	-0.92377	-0.84208	5.6	-0.1112	-0.0238	0.1231	3.8	-0.0097	0.0479	-0.0444
4.7	-0.7426	-0.84039	-0.76368	5.7	-0.1069	-0.0127	0.0870	3.9	-0.0131	0.0461	-0.0412
4.8	-0.6664	-0.75944	-0.68953	5.8	-0.0962	-0.0002	0.0665	4	-0.0117	0.0506	-0.0359
4.9	-0.5961	-0.68319	-0.62097	6	-0.0689	0.0193	0.0493	4.1	-0.0079	0.0585	-0.0297
5	-0.5322	-0.61281	-0.55847	6.5	-0.0157	0.0214	0.0444	4.2	-0.003	0.0679	-0.0236
								4.3	0.002	0.0774	-0.0177
								4.5	0.0107	0.0943	-0.0077
								5	0.0216	0.1166	0.0070

R is the carbon-carbon distance. QM, CO₂-Fq, and FEP2 denote as quantum-mechanics, CO₂-Fq, and FEP2 energies, respectively. All QM energies were calculated via Q-Chem 5.2 package [2] at aug-cc-pVTZ/MP2 level.

The full set of parameters that defined the CO₂-Fq model is given in **Table 3.4**. In our convention, the R parameter denotes the atomic radius.

Table 3.4 CO₂-Fq forcefield parameters.

	C - C	O - O	C - O
Van der Waals (UNB)			
R_e (Å)	5.42252	3.00361	3.64660
D_e (kcal/mol)	0.04138	0.43302	0.11315
L (Å)	0.69526	0.33056	0.47565
	C	O	
Electrostatic (QEq)			
χ (eV)	5.34300	9.19962	
J (eV)	10.12600	16.07839	
R (Å)	0.75900	0.40344	
Bond (Morse)			
r_0 (Å)	1.17257		
α (1/Å)	2.07474		
D_e (kcal/mol)	262.239		
Angle (Harmonic)			
θ_0 (degree)	180		
K_θ (kcal/mol/radian ²)	55.6154		

3.4.7. CO₂-Fq MD Solid/Liquid Simulations and Thermodynamics

In simulating the CO₂-Fq solid and liquid phase systems, we followed a similar procedure to Section 3.4.3., except that the system electrostatics were obtained from the overlap of Gaussian 1s charge distribution orbitals in Equation 3.23. Importantly, we calculate the charges on each atom by considering every neighboring atom within the cutoff, and include the energies and forces of the 1 – 2 (bond) and 1 – 3 (angle) interactions. We found that application of the Generalized Langevin equation (GLE)[95, 96] to thermostat the system lead to a better distribution of energies at equilibrium. After an initial 500 steps of CG minimization, we performed 10ps of dynamics using the GLE thermostat followed by simulations in the NPT ensemble in order to stabilize the system at a specific temperature and pressure. Afterwards, we performed 3ns NVT dynamics with

the GLE thermostat and another 0.5ns dynamics with the Nose-Hoover thermostat for further equilibration. The real space cutoffs for the UNB and QEq potentials were 10Å and 12.5Å, respectively, and we applied a Taper function to the QEq energies and forces to ensure zero energies and forces at the cutoff. The GLE matrix was tuned to enforce “Smart sampling”, [97] with $N_s=6$ additional degrees of freedoms. Similar to Section 3.4.4, atomic trajectory information of CO₂-Fq solid and liquid systems were collected for 200ps NVT dynamics. The 200ps trajectory information was further applied in 2PT thermodynamics analysis.

3.4.8. CO₂-Fq Thermodynamics of the Gas Phase

The QEq approach equalizes the charges in the thermodynamic limit, leading to spurious long-range charge transfer between molecules. [85, 98] This complicates simulations of gas phase systems. Thus, we obtained the CO₂-Fq gas-phase reference energies at specific points on the P-T diagram by applying the ideal gas law, Equation 3.30, and the minimized energy of the isolated molecule at 0K:

$$S = S^0 - R \ln(P/P_0)$$

$$E = E_{min} + E_{kinetic} + C_p(T - T_0) , \quad (3.30)$$

where the S^0 is the ideal gas entropy at 1atm, E_{min} is the minimum energy of the system at 0 K, $E_{kinetic}$ is the kinetic energy (temperature correction), and C_p is the constant pressure heat capacity correction.

3.4.9. Determination of the Phase Boundaries

We obtained the phase boundaries by explicitly considering the per-molecule Gibbs energy (i.e. the chemical potential μ for a single component system: $\mu(T,P) = g = G/N$) of the respective phases at specific points in the P-T diagram. The most stable phase was determined to be the one with the lowest chemical potential. We employed a multi-resolution approach to efficiently obtain the phase diagram: initial simulations were performed on a coarse sampling of the P-T space. At specific pressures, once a phase transition was detected, we first approximated the location of the phase transition temperature(s) by linear interpolation between adjacent points, followed by further simulations around this temperature in smaller temperature increments. Critical points were treated as special cases, as detailed below.

3.4.10. Determining the Critical Point from the Vapor-Liquid Coexistence curve

A variety of approaches can be used to determine the critical point, such as the discontinuity of constant pressure heat capacity, C_p , [99] or the discontinuity in relaxation times [100]. In this work, we determine the critical point via the VLE curve, [35] exploiting the fact that as the density increases, the temperature at VLE conditions will increase initially and further decrease, with the turnover point being the critical temperature.

3.5. Results and Discussion

3.5.1. Molecular charge distribution in the condensed phase using the CO₂-Fq model

As currently implemented, the QEq approach equalizes the chemical potential of the entire system, applying the charge neutrality constraint. This could lead to non-neutral molecules at any given timestep, and spurious physics. We found that in practice, our current approach (which we employ for computational convenience) led to nearly neutral CO₂ molecules in the condensed phase. We reason that this is due to the relatively high electron affinity of the oxygen atoms, which presents a rather deep, attractive on-site potential and effects a high degrees of electron localization. As a figure of merit, we calculated the distribution of the molecular charges for CO₂-Fq CO₂ at 240K and 100atm in the liquid and solid phases in **Figure 3.1**. This shows a sharp distribution, centered around zero with a variance (1 σ deviation) of $\sim 0.03 e$.

We further tested the validity of our approach by computing the dielectric constant for liquid CO₂-Fq at 240K and 100atm, as determined from the fluctuations in the dipole moment and linear response theory [101]

$$\epsilon = 1 + \frac{4\pi (\langle M^2 \rangle - \langle M \rangle^2)}{3\epsilon_0 V k_B T} , \quad (3.31)$$

where the ϵ , M , ϵ_0 , V , k_B , and T represent as dielectric constant, dipole moment, dielectric constant in vacuum, volume, Boltzmann constant, and temperature, respectively. As shown in **Figure 3.2a**, the calculated dielectric constant values from a 0.5 ns trajectory using the CO₂-Fq model is ~ 1.38 , in excellent agreement with the experimental value of ~ 1.5 [102]. The corresponding dielectric constant of the FEPM2 model was ~ 4.64 (**Figure 3.2b**).

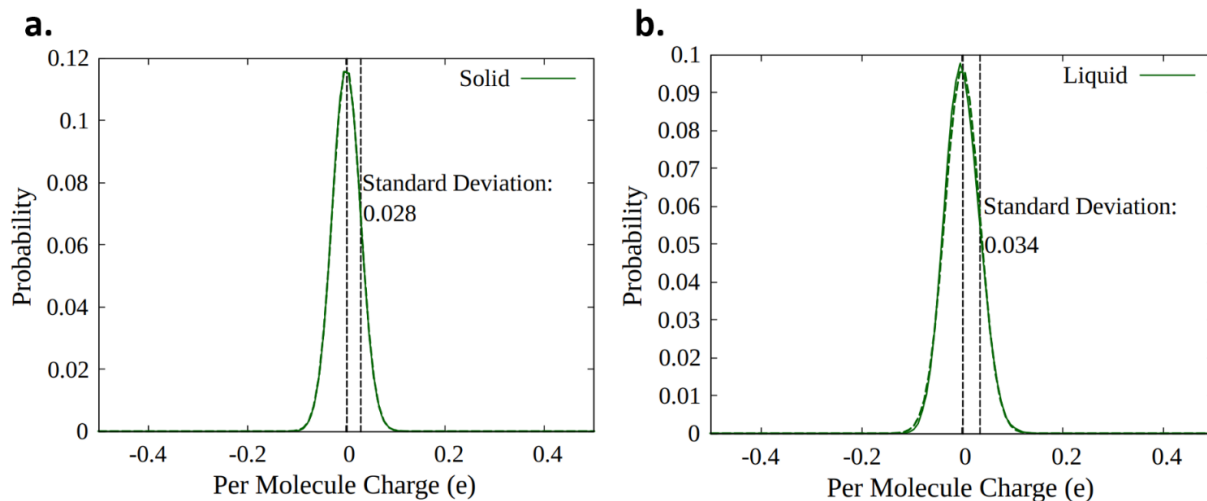


Figure 3.1 The distribution of molecular charges using the CO₂-Fq forcefield for (a) a solid and (b) a liquid at 100atm, 240K. The simulation data (solid lines) are fitted to Gaussian functions (dashed green lines). The dashed black lines indicate the standard deviations (solid: $1\sigma = 0.028$; liquid: $1\sigma = 0.034$).

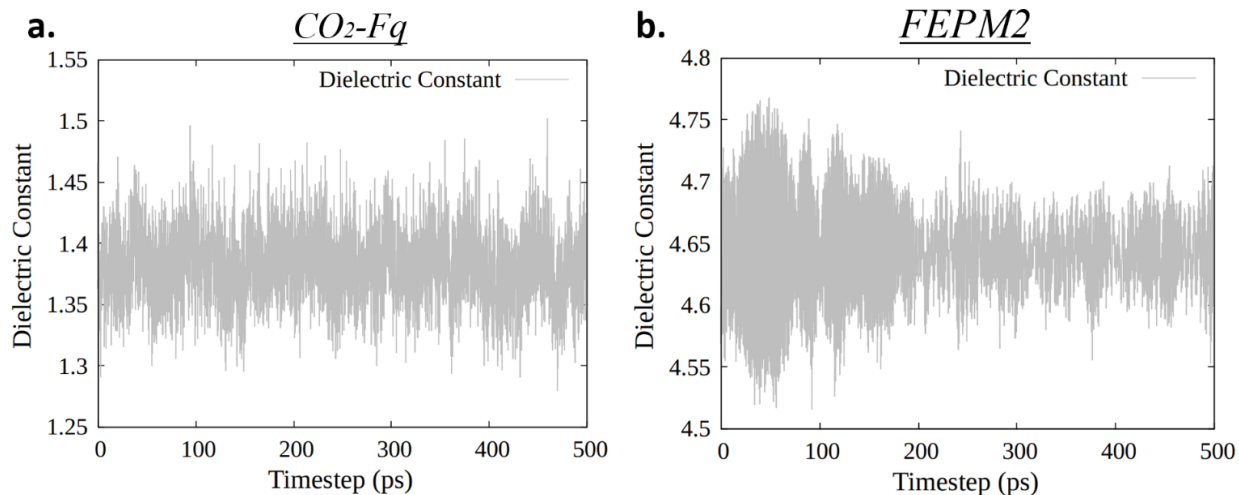


Figure 3.2 The dielectric constant values of 0.5 ns simulation of liquid CO₂ (240K and 100atm) using (a) the CO₂-Fq forcefield and (b) the FEPM2 forcefield. The experimental dielectric constant at these conditions is ~ 1.5 .

3.5.2. Spectral Density function of CO₂

We first tested the convergence of the 2PT method for describing the thermodynamics of CO₂, by considering the VAC function. Normally, for a solid, liquid, or saturated-vapor system, the VAC function converges to zero on the timescale of a few picosecond. A low-density gas, on the other hand, requires longer convergence times, due to the low collision probability between molecules. **Figure 3.3** presents the VAC function of CO₂ described by the FEPM2 and CO₂-Fq models, where we find convergence times of ~ 20ps for the solid and liquid systems and ~ 500ps for the gas. This result validates our computational approach, where the sampling windows (200ps and 2ns respectively) are several factors greater than these typical correlation times.

The associated DoS of liquid CO₂ are shown in **Figure 3.4**. Here we separately consider the independent motions that contribute to the DoS: translations, rotations and internal vibrations. We apply the 2PT method to the translations and rotations, and separately show the distribution of modes from diffusive (gas-like) and from librational (solid-like) motions. The purely vibrational degrees of freedom at equilibrium are analogous to the non-equilibrium response of the system when excited by Raman and infrared radiation,[103] providing a 1:1 mapping between molecular thermodynamics and spectroscopy. We find that the vibrational spectrum of the solid and liquid phases CO₂ described with the FEPM2 forcefield are in reasonable agreement with the experimental asymmetric and symmetric bond stretching frequencies. However, the FEPM2 angle bending force constant (taken from the work of Trinh et al. [57]), leads to a 60% increase in the O-C-O bond bending frequency, compared to experiments (1102 cm⁻¹ vs 667.38 cm⁻¹, respectively). Additionally, the FEPM2 model is unable to reproduce the Fermi resonance peak, which results from a coupling between the O-C-O angle bending and the C-O bond stretching (i.e. cross terms), observed experimentally. Conversely, we find that the full QM-derived CO₂-Fq

model produces improved vibrational properties compared to experiments (**Table 3.5**) and remarkably, captures the Fermi resonance, with two peaks at 1278 cm^{-1} and 1378 cm^{-1} , even though the cross term was not included in the parameterization.

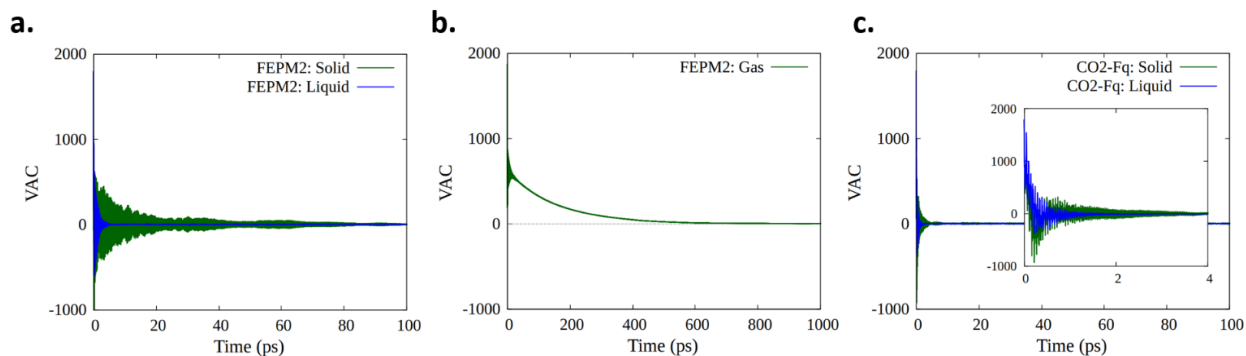


Figure 3.3 The CO₂ total VAC function of (a) FEPM2 solid/liquid density systems at 240K, 100atm, (b) FEPM2 gas density system at 1atm, 250K and (c) CO₂-Fq solid/liquid density systems at 240K, 100atm. The zoomed inset of (c) demonstrates the VAC function details within 0 – 4 ps.

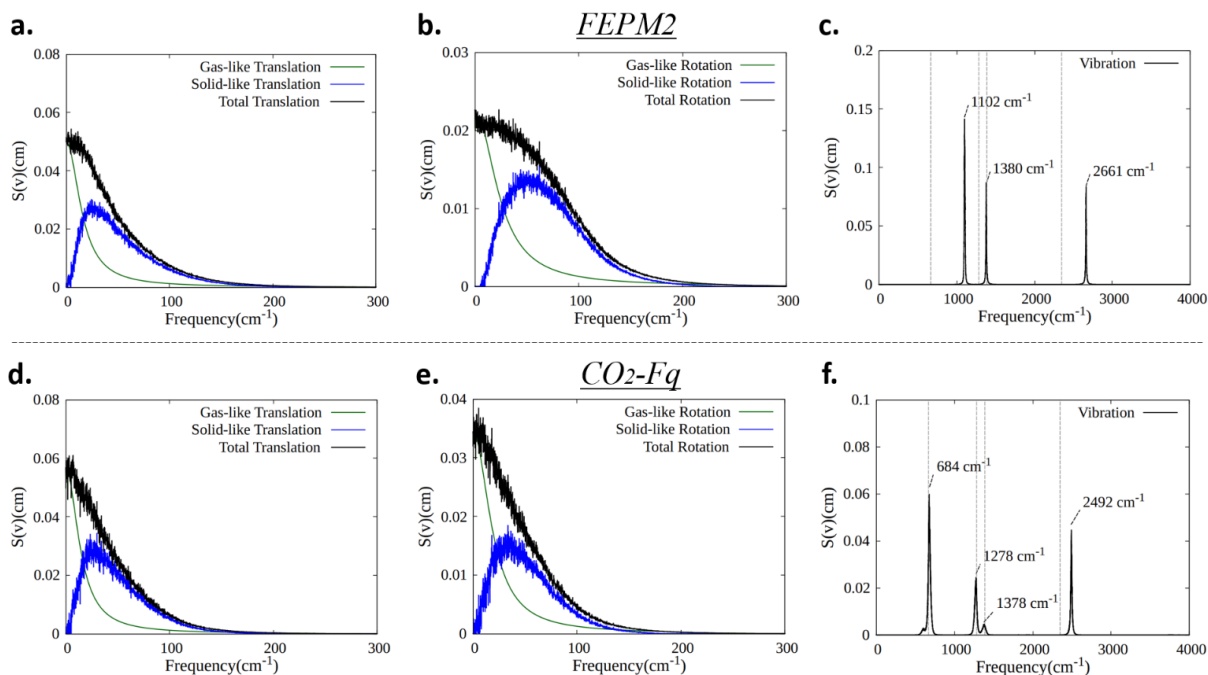


Figure 3.4 The per-molecule CO₂ DoS functions of (a) translational, (b) rotational, and (c) vibrational motion for FEPM2 model and the CO₂-Fq model (d, e and f respectively), for the liquid at 240K and 100atm. The decomposition of the translational and rotational spectrum into contributions arising from diffusive (gas-like, green) and librational (solid-like, blue) contributions as determined by the 2PT method portions are shown. The experimental vibrational frequencies are shown as dashed gray lines.

Table 3.5 CO₂ vibration frequencies from experiment and FEPM2/CO₂-Fq MD simulations

	Experiments [63] [cm ⁻¹]	FEPM2 (240K,100atm with liquid density) [cm ⁻¹]	CO ₂ -Fq (240K,100atm with liquid density) [cm ⁻¹]
Symmetric stretching	1285.40 (Raman) 1388.15 (Raman)	1380	1278 1378
Asymmetric stretching	2349.16 (IR)	2661	2492
Angle bending	667.38 (IR)	1102	684

3.5.3. The Thermodynamic Properties of Carbon Dioxide

3.5.3.1. Thermodynamics of Crystalline CO₂

We now turn our attention to the thermodynamics of crystalline CO₂ at low temperatures, which is a more stringent test of the (gas-phase) derived interaction potentials. Specifically, we consider the calculated entropy potential, which we compare to a purely theoretical model computed from empirical parameters (**Table 3.6**) and the following equation:

$$\begin{aligned}
\Delta S &= \int dS \\
&= \int dH/T - \int VdP/T + \Delta H_{\text{phase-change}}/T_{\text{phase-change}} \\
&= \int C_P^G/T dT + \int C_P^L/T dT + \int C_P^S/T dT - nR \int dP/P + \Delta H_{\text{vap}}/T_{\text{vap}} + \Delta H_{\text{fus}}/T_{\text{fus}}, \quad (3.32) \\
&\text{or} \\
&= \int C_P^G/T dT + \int C_P^S/T dT - nR \int dP/P + \Delta h_{\text{sub}}/T_{\text{sub}}
\end{aligned}$$

where C_p is the constant pressure heat capacity, the superscript G , L , and S represent gas, liquid and solid, respectively. ΔH is the phase change enthalpy, the subscript vap, fus, and sub represent

Table 3.6 Equations and data used for thermodynamic properties calculation. Empirical thermodynamic data from References [90, 104]

	Equations / Data
Constant pressure heat capacity, C_p [T in K; C_p in J/mol/K]	$C_p^G = 27.437 + 0.042315 T - 1.955 \cdot 10^{-5} T^2 + 4 \cdot 10^{-9} T^3 - 2.99 \cdot 10^{-13} T^4$ $C_p^L = -338.956 + 5.28T - 0.0233T^2 + 3.6 \cdot 10^{-5} T^3$ $C_p^S = -1.63 + 0.542T - 0.00127T^2$
ΔH_{sub} at 195K, 1atm [kJ/mol]	25.2
S^0 at 298K, 1bar [J/mol/K]	213.785

vaporization, fusion, and sublimation, respectively. The number of moles of CO₂ in a system is denoted by n , R is the gas constant, and P is the pressure. We note that the entropy computed from 2PT method (referred henceforth as the 2PT entropy) applies the quantum harmonic oscillator weighting function to each of the (classical) modes, a hybrid approach that produces “quantum” entropies in very good agreement with experiment for a variety of liquid systems at ambient conditions.[63, 66, 67, 73, 74, 105-109] Of course, the 2PT method is equally applicable to purely solid and gas system, which are the limiting cases of the theory. We demonstrate this by noting that the fluidicity factors for the crystalline solids are small, as expected, but slowly increasing with increasing temperature.

We find that the calculated entropies are in very good agreement with the theoretical model at low temperatures (**Table 3.7**). Overall, the entropy of the CO₂-Fq model is larger than FEPM2, reflecting the additional degree of freedom (fluctuating partial atomic charge) in the former. This ultimately leads to an overestimation of the entropy, compared to the thermodynamic model, by ~ 5 – 10%. Encouragingly, the temperature of the translational, rotational, and internal vibrational modes was consistent with the system temperatures, verifying equipartition and thermal equilibration and further validating our computational approach. Indeed, we found that application

of a stochastic thermostat (Langevin or GLE) was necessary for proper mode thermal equilibration for these nanosized system on the nanosecond timescale. The application of deterministic thermostats (Nose-Hoover) required an order of magnitude longer simulation to achieve proper mode equipartition, even though the overall temperature of the system and the per-molecule distribution of total kinetic energy converged in much shorter timescales.

As a further check of equilibration, we note that the distribution of C-O bond lengths is normal and can be fit to a Gaussian function with near zero skewness (2nd moment) and kurtosis (3rd moment) (**Figure 3.5**).

Table 3.7 The thermodynamic properties of crystalline CO₂ at 1 atm, 50K/100K/150K. The subscripts of trans, rot, and vib represent as the translation, rotation, and vibration modes of 2PT, respectively. S_q is the quantum entropy obtained from 2PT analysis.

		FEPM2			CO ₂ -Fq		
T [K]	Theoretical entropy [J/mol/K]	T Decomposition from 2PT [K]	2PT entropy [J/mol/K]	fluidicity factor	T Decomposition from 2PT [K]	2PT entropy [J/mol/K]	fluidicity factor
50	16.19	T _{trans} = 47.07 T _{rot} = 47.14 T _{vib} =53.65	S _q = 14.38	f _{trans} = 0.00327785 f _{rot} = 0.011844	T _{trans} = 49.53 T _{rot} = 50.54 T _{vib} =50.06	S _q = 20.31	f _{trans} = 0.0033372 f _{rot} = 0.018596
100	37.42	T _{trans} = 96.60 T _{rot} = 96.97 T _{vib} =103.85	S _q = 38.23	f _{trans} = 0.0041886 f _{rot} = 0.021889	T _{trans} = 94.21 T _{rot} = 96.54 T _{vib} =105.72	S _q = 43.94	f _{trans} = 0.0045095 f _{rot} = 0.034896
150	55.92	T _{trans} = 146.21 T _{rot} = 146.25 T _{vib} =154.77	S _q = 56.4	f _{trans} = 0.0053767 f _{rot} = 0.029656	T _{trans} = 149.59 T _{rot} = 152.43 T _{vib} =149.34	S _q = 63.96	f _{trans} = 0.0051085 f _{rot} = 0.057985

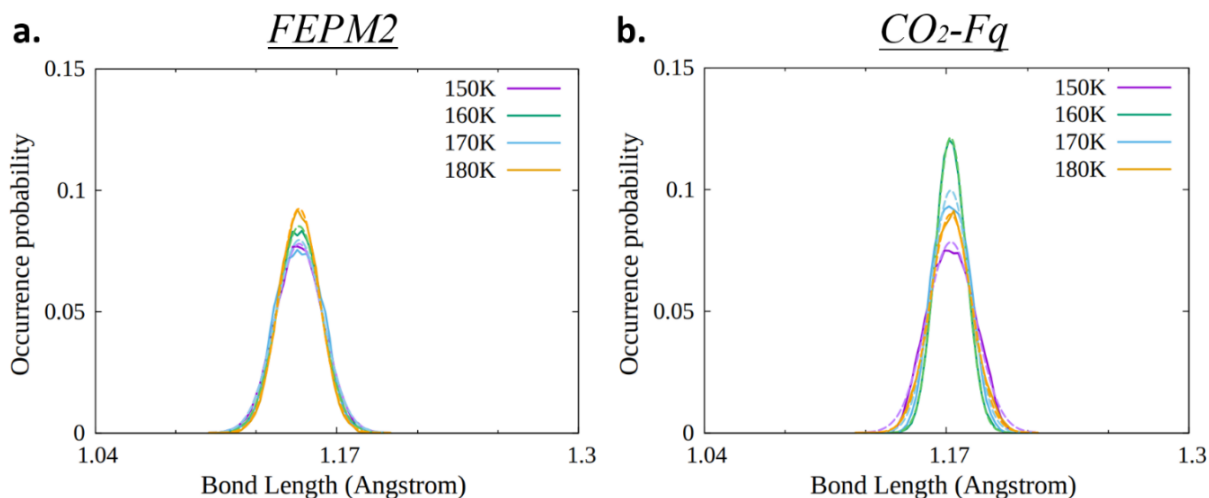


Figure 3.5 Probability distribution of the C-O bond lengths of crystalline CO₂ from equilibrium MD simulations at 150 – 180K and 1atm, using the FEPM2 (a) and CO₂-Fq (b) forcefields. We fit the simulation data (solid lines) to Gaussian functions (dashed lines).

3.5.3.2. Carbon Dioxide Thermodynamic properties at Vapor-Liquid Coexistence (VLE) conditions and Critical Point

In **Figure 3.6**, we plot the density - temperature relationship of the saturated liquid and saturated vapor systems. The VLE density increases monotonically with temperature until a certain condition (i.e., critical density) is met, after which, the VLE density decreases monotonically with temperature. Thus, along the VLE curve, that saturated vapor becomes more liquid-like and saturated liquid becomes more gas-like as they approach the critical point. In fact, we note that besides the density - temperature characteristics at the VLE condition, the 2PT fluidicity-factor (f-factor) can be used to determine the critical point. This is demonstrated in **Figure 3.6b** for the FEPM2 model, where we find that the turning point of the curves (infinite slope) is in excellent agreement with the critical point determined from the density. At this point,

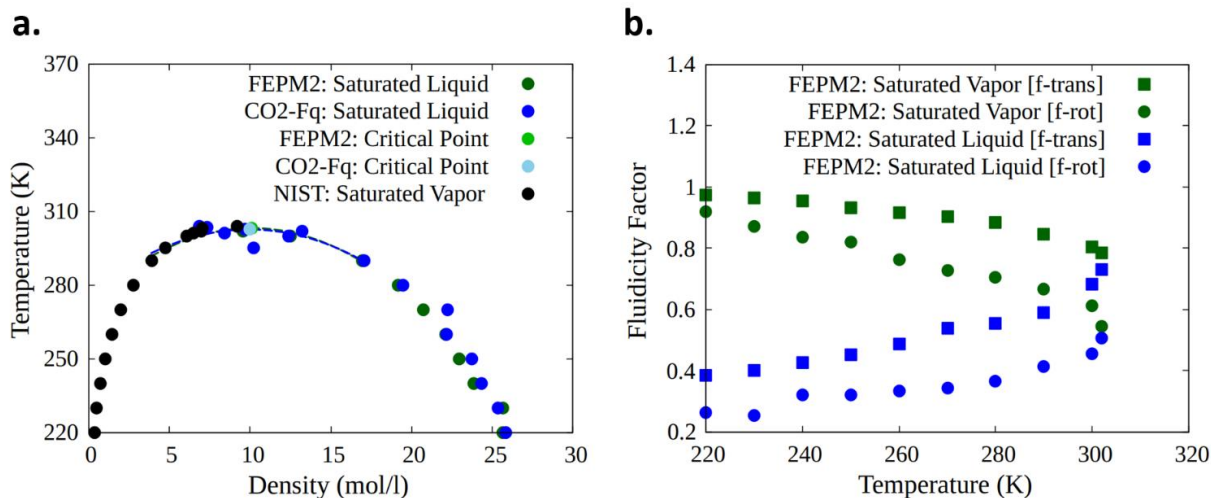


Figure 3.6 (a) The density – temperature relationship along the VLE curve and the critical point of CO₂ simulated with the FEPM2 and CO₂-Fq models (solid data points). Dashed curves are cubic spline fits to the calculated data. (b) The translational (trans) and the rotational (rot) fluidicity factors of FEPM2 model along the VLE curve.

the system can be described as equally liquid-like and gas-like, and the separate phases become indistinguishable.

Based on the results in **Figure 3.6**, we calculate a critical temperature (T_c) and a critical density (ρ_c) $T_c=303.1\text{K}$, $\rho_c=10.133\text{ mol/l}$ for the FEPM2 model. This can be compared to Harris et al.'s work [35] ($T_c = 313.4\text{ K}$ and $\rho_c = 10.31\text{ mol/l}$) for the original rigid EPM2 model. Further, we calculate $T_c=302.5\text{K}$, $\rho_c=9.9883\text{ mol/l}$ for the CO₂-Fq model. Both are in a good agreement with NIST database values ($T_c=304.18\text{K}$, $\rho_c=10.6\text{ mol/l}$). Detailed 2PT simulated data and experimental values are shown in **Table 3.8**.

Table 3.8 Thermodynamic properties of CO₂ along the VLE curve using the FEPM2 and CO₂-Fq models compared to experiments

	T	FEPM2				CO ₂ -Fq				EXP[63, 90]	
		ρ	$S_{q\ 2PT}$	$E_{md\ 2PT}$	$E_{q\ 2PT}$	ρ	$S_{q\ 2PT}$	$E_{md\ 2PT}$	$E_{q\ 2PT}$	S_{EXP}	E_{EXP}
Saturated liquid	220	1.1663	113.74	17.25	17.25	1.1663	116.01	17.25	17.25	118.12	17.25
	230	1.1292	115.70	17.95	18.42	1.1292	118.25	18.27	17.86	121.59	18.06
	240	1.0896	120.40	19.60	19.51	1.0896	124.41	19.32	20.60	125.07	18.88
	250	1.0467	125.81	20.59	19.60	1.0467	126.37	20.27	19.81	128.64	19.74
	260	1.0000	128.19	21.71	21.12	1.0000	130.87	21.78	20.37	132.24	20.65
	270	0.9470	133.91	22.91	21.19	0.9470	132.53	22.42	21.50	135.94	21.61
	280	0.8850	136.71	24.36	23.20	0.8850	139.30	24.27	22.07	139.77	22.64
	290	0.8058	142.56	25.87	23.40	0.8058	145.01	25.82	23.47	143.95	23.81
	300	0.6803	151.21	28.29	25.85	0.6803	151.45	28.25	25.18	149.32	25.33
	302	0.6337	154.50	29.67	27.97	0.6337	152.20	28.03	26.20	--	--
Critical point	303.1 (FEPM2)										
	302.5 (CO ₂ -Fq)	0.4459	155.30	29.53	27.03	0.4395	155.51	29.45	26.76	--	--
Saturated vapor	302	0.3082	159.00	30.78	28.59	--	--	--	--	--	--
	300	0.2703	162.20	30.95	28.25	--	--	--	--	164.68	29.28
	290	0.1724	168.07	31.40	29.02	--	--	--	--	169.61	30.19
	280	0.1220	170.03	31.65	29.57	--	--	--	--	172.73	30.59
	270	0.0885	172.78	31.42	28.79	--	--	--	--	175.20	30.78
	260	0.0645	174.80	31.34	29.14	--	--	--	--	177.44	30.86
	250	0.0467	179.26	30.79	29.82	--	--	--	--	179.51	30.87
	240	0.0333	182.10	30.47	29.46	--	--	--	--	181.67	30.82
	230	0.0234	182.60	30.05	29.86	--	--	--	--	183.35	30.74
	220	0.0160	184.86	29.57	29.90	--	--	--	--	186.71	30.62

T is the temperature in K, ρ is the initial density in g/cm³, S_q is the entropy in J/mol/K, E_{md} is the internal classical energy in kJ/mol and E_q is the internal quantum energy in kJ/mol. The energy referent state is set as saturated liquid at 220K.

3.5.4. The Carbon Dioxide Phase Diagram based on phase stability and the 2PT method

As previously elaborated, we constructed the phase diagram by explicitly considering the Gibbs energy of the isolated phases at specific points on the P-T diagram. Such an approach is only possible due to the ability to compute the absolute entropy of the phases from short MD simulations using the 2PT method. This last point is important, since near the phase boundaries, we can expect significant fluctuations in the thermodynamic potentials over long-term dynamics. In fact, for 1st order phase transitions, the Gibbs energy function is discontinuous near the phase boundary. In **Figure 3.7** we plot the Gibbs energy, entropy and enthalpy of liquid/solid systems for both FEPM2 and CO₂-Fq models as a function of temperature at 100atm, showing the system transitions from a solid ($G^S < G^L$) to a liquid ($G^S > G^L$). We note that the FEPM2 enthalpies are computed with quantum (zero-point energy) corrections, while CO₂-Fq enthalpies exclude the quantum corrections for consistency with the gas phase reference.

We found that the fluctuations in the Gibbs energy were larger in the FEPM2 forcefield compared to CO₂-Fq, which led to larger uncertainties in the relevant phase boundaries. For example, at 100atm we were unable to cleanly resolve the melting temperature (T_m) of the FEPM2 model by inspection, and instead had to determine T_m by fitting to a cubic interpolation function, resulting in $T_m = 232 \pm 5$ K. The thermodynamics of the isolated phases are more well behaved in CO₂-Fq and the predicted $T_m = 217 \pm 1$ K is in much better agreement with the experimental value of 218.6 K. Overall, we find closer agreement of the experimental phase boundaries with the CO₂-Fq forcefield, especially in the high-pressure regime, which we attribute to an improved description of the repulsive inner wall by application of UNB nonbond potential over the Lennard Jones 12-6 potential in FEPM2.

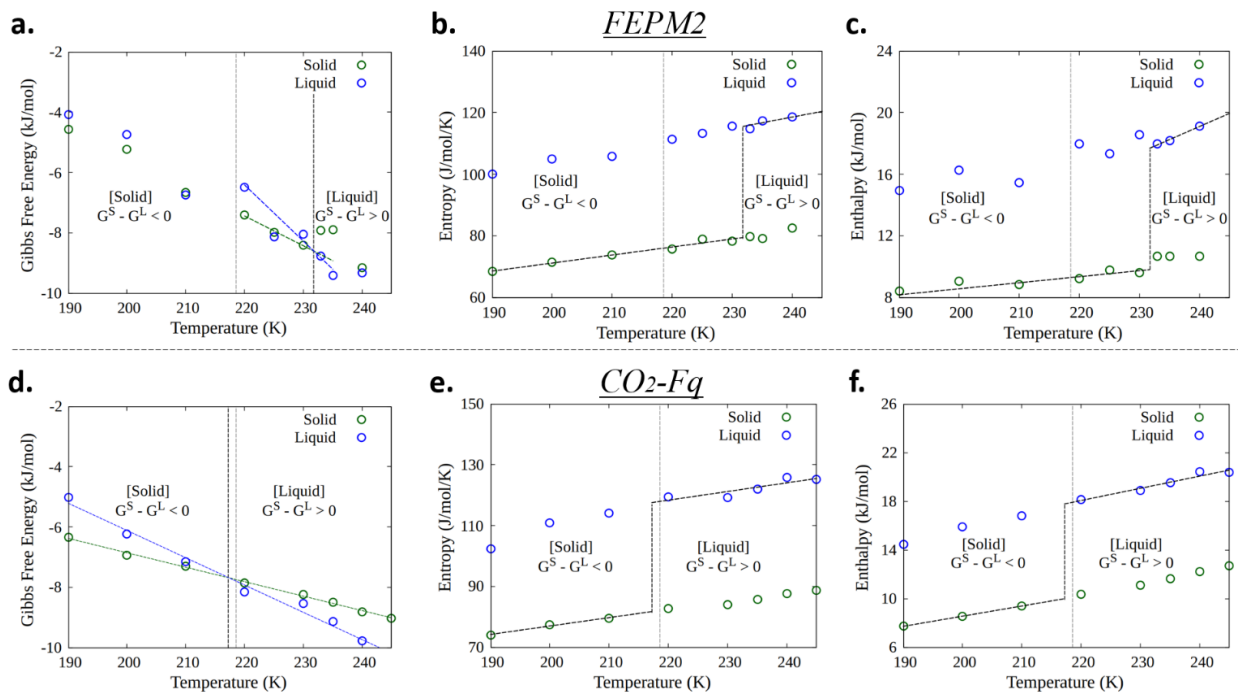


Figure 3.7 The thermodynamics of CO_2 described by the FEPM2 and CO_2 -Fq models at 100atm as the system undergoes a 1st order phase transition. The FEPM2 total Gibbs energy (a), the separate entropy (b), and enthalpy (c) contributions, and the CO_2 -Fq total Gibbs energy (d), the separate entropy (e), and enthalpy (f) contributions are shown. The dashed green line and dashed blue line represent the fitted lines in determining the phase transition temperatures via interpolation (CO_2 -Fq) and extrapolation (FEPM2). The dashed black lines demonstrate the simulated phase changes – FEPM2 of 232 K and CO_2 -Fq of 217 K, which can be compared to the experimental value of 218.6 K - shown as the dashed gray lines.

In **Figure 3.8** we present the entire phase diagram of CO_2 , where the phase boundaries are taken as the points in P-T space, where the phases have equal chemical potentials. Here again, we note that the larger fluctuations in the Gibbs energy of FEPM2 obscures exact determination of the phase boundaries, so we apply to interpolation scheme employed in the Section 3.4.9. and considered two (or more) phases to have the same chemical potentials if the difference in the Gibbs energies (ΔG) are within 5%. In the case of the CO_2 -Fq model, we were able to resolve the phase boundaries with a much more stringent condition $\Delta G < 0.3\%$.

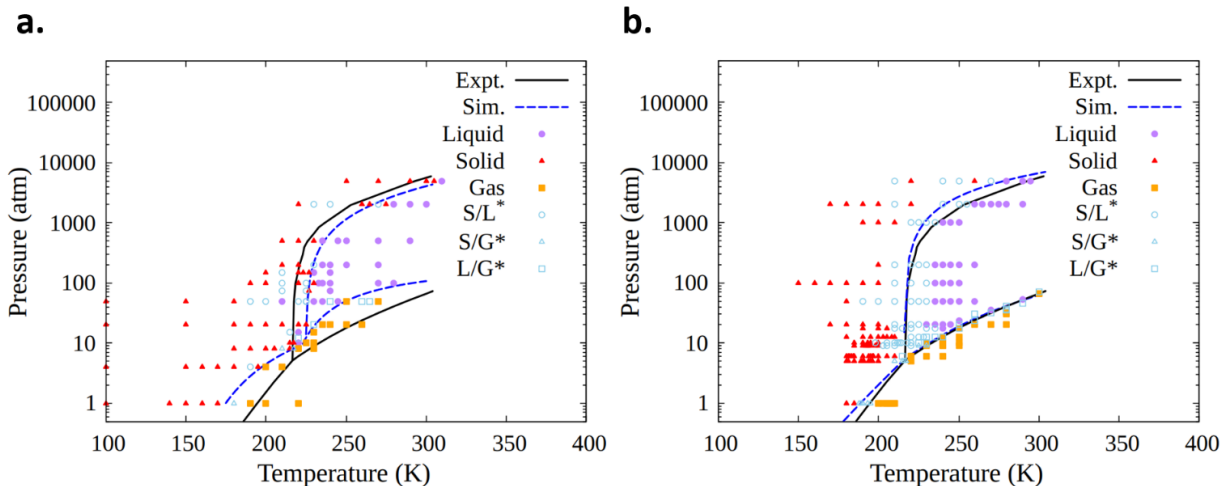


Figure 3.8 The CO₂ phase diagram, based on the Gibbs energy of the isolated solid, liquid and gas phases, using the FEPM2 (a) and the CO₂-Fq (b) models. The superscript * means the ΔG is smaller than 5% between solid/liquid (S/L*), solid/gas (S/G*) or liquid/gas (L/G*) systems for the FEPM2, and smaller than 0.3% for the CO₂-Fq model. The dashed blue curves are the simulated phase boundaries of FEPM2 and CO₂-Fq models. The experimental reference is from the Global CCS Institute (solid black lines)

Overall, we find improved prediction of the phase diagram using the CO₂-Fq model, compared to experiments. In addition to the improved van der Waals interaction mentioned previously, the additional charge degree of freedom in CO₂-Fq leads to more a more accurate representation of the intermolecular physics by facilitating additional instantaneous dipole interactions that stabilizes the liquid. We also obtained encouraging results when considering the triple point. Our interpolation procedure yields an approximate triple point temperature (T_t) and the triple point pressure (P_t) of $T_t = 218.0 \pm 5.0$ K, $P_t = 8.2 \pm 1.1$ atm using the FEPM2 model and $T_t = 216.2 \pm 3.0$ K, $P_t = 5.5 \pm 0.5$ atm using the CO₂-Fq model, both in good agreement with the experimental values from the NIST database: $T_t = 216.6$ K, $P_t = 5.12$ atm. Here again, the CO₂-Fq model led to marked improved results compared to experiments, over FEPM2. While these results are indeed encouraging, we note that one potential limitation of the current approach is that stabilization of the isolated phases near the phase boundaries is rather difficult, even on the

relatively short timescale of the 2PT trajectories. We overcome this here by interpolation near the phase boundaries, however this introduces some additional uncertainties in our calculations.

3.6. Conclusions and Outlook

In this work, we employed a fixed atom-charge model FEPM2 and a QM-derived fluctuating charge model CO₂-Fq to calculate the phase diagram of CO₂ from equilibrium MD simulations of the isolated phases and the 2PT method. We find that relatively short trajectories (~200ps) are sufficient for capturing the thermodynamics of the solid and liquid phases, while the gas phase require longer windows (~2ns). This means that the entire phase diagram was obtained from MD simulations on the ns timescale, and since the 2PT method does not incur any appreciable extra computational cost, this presents a rather efficient approach for determining phase diagram. Overall, the FEPM2 model predicts the phase behavior thermodynamics in reasonable agreement with experiments, especially at low temperatures and pressures. At higher pressures, the inability of the Lennard Jones 12-6 potential to adequately represent the repulsive Pauli forces and the inability to model charge renormalization within the molecule leads to larger deviations. The CO₂-Fq thus improves on the FEPM2, by including the many body QM physics, leading to excellent agreement with experiments over the entire phase diagram. This improved description may be important for study CO₂ in extreme environments, such as the controversial high pressure polymeric phase [110, 111] and its associated thermodynamics. We note that, as mentioned in Section 3.4.8., the QEq approach leads to spurious long-range charge transfer between molecules. This can be remedied by QEq reformulations that constrain the total molecular charge and prevent inter-molecular charge transfer [85, 112] Alternative, we suggest adopting the ideal gas treatment, detailed in Section 3.4.8., with CO₂-Fq model for low-density CO₂ environments.

This work provides an efficient approach for calculating phase diagrams, which should be applicable to arbitrary systems. We are currently applying to approach to study other homogeneous liquids, including water. Considerations of multi-component systems are a natural extension, and insights into the behavior of the separate entropic and enthalpic functions are currently being explored.

3.7. Acknowledgements

Chapter 3, in full, is a modified version of the published materials – Amanda A. Chen, Alexandria Do, and Tod A. Pascal. “The Phase Diagram of Carbon Dioxide from Correlation Functions and a Many-body Potential” (2021), on The Journal of Chemical Physics. The dissertation author is the primary author who conducts the investigation and analyzation on this work.

CHAPTER 4 : Sub-Nanometer Confinement Enables Facile Condensation of Gas Electrolyte for Low-Temperature Batteries

Chapter 4 adopted materials from G. Cai, Y. Yin, D. Xia, A.A. Chen, J. Holoubek, J. Scharf, Y. Yang, K.H. Koh, M. Li, D.M. Davies, M. Mayer, T.H. Han, Y.S. Meng, T.A. Pascal, and Z. Chen. “Sub-Nanometer Confinement Enables Facile Condensation of Gas Electrolyte for Low-Temperature Batteries” *Nature Communications*, 12(1), 1-11 (2021), which is under a Creative Commons Attribution 4.0 license. Changes were made for concentrating the theoretical backbone. To view a copy of this license, visit <http://creativecommons.org/licenses/by/4.0/>.

4.1. Abstract

Confining molecules in the nanoscale environment can lead to dramatic changes of their physical and chemical properties, which opens possibilities for new applications. There is a growing interest in liquefied gas electrolytes for electrochemical devices operating at low temperatures due to their low freezing point. However, their high vapor pressure still poses potential safety concerns for practical usages. Herein, we report facile capillary condensation of gas electrolyte by strong confinement in sub-nanometer pores of metal-organic framework (MOF). As the results, we show significant uptake of hydrofluorocarbon molecules in MOF pores at pressure lower than the bulk counterpart. The investigation of the FM molecule behaviors provides insight on future battery design at low-temperature condition.

4.2. Introduction

Batteries that can sustain ultralow temperatures ($< -30\text{ }^{\circ}\text{C}$) are essential for extending the operation capability of existing energy storage systems as well as enabling human presence to the outer space and deep ocean worlds.[113-117] The state-of-the-art lithium-ion batteries (LIBs) are mostly restricted to perform in mild conditions due to the drastically decreased ionic conductivity and increased charge transfer impedance of electrode/electrolyte interfaces at ultra-low temperatures,[113-123] despite that some cells like lithium-thionyl chloride batteries are capable of operation down to $-80\text{ }^{\circ}\text{C}$ for low power applications.[124-126] Although many approaches (*e.g.*, externally/internally heating, cell insulating, and introducing co-solvents or additives) have been developed to overcome the above issues,[117-123] no current technology extends the operating temperature range of batteries without sacrificing the long-term stability and energy density.

Unlike conventional liquid/solid electrolyte chemistries, liquefied hydrofluorocarbon gas molecules like fluoromethane (FM) shows a low melting point ($-142\text{ }^{\circ}\text{C}$) and low viscosity ($0.085\text{ mPa}\cdot\text{s}$), which enable electrolytes with high ionic conductivity and superior lithium metal compatibility down to temperatures as low as $-60\text{ }^{\circ}\text{C}$.[127-129] To retain the electrolyte in the liquid state, the gas molecules need to be maintained at its vapor pressure (P_v). However, the saturated vapor pressure for these gas molecules is very high ($P_{\text{sat, FM}} = 495\text{ psi}$ or 33 atm at $20\text{ }^{\circ}\text{C}$), which would render safety concerns in practical devices.

To address the above-mentioned limitation, it is conceivable to exploit capillary condensation, a phenomenon whereby gas molecules in small confined pores condense into a

liquid at an equilibrium pressure P_v that is lower than the bulk vapor pressure P_{sat} . [130, 131] The relationship between the P_v and the P_{sat} follows the Kelvin equation:

$$\ln \frac{P_v}{P_{sat}} = \frac{2\gamma V_L}{rRT} \quad (4.1)$$

where γ is the liquid/vapor surface tension, V_L the molar volume of the liquid adsorbate, r the mean radius of curvature of the liquid/gas interface (proportional to pore radius), R the universal gas constant, and T the absolute isothermal temperature. Generally, smaller r values enable a lower P_v to condense gas molecules at a given temperature (**Figure 4.1**). [132-134] For example, both simulation and experimental results show that the actual pressure required to condense nitrogen molecules in porous carbon (slit-shaped pores) reduces by > 10 times as the pore diameter decreases from 7 nm to 1 nm. [135] Similar trends have also been observed for methane absorption and condensation in nanopores. [136] Hydrofluorocarbons share some similar physicochemical

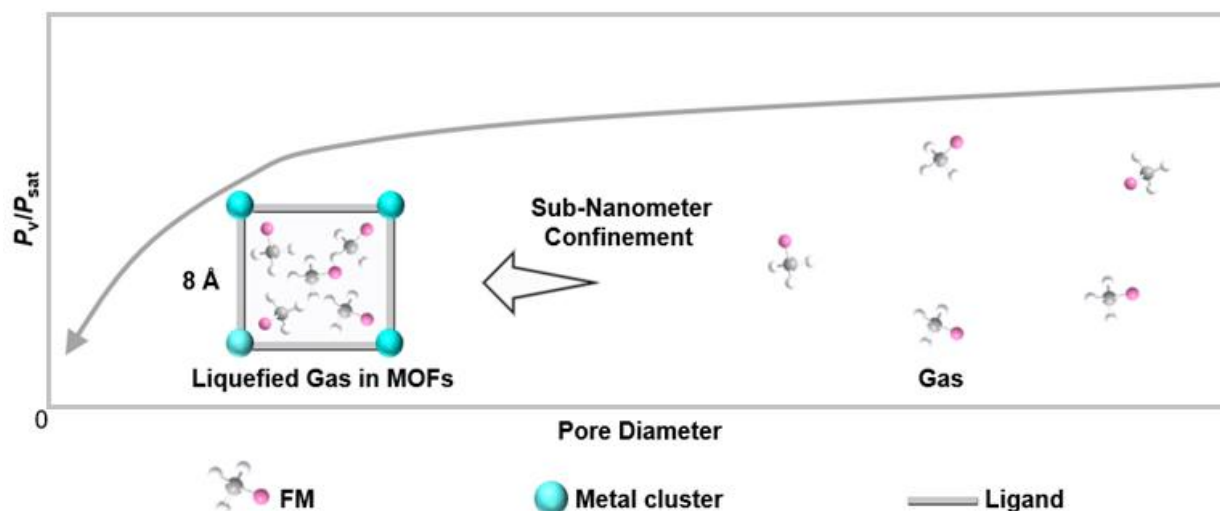


Figure 4.1 Schematic showing the mechanism of nano-confinement effects for lowering the equilibrium pressure of liquefied gas, where MOFs were employed as the porous hosts to condense the gas molecules under a lower P_v than P_{sat} , attributed to the driving force of the sub-nanometer confinement of MOFs. [137]

characteristics with methane (*e.g.*, high vapor pressure, low melting point), yet capillary condensation of hydrofluorocarbon has not been explored, nor has there been a study reporting the design of a stable nanoporous host to condense gas molecules at reduced pressures for electrochemical applications.

Metal-organic frameworks (MOFs), a class of porous crystalline solids assembled by organic linkers and metal ions/clusters, could be ideal candidates to capture FM molecules via capillary condensation to lower the inner pressure of batteries employing liquefied gas electrolytes (LGE).[138-140] Various MOFs have been successfully applied for the storage or separation of carbon dioxide, methane, and alkene molecules.[136, 141-143] Herein, we investigated the phase transitions for free FM molecules and confined FM molecules and explored the dynamics of confined FM to determine the capillary condensation of FM gaseous electrolytes. This study not only provides the insights on the molecular behavior in the nano-confined environment but also opens a potential pathway for safer operation of gas electrolytes.

4.3. Theoretical and Computational Analysis

4.3.1. Computational Investigation

Insights into the microscopic interactions between FM and UiO-66 were acquired from computer simulations (**Figure 4.2**). Both quantum mechanics (QM) calculations and molecular dynamic simulations were applied. In **Table 4.1**, we described the intermolecular and intramolecular parameters of UiO-66 and FM, where the FM properties were obtained via QM calculations at the MP2/aug-cc-pVTZ level of theory using the Q-Chem 5.0 electronic structure

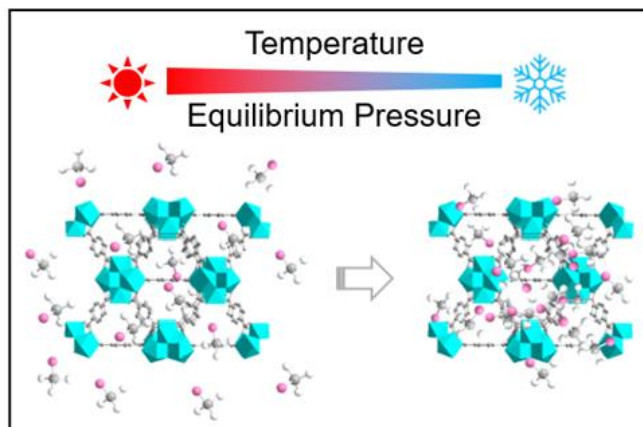


Figure 4.2 Schematic showing the adsorption behavior of FM in UiO-66 at different conditions.

Table 4.1 Simulation parameters applied in MD/GCMC computations. The inter-/intra- molecular parameters of UiO-66 were taken from published works.[144, 145] FM molecule structure was optimized to obtain inter-/intra- molecular parameters based on QM calculations at the MP2/aug-cc-pVTZ level of theory, with the partial atom charges taken from a published work.[146] CO₂ and CH₄ were described by the TraPPE-EH and TraPPE-UA forcefields respectively.[147]

Materials	Types	Equations	Parameters	
FM	Pair interaction	Lennard-Jones	C	$\sigma = 3.304; \epsilon = 0.0980; M = 12.01$
			H	$\sigma = 2.385; \epsilon = 0.0456; M = 1.01$
			F	$\sigma = 2.671; \epsilon = 0.1165; M = 19.00$
	Bond	Rigid (GCMC) Harmonic (MD)	C-F	Rigid: $r_0 = 1.389$ Harmonic: $r_0 = 1.389; K = 368$
			C-H	Rigid: $r_0 = 1.087$ Harmonic: $r_0 = 1.087; K = 333.5$
	Angle	Rigid (GCMC) Harmonic (MD)	H-C-H	Rigid: $\theta_0 = 110.3$ Harmonic: $\theta_0 = 110.3; K = 34.79$
			H-C-F	Rigid: $\theta_0 = 108.6$ Harmonic: $\theta_0 = 108.6; K = 40.00$
	Charges[146]		C	-0.2469
			F	-0.1950
			H	+0.1473

Table 4.1 Simulation parameters applied in MD/GCMC computations. The inter-/intra- molecular parameters of UiO-66 were taken from published works.[144, 145] FM molecule structure was optimized to obtain inter-/intra- molecular parameters based on QM calculations at the MP2/aug-cc-pVTZ level of theory, with the partial atom charges taken from a published work.[146] CO₂ and CH₄ were described by the TraPPE-EH and TraPPE-UA forcefields respectively.[147] (Continued)

FM/UiO-66	Pair interaction	Lennard-Jones	C(FM)-Zr1(UiO-66)	$\sigma = 3.485; \epsilon = 0.0535$
			F(FM)-Zr1(UiO-66)	$\sigma = 3.134; \epsilon = 0.0583$
			H(FM)-Zr1(UiO-66)	$\sigma = 2.961; \epsilon = 0.0365$
			C(FM)-O1(UiO-66)	$\sigma = 3.498; \epsilon = 0.0673$
			F(FM)-O1(UiO-66)	$\sigma = 3.145; \epsilon = 0.0734$
			H(FM)-O1(UiO-66)	$\sigma = 2.972; \epsilon = 0.0459$
			C(FM)-C25(UiO-66)	$\sigma = 3.966; \epsilon = 0.0503$
			F(FM)-C25(UiO-66)	$\sigma = 3.566; \epsilon = 0.0548$
			H(FM)-C25(UiO-66)	$\sigma = 3.370; \epsilon = 0.0343$
			C(FM)-O29(UiO-66)	$\sigma = 3.498; \epsilon = 0.0673$
			F(FM)-O29(UiO-66)	$\sigma = 3.145; \epsilon = 0.0734$
			H(FM)-O29(UiO-66)	$\sigma = 2.972; \epsilon = 0.0459$
			C(FM)-O25(UiO-66)	$\sigma = 3.633; \epsilon = 0.0875$
			F(FM)-O25(UiO-66)	$\sigma = 3.266; \epsilon = 0.0954$
			H(FM)-O25(UiO-66)	$\sigma = 3.086; \epsilon = 0.0597$
C(FM)-C1(UiO-66)	$\sigma = 4.128; \epsilon = 0.0581$			
F(FM)-C1(UiO-66)	$\sigma = 3.712; \epsilon = 0.0633$			
H(FM)-C1(UiO-66)	$\sigma = 3.507; \epsilon = 0.0396$			
C(FM)-C13(UiO-66)	$\sigma = 4.118; \epsilon = 0.0416$			
F(FM)-C13(UiO-66)	$\sigma = 3.702; \epsilon = 0.0453$			
H(FM)-C13(UiO-66)	$\sigma = 3.498; \epsilon = 0.0284$			
C(FM)-H1(UiO-66)	$\sigma = 3.211; \epsilon = 0.0458$			
F(FM)-H1(UiO-66)	$\sigma = 2.887; \epsilon = 0.0499$			
H(FM)-H1(UiO-66)	$\sigma = 2.728; \epsilon = 0.0312$			
C(FM)-H25(UiO-66)	$\sigma = 0.0; \epsilon = 0.0$			
F(FM)-H25(UiO-66)	$\sigma = 0.0; \epsilon = 0.0$			
H(FM)-H25(UiO-66)	$\sigma = 0.0; \epsilon = 0.0$			
The units of energy, distance, angle, mass and charge are kcal/mol, Angstrom, degree, g/mol and electron charge, respectively. Lennard-Jones equation is $E = 4\epsilon[(\sigma/r)^{12} - (\sigma/r)^6]$. Harmonic equations are $E = K(r-r_0)^2$ (for bond) and $E = K(\theta - \theta_0)^2$ (for angle).				

package.[2] Initially, we optimized the UiO-66 starting structure (**Figure 4.3**) using molecular dynamics (MD) simulations via the Large-scale Atomic/Molecular Massively Parallel Simulator (LAMMPS) simulation engine.[1] The loading curves of FM in UiO-66 were then obtained from the optimized structure by means of Grand Canonical Monte-Carlo (GCMC) simulations using the MCCCSTowhee simulation package.[148] The accuracy of our GCMC approach was confirmed by comparing the adsorption isotherms of CH₄ and CO₂ to other published works as shown in **Figure 4.4**. [149, 150] All simulated adsorption isotherms of FM in UiO-66 at variable temperatures exhibited a classical type I isotherm of micropore adsorption (**Figure 4.5**), in which UiO-66 achieved a 10% mass uptake of FM at 140 psi and 25 °C, in good agreement with our experiments (9% mass uptake at 140 psi, 25 °C). In addition, it was found that the FM density increased from 0.3 mol L⁻¹ in bulk FM to 3 mol L⁻¹ in the confined pores in UiO-66 at 100 psi, 25 °C (**Figure 4.6**). We quantified the capillary condensation of FM in UiO-66 by considering the thermodynamics of the equilibrated system using the Two-Phase Thermodynamics Method.[64, 74] In particular, we determined the phase change behavior of FM by a novel approach, considering the self-diffusion constant of FM and the number of FM modes that were diffusive (**Figure 4.7**). This approach is necessary because while the phase boundaries of a bulk homogenous fluid are given by solutions to the Clausius-Clapeyron equation,[151] computational schemes typically rely on locating discontinuities in the relevant thermodynamic functions, such as the molar enthalpy.[103] In the particular case of FM in UiO-66, we found that the molar enthalpy function showed significant uncertainty, especially at low pressures, which obscured unambiguous determination of possible phase boundaries. We found less variability in the calculated self-diffusion constants however, which we used to determine the number of modes of FM that were diffusive.

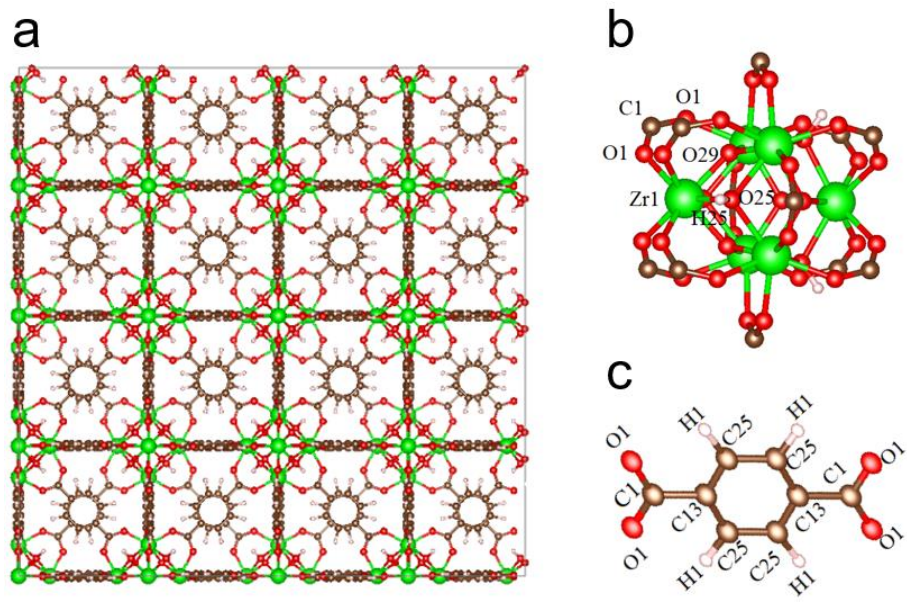


Figure 4.3 Simulation structure of UiO-66. The simulation structure for (a) UiO-66, composing of (b) $[Zr_6O_4(OH)_4]$ clusters and (c) BDC linkers.

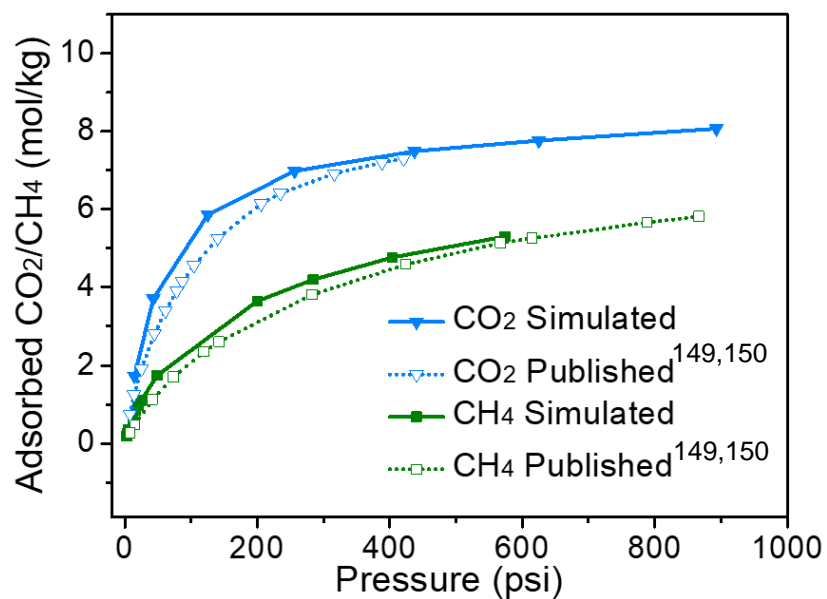


Figure 4.4 Simulated adsorption isotherms of UiO-66 confined CH_4 and CO_2 at room temperature, compared to other published data.[149, 150] We find overall excellent agreement with published data, validating our current simulation approach.

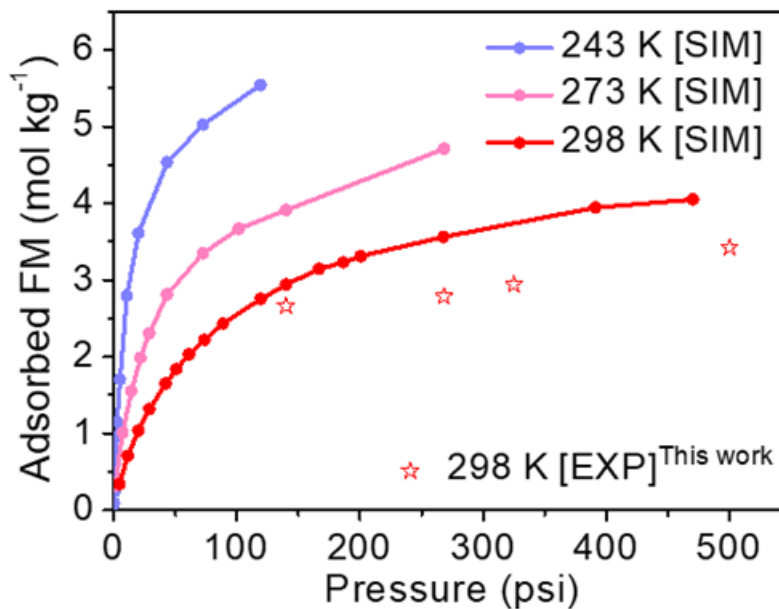


Figure 4.5 Simulated (SIM) adsorption isotherms of UiO-66 confined FM at different temperatures and experimental (EXP) results at 25 °C.

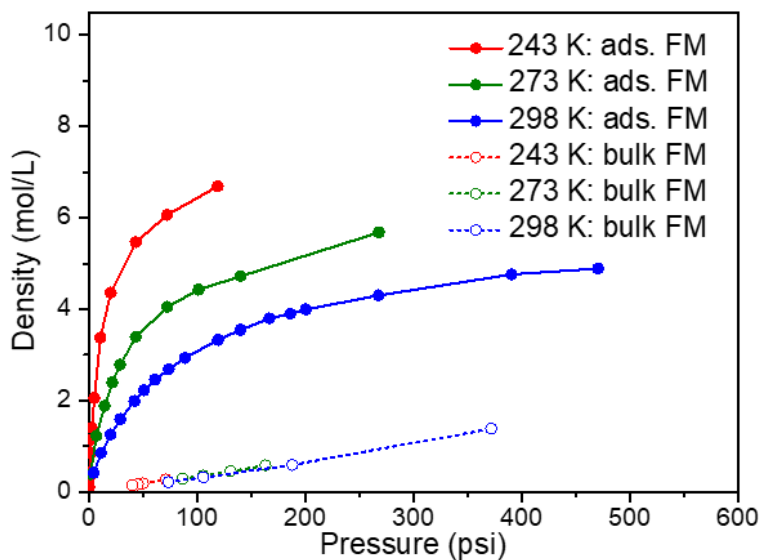


Figure 4.6 The densities comparison between adsorbed FM inside UiO-66 and free FM in bulk FM systems. The solid curves represent the FM densities inside UiO-66 and the dashed curves indicate the bulk FM densities, at the stated temperatures.

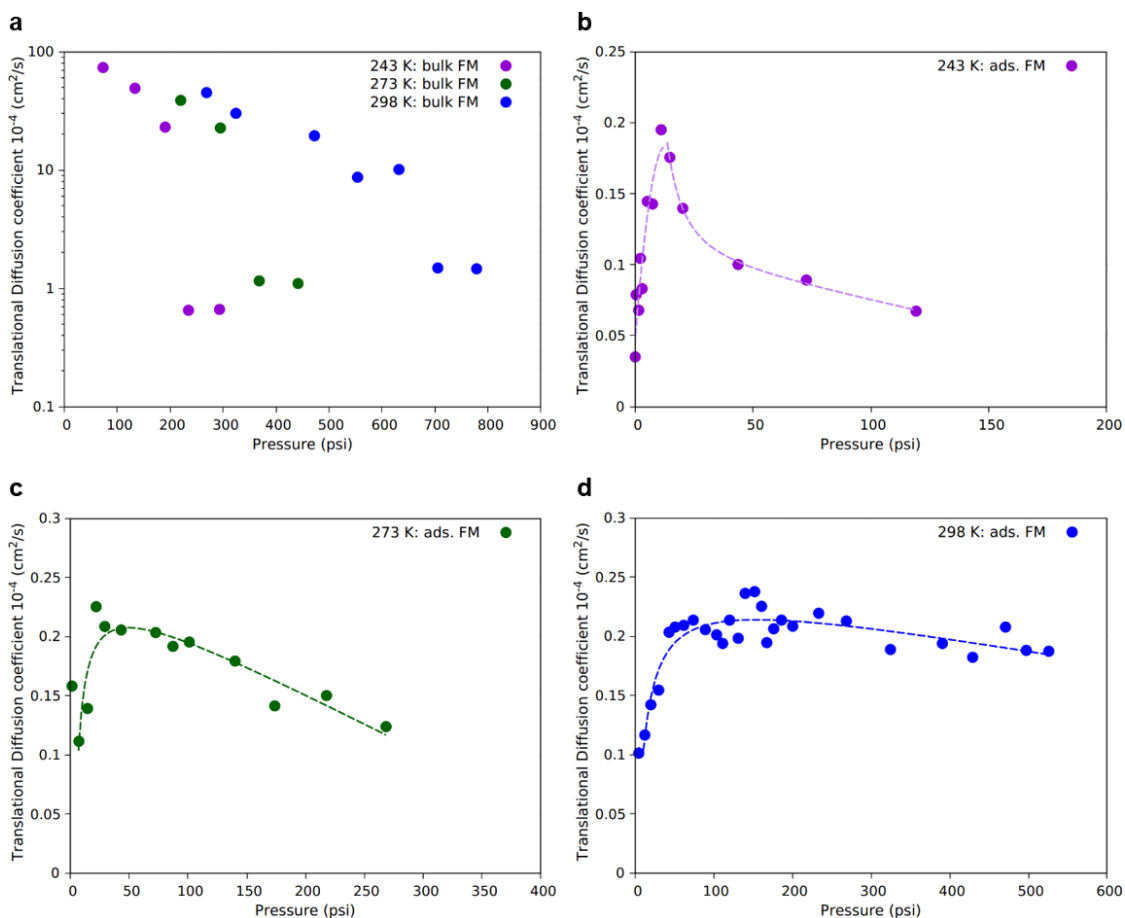


Figure 4.7 Simulated translational diffusion coefficients. Simulated translational diffusion coefficients of (a) bulk FM, and (b, c, d) adsorbed FM (ads. FM) in UiO-66 at different temperatures and pressures.

Figure 4.7a-d show the translational diffusion coefficient of bulk FM and adsorbed FM systems. In adsorbed FM systems, we find that as the pressure increases, the translational diffusion coefficient gradually increases until a certain pressure (the phase transition point), after which the translational diffusion coefficient monotonically decreases with increasing pressure. The reduced intermolecular distances between (gaseous) FM molecules before the transition pressure results in weaker attractive forces and an increase in the translational diffusion coefficient. After the phase transition, the compressed, liquefied FM molecules experiences reduced translational degrees of

freedom, and are less diffusive. It is shown that the transition conditions (pressures/translational-diffusion-coefficients) of adsorbed FM models at 243 K, 273 K, and 298 K occurred at about 10.8 psi/ $2.0 \cdot 10^{-5} \text{ cm}^2 \text{ s}^{-1}$, 21.7 psi-43.5 psi/ $2.1 \cdot 10^{-5} \text{ cm}^2 \text{ s}^{-1}$ - $2.3 \cdot 10^{-5} \text{ cm}^2 \text{ s}^{-1}$, and 103 psi-200 psi/ $1.9 \cdot 10^{-5} \text{ cm}^2 \text{ s}^{-1}$ - $2.4 \cdot 10^{-5} \text{ cm}^2 \text{ s}^{-1}$, respectively. It is noted that at 25 °C, the decrease in the translational diffusion coefficient after the phase transition pressure is not apparent, due to the fact that the FM is approaching its critical properties. The **Figure 4.8** plots the phase transitions points for bulk FM, compared to adsorbed FM in UiO-66. We find that FM experienced a phase transition at significantly lower pressures in UiO-66, compared to the bulk fluid. In particular, capillary condensation in UiO-66 resulted in liquefied FM at an approximated pressure of 44 psi compared to NIST value of 296 psi in the bulk tank at 0 °C, and at an approximated pressure of 11 psi compared to 118 psi at -30 °C, respectively.

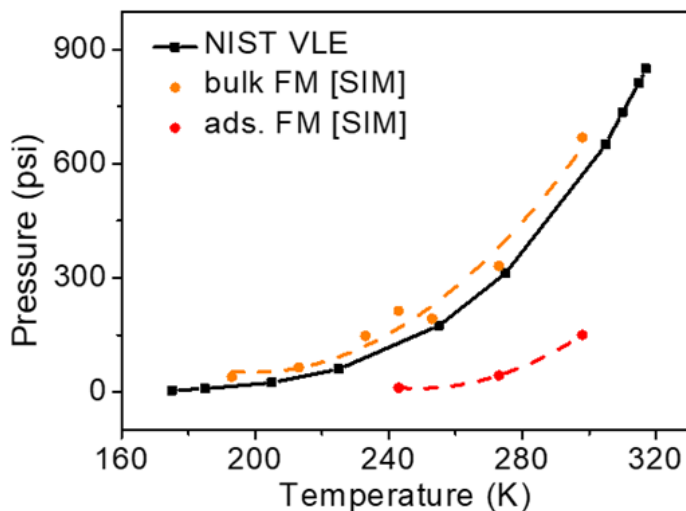


Figure 4.8 Phase transition comparison between bulk FM taken from NIST database, simulated (SIM) bulk FM and simulated (SIM) adsorbed (ads.) FM in UiO-66 systems, where the orange and the red points represent as the phase transitions of bulk FM and adsorbed FM (ads. FM) in UiO-66, respectively.

4.3.2. Computational Details

4.3.2.1. Grand Canonical Monte-Carlo (GCMC) simulations in determining the loading curves

GCMC simulations (the MCCCCS Towhee simulation package[148]) were applied to model the molecules' loading value inside the optimized UiO-66 structure. GCMC is a procedure involving insertion/deletion molecules between a system and a reservoir to eventually make system/reservoir in thermodynamic equilibrium, under conditions of constant chemical potential (μ), volume (V) and temperature (T). For each GCMC computation, 3 million moves were performed, and we tested that convergence was obtained in each simulation. The initial 2 million moves were used to equilibrate the system, while the last 1 million moves were used to obtain the relevant statistics and absorption capacities. Besides the FM/UiO-66 models, the adsorption isotherms of CH₄ and CO₂ inside UiO-66 were also calculated in order to confirm the accuracy of our GCMC approach, as shown in **Figure 4.4.**[149, 150] After the adsorption capacity of FM were determined, the final snapshot of the system was used as input for further MD simulations.

4.3.2.2. MD simulations of FM/UiO-66 and UiO-66 systems

We initiated each MD simulation with a geometry optimization at 0 K, comprising 500 steps of conjugated gradient (CG) minimization (cell coordinates and atom positions) followed by 10 ps of canonical (constant particles, volume and temperature or NVT) dynamics to heat the system from 1 K to the defined temperature. This was followed by iso-thermal iso-baric (constant particles, pressure, and temperature or NPT) dynamics for 1ns at the required pressures, followed another 0.8 ns NVT dynamics to further equilibrate the system. The last 0.2 ps NVT data was used

to collect thermodynamic statistics and to analyze the system properties. In all our MD simulations, the temperature damping constant was 0.1 ps, and the pressure damping constant was 2.0 ps. The equations of motion used are those of Shinoda *et al.*,[152] which combine the hydrostatic equations of Martyna *et al.*[153] with the strain energy proposed by Parrinello and Rahman.[154] The time integration schemes closely follow the time-reversible measure preserving Verlet integrators derived by Tuckerman *et al.*[155]

4.3.2.3. MD simulations of bulk FM systems

For bulk FM, a simulation cell comprising 216 molecules at the 298 K saturated vapor density (2.7688 mol L⁻¹ from NIST database) was subjected to 500 steps of CG minimization, followed by 10 ps of Langevin dynamics to heat the system from 1 K to a defined temperature. This was followed by 1 ns of NPT dynamics, and a further 5.5 ns of Langevin dynamics to properly equilibrate the system. Longer simulation times, compared to FM/UiO-66 and UiO-66 systems, and the application of Langevin dynamic were to ensure thermal equipartition of the energy, due to the low density of the bulk FM system. After equilibration, we ran a further 0.7 ns of NVT dynamics, with statistics collected during the last 0.2 ps used to analyze the system properties. The temperature and pressure damping constants were the same as above.

4.3.2.4. Self-diffusion constant

The self-diffusion constant D was obtained using the Green-Kubo VAC formulism in linear response theory:[103]

$$D = \frac{1}{N} \sum_1^N \int_0^\infty \langle v_i(t) v_i(0) \rangle dt \quad (4.2)$$

where t is time, v_i the axial COM velocity of molecule i and the brackets denote an autocorrelation that is summed over all molecules. These calculations were obtained from additional simulations in the NVT ensemble, after pressure equilibration has been achieved. Snapshots of the system (atomic coordinates and velocities) were saved every 1 fs during a 0.5 ns simulation. Statistical averaging was performed by using 10 windows of 50 ps each. Our previous work has shown that trajectory windows of 50 ps were long enough to have converged self-diffusion constants by this approach.[74]

4.4. Experimental Analysis

In addition to the computation analysis, experimental investigations have also been conducted to demonstrate consistent insights as computations by our collaborated group of Prof. Zheng Chen. Details of synthesis, characterization, and the process of electrochemical measurements were mentioned in our published paper [156]. Here, we provided an overview of the experimental outcomes.

4.4.1. The adsorption behavior of FM in UiO-66

In order to quantify the FM absorption capability of UiO-66, a direct measurement of FM uptake in the UiO-66 powders was performed after immersing the UiO-66 powders into FM with various pressures for three days. After purging out the bulk FM from the customized high-pressure cell, the total mass of the soaked UiO-66 powders was *in-situ* measured in an Ar-filled glove box

under ambient pressure. The mass difference of UiO-66 before and after the soaking process was considered as the mass change caused by the absorbed FM. As shown in **Figure 4.9**, the mass of the UiO-66 powders increased by ~12% after soaking at ~500 psi, demonstrating the ability of UiO-66 to store of a large volume of liquefied FM molecules (corresponding to molar ratio of FM:UiO-66 at 5.7:1 for the absorbed sample), consistent with computational high FM loading value inside UiO-66.

4.4.2. Electrochemical properties of MOF-polymer membranes (MPM) in liquefied FM solution

Pure MOF membranes have been reported for gas adsorption/separation and solid electrolyte,[141-143, 157] however their poor mechanical properties and large thickness (typically >

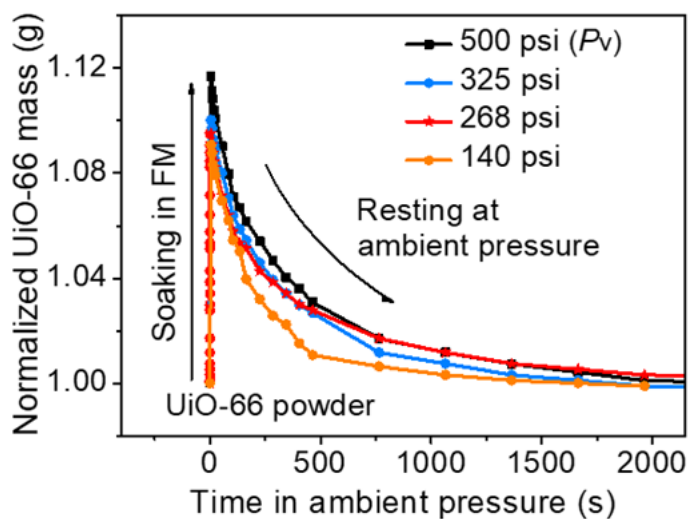


Figure 4.9 Mass change of liquefied FM soaked UiO-66.

100 μm) inhibit their applications in batteries. MOF particles have therefore been combined with commercial Celgard membranes or other porous substrates to improve the mechanical properties of the resulted MOF-based membranes.[158, 159] However, additional substrates increase the separator thickness and hinder the cathode – anode ion pathway at reduced pressures. Therefore, it is prerequisite to develop a mechanically robust, self-supporting MOF-based porous membrane with small thickness and minimal macro-voids for continuous ionic transport in LGE, especially at reduced pressures. Herein, in this work, a class of flexible MOF-polymer membranes (MPMs) were designed and applied to investigate battery performance.

To investigate the electrochemical properties of cells employing the MPM with FM, the ionic conductivity was measured by a customized two-electrode conductivity cell. As presented in **Figure 4.10a**, the LGE steadily maintained good conductivity from $-60\text{ }^{\circ}\text{C}$ to $30\text{ }^{\circ}\text{C}$. In contrast, the industry-standard liquid electrolyte (*e.g.*, 1 M LiPF_6 in ethylene carbonate (EC)/diethyl carbonate (DEC), 1:1 in volume, 1.2 M LiPF_6 in EC: ethyl methyl carbonate (EMC), 3:7 by weight) suffered from rapid conductivity fading with decreasing temperature, suggesting the advantage of using LGE in cold conditions. The MPM-confined FM exhibited an ionic conductivity of $\sim 0.14\text{ mS cm}^{-1}$ at $-60\text{ }^{\circ}\text{C}$ while the Celgard-based system showed less than 0.08 mS cm^{-1} at the same temperature and pressure (**Figure 4.10b**). This dramatic difference is attributed to the continuous microporous channels formed in the MOF layers and strong affinity between FM and MOFs, which provides improved transport properties.

To probe the nano-confinement effect of the MPM at low temperatures beneath the vapor pressure of the FM electrolyte, a special testing system was designed to control and record the

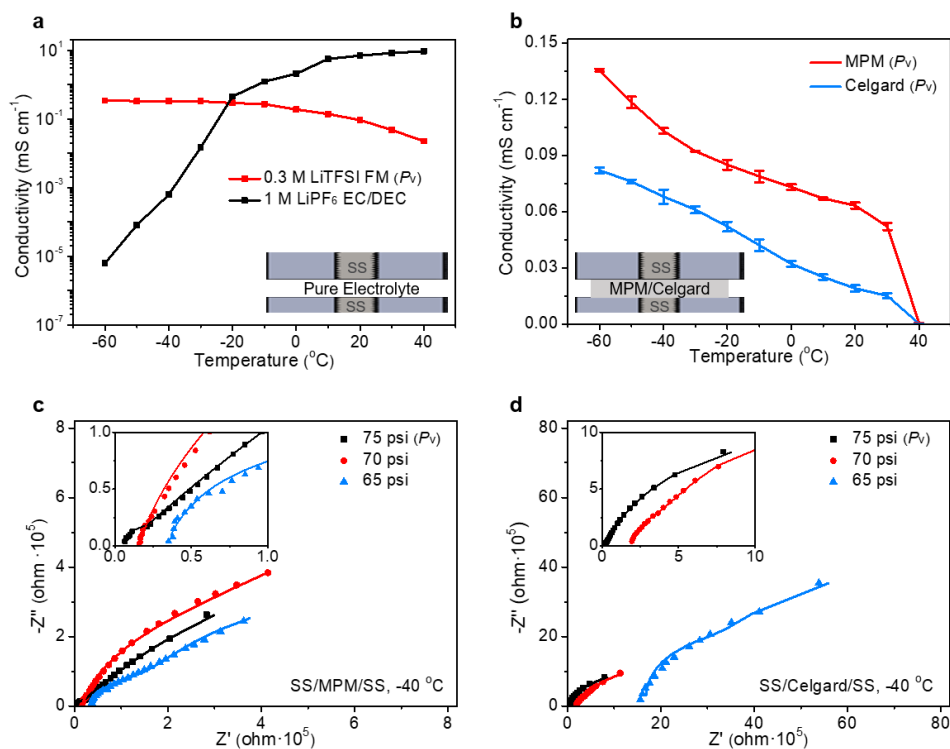


Figure 4.10 Electrochemical properties of MPM-based LGE. (a), Ionic conductivity of pure electrolyte with LGE or conventional liquid electrolytes. (b), Ionic conductivity of LGE with the presence of MPM or Celgard-based membranes as the separator at different temperatures. The two symmetric stainless steel (SS) cells shown in the inset a and b were set to remain the consistent 500-micron distance. Nyquist impedance of cells with MPM (c) or Celgard-based (d) membrane as the separator at -40 °C and different FM pressures.

pressure inside the tested cells, which was then applied to measure the ionic conductivity of the FM-soaked MPM at -40 °C under different pressures. By tuning the cell to 70 psi, 5 psi beneath the vapor pressure of the FM electrolyte, the cells utilizing MPM still offered an electrolyte conductivity of more than 0.02 mS cm⁻¹ at -40 °C (Figure 4.10c, Table 4.2), indicating that the MPM retained a reasonable amount of FM inside their pores beneath the bulk vapor pressure, enabling Li⁺ transport. On the contrary, the Celgard-based system produced an ionic conductivity of less than 0.002 mS cm⁻¹ due to inability of Celgard membranes to confine enough FM molecules at such pressure (Figure 4.10d, Table 4.2).

Table 4.2 Quantification of ionic conductivity value comparison between MPM and commercial Celgard membranes at different pressures at -40°C.

Pressure	MPM		Celgard	
	Bulk Resistance (Ohm)	Ionic Conductivity (mS/cm)	Bulk Resistance (Ohm)	Ionic Conductivity (mS/cm)
75 psi (P_v)	3173	0.113	5371	0.065
70 psi	15165	0.0217	192190	0.0015
65 psi	32908	0.009	1695000	0.0001

4.4.3. Cell performance with MPM confined FM electrolyte

To further verify the application of MPM in a real battery system, the MPM was applied to Li//CF_x primary cells, considering the excellent shelf life and negligible self-discharge behavior of CF_x in conventional liquid electrolytes. To ensure gas electrolyte transport, a composite cathode was fabricated by introducing 20 wt% of UiO-66 powders to blend CF_x with binder and conductive agent. The corresponding cells were assembled using CF_x composite cathode, Li metal as the anode, and the MPM or Celgard 2400 membranes as the separator (**Figure 4.11a**). The MPM-based cell produced an expected high capacity (~855 mAh g⁻¹) at room temperature and vapor pressure, considerably higher than cells with Celgard 2400 membranes (~810 mAh g⁻¹). At -40 °C and vapor pressure, the cells with MPM provided an around 71 % room temperature capacity retention (**Figure 4.11b**), which was slightly higher than that of the Celgard membranes.

More interesting results were found during cell operation at reduced pressure (below P_v). To ensure low-pressure gaseous phase operation, the cell pressure was *in-situ* monitored and maintained a nearly constant pressure of 70 psi during discharging operation (**Figure 4.11c**).

Notably, the cells with MPM can still maintain 57%, 46% and 25% of their room temperature capacity (at vapor pressure) at current density of 10, 20, and 40 mA g⁻¹, respectively (**Figure 4.11d**), in spite of the low conductivity of CF_x cathode and reduced charge-transfer kinetics at low temperature. In contrast, the cells with Celgard membrane under the same temperature and pressure produced negligible capacity (~ 0.03 mAh g⁻¹) at 10 mA g⁻¹. Moreover, during discharging the voltage sharply decreased due to a large internal resistance (**Figure 4.12**), suggesting that the large pores of Celgard membrane were not able to retain gas electrolytes at reduced pressure, in agreement with the ionic conductivity measurements.

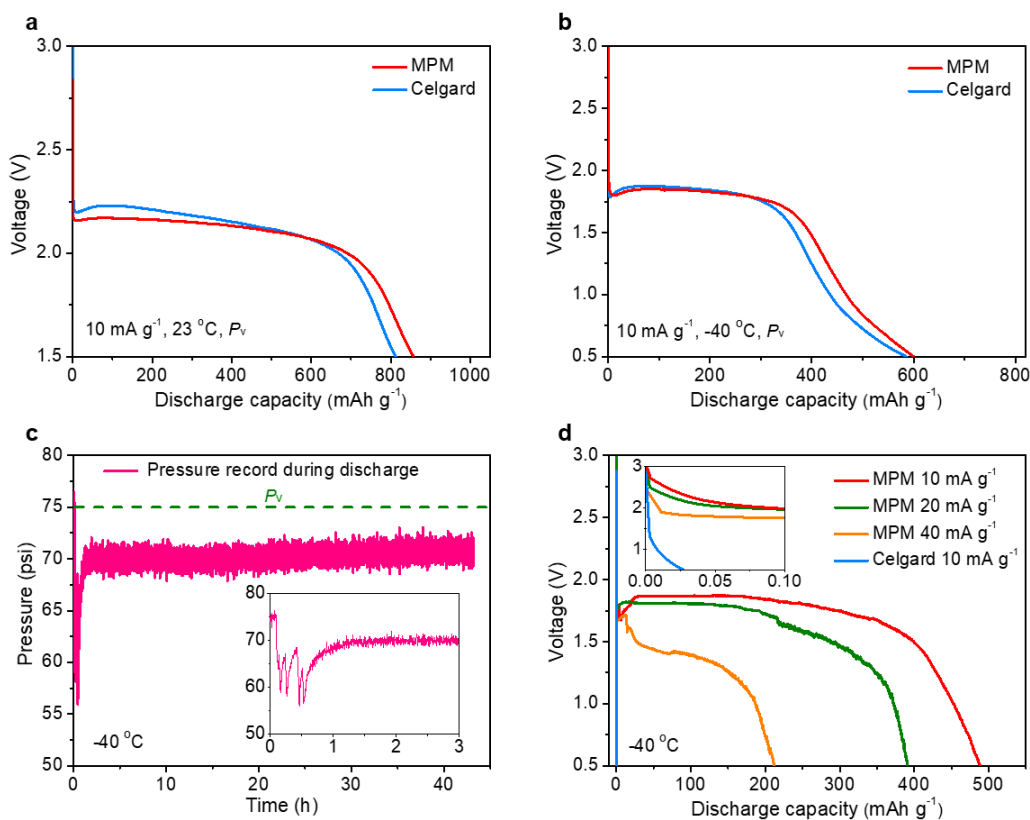


Figure 4.11 Cell performance of Li//CF_x cells. Discharge characteristics of Li//CF_x cells based on Celgard 2400 or MPM at room temperature (**a**) and -40 °C (**b**) under vapor pressure. (**c**), In-situ monitoring the interior pressure of Li//CF_x cell at -40 °C during the process of discharge. (**d**), Discharge characteristics of Li//CF_x cells based on Celgard 2400 or MPM at -40 °C, 70 psi and different discharge current density beneath vapor pressure.

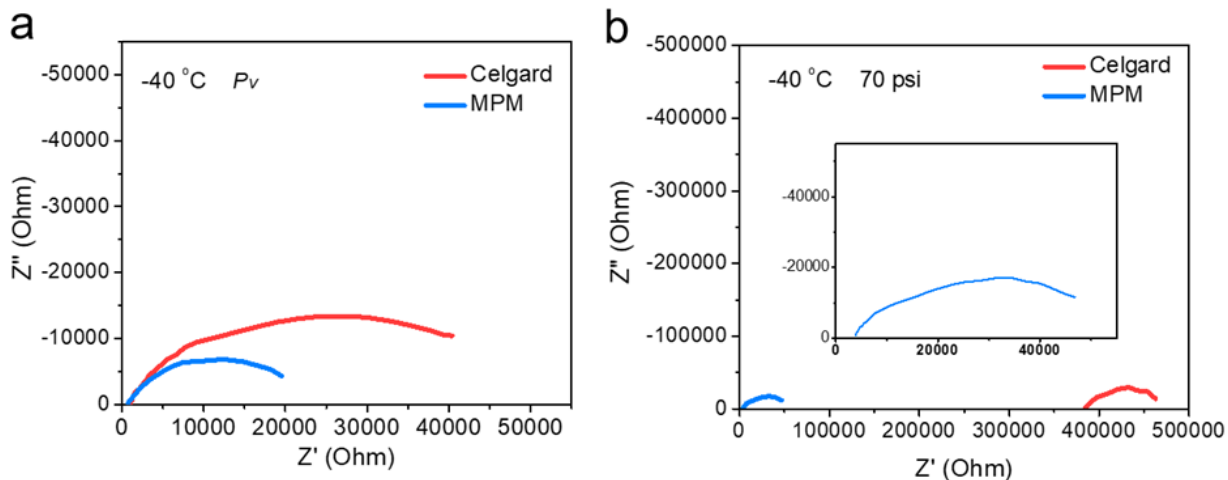


Figure 4.12 Nyquist impedance. Nyquist impedance of Li//CF_x cells mixed with 20 wt. % UiO-66 using Celgard and MPM at (a) vapor pressure and (b) 70 psi at -40 °C.

4.5. Conclusion

In summary, this work shows strong confinement effects of gas molecules in sub-nanometer pores which leads to significantly increased mass uptake of molecules at pressure lower than the vapor pressure of the bulk counterpart. Both computational and experimental results showed that the electrolyte system based on liquefied FM molecules via capillary condensation in MOFs lowers the equilibrium vapor pressure of FM. The resulted MPM with FM exhibited high structural integrity, decent ion conductivity, and high FM retention, which enabled the operation of high-energy Li cells at low temperatures and reduced working pressure. The unique properties endowed by molecule confinement in nanopores can be extended to design other types of ionic conductive structures for different electrochemical systems, thus opening up new opportunities for emerging applications without sacrificing ease of manufacturability and operation.

4.6. Acknowledgements

Chapter 4, in full, is a modified version of the published materials - Guorui Cai, Yijie Yin, Dawei Xia, Amanda A. Chen, John Holoubek, Jonathan Scharf, Yangyuchen Yang, Ki Hwan Koh1, Mingqian Li, Daniel M. Davies, Matthew Mayer, Tae Hee Han, Ying Shirley Meng, Tod A. Pascal, and Zheng Chen. “Sub-Nanometer Confinement Enables Facile Condensation of Gas Electrolyte for Low-Temperature Batteries” (2021), on Nature Communications. The dissertation author is the primary researcher who leads the computational analysis in this work.

CHAPTER 5 : Curvature-Selective Nanocrystal Surface Ligation Using Sterically-Encumbered Metal-Coordinating Ligands

Chapter 5 was reprinted (adapted) with permission from Y. Wang*, A.A. Chen*, K.P. Balto*, Y. Xie, J.S. Figueroa, T.A. Pascal, and A.R. Tao, “Curvature-Selective Nanocrystal Surface Ligation Using Sterically-Encumbered Metal-Coordinating Ligands”, *ACS Nano*, 16(8), 12747-12754. (2022). Copyright 2022 American Chemical Society. Changes were made for concentrating the theoretical backbone.

5.1. Abstract

Organic ligands are critical in determining the physicochemical properties of inorganic nanocrystals. However, precise nanocrystal surface modification is extremely difficult to achieve. Most research focuses on finding ligands that fully passivate the nanocrystal surface, with an emphasis on the supramolecular structure generated by the ligand shell. Inspired by molecular metal-coordination complexes, we devised an approach based on ligand anchoring groups that are flanked by encumbering organic substituents and are chemoselective for binding to nanocrystal corner, edge, and facet sites. Through experiment and theory, we affirmed that the surface-ligand sterics generated by these organic substituents are significant enough to impede binding to regions of low nanocurvature, such as nanocrystal facets, and to promote binding to regions of high curvature, such as nanocrystal edges.

5.2. Introduction

Inorganic nanocrystals are bound by crystalline facets that present highly undercoordinated surface sites at the corners and edges of the nanocrystal. Chemical modification of these surface sites can have a profound effect on the distinctive properties of a nanocrystal, including its optoelectronic function,[160] catalytic reactivity,[161] and ability to self-assemble.[162-164] Ligands that feature anchoring groups with favorable nanocrystal binding energies typically result in indiscriminate binding to all available surface sites, as exemplified by thiolated molecules where strong metal-sulfur bonds facilitate the formation of a molecular monolayer.[165] Nanocrystal surface ligation is further complicated by the consideration of solvent interactions, which can significantly alter both the thermodynamics and dynamics of surface-ligand interactions and, thus, interfere with binding site selectivity. As a result, very few strategies are successful in anchoring ligands with precision to specific nanocrystal features. [166]

In contrast, ligand-design strategies – often implemented through synthetic organic chemistry – are routinely employed to control the coordination number, geometry and overall electronic structure of molecular transition-metal complexes.[167-169] As a general principle, ligands featuring encumbering steric profiles can enforce and stabilize low coordination numbers for transition metal centers. A particularly effective scaffold used in the synthesis and stabilization of reactive, low-coordinate metal centers is the m-terphenyl ligand class,[170-174] in which two sterically-encumbering arene groups flank a metal-binding group on a central aryl ring. This specific molecular topology places considerable steric demands in the direction pointing toward the metal primary coordination sphere and, as a result, can promote low coordination numbers in molecular complexes through *ligand-ligand* steric interference (**Figure 5.1a**). We

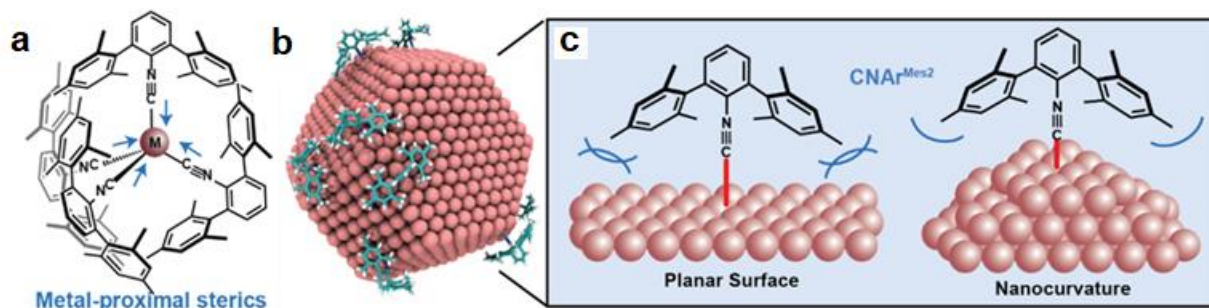


Figure 5.1 Nanocurvature selectivity enabled by surface-ligand sterics. Schematic of (a) a tetrahedral coordination complex formed by *m*-terphenyl isocyanide ligation to a metal center. (b) Computational model of *m*-terphenyl isocyanide ligands binding to an Au nanocrystal, where Au(100) and Au(111) surface facets generate planar, edge, and corner sites. (c) Schematic of *m*-terphenyl isocyanide selectivity for high-curvature surface binding sites due to the molecular topology of the ligand anchoring group.

reasoned that the *m*-terphenyl backbone, when attached to the surface of a nanocrystal, could serve to differentiate undercoordinated binding sites via *surface-ligand* steric interference. For surfaces with high nanocurvature such as nanocrystal corners and edges, binding should result in low steric interference from neighboring surface atoms in the vicinity of ligand anchoring. Surfaces with low nanocurvature, such as nanocrystal facets, more closely approximate a planar surface where the steric pressure from neighboring surface atoms becomes more significant and potentially great enough to inhibit ligand binding. (**Figure 5.1b, c**)

We specifically employ encumbering *m*-terphenyl isocyanide ligands,^[172-174] which provide a three-atom linker (ie. CNR) between a surface Au binding atom and the central aryl ring of the *m*-terphenyl backbone. This allows the organic substituents of the *m*-terphenyl isocyanide ligands to be synthetically tuned to either maximize or relieve steric pressures across a wide degree of nanocurvature. Nanocurvature-selective ligand binding is confirmed through nanocrystal extraction experiments and is explained by atomistic modelling, employing quantum mechanical (QM) electronic-structure calculations, and molecular dynamics (MD) simulations. We

conclusively demonstrate how the steric differentiation of ligand anchoring groups can be engineered, providing insights on nanocrystal ligand chemistries for improved nanocrystal synthesis and nanomanufacturing.

5.3. Theoretical and Computational Analysis

5.3.1. Investigation of CNAr^{Mes2} on Au

To pinpoint how the molecular topology of CNAr^{Mes2} leads to this curvature selectivity, we performed QM calculations employing density functional theory at the PBE/GGA level with dispersion corrections. A planar Au surface was modeled as either perfect Au(100) or Au(111) slabs, while a curved surface was modeled as an edge site at the intersection of the slabs. The binding energy was taken as the lowest energy for the CNAr^{Mes2} approach to each surface. We found that in vacuum, CNAr^{Mes2} exhibited a larger binding energy for edge sites ($E = -1.22$ eV) than for the Au(100) surface ($E = -0.17$ eV). (**Figure 5.2a, b**) Closer examination shows that the steric profile of the flanking arenes on CNAr^{Mes2} allows for a closer approach of the isocyanide group at the Au edge sites, with a C-Au distance of 2.0 Å. In contrast, steric interactions between these arenes and neighboring Au atoms on the Au(100) slab enforce a longer C-Au bond distance of 3.6 Å and thus weaker metal-ligand binding.

The presence of solvent modulates isocyanide ligand binding to the Au surface, as expected, an effect we quantify by means of extensive MD simulations. Here, we modeled a 5-nm diameter AuNS as a chamfered cube bound by Au(100) and Au(111) facets with edge lengths of 1.7 nm (**Figure 5.3**). Snapshots of the system solvated in CHCl₃ and structural analysis by means

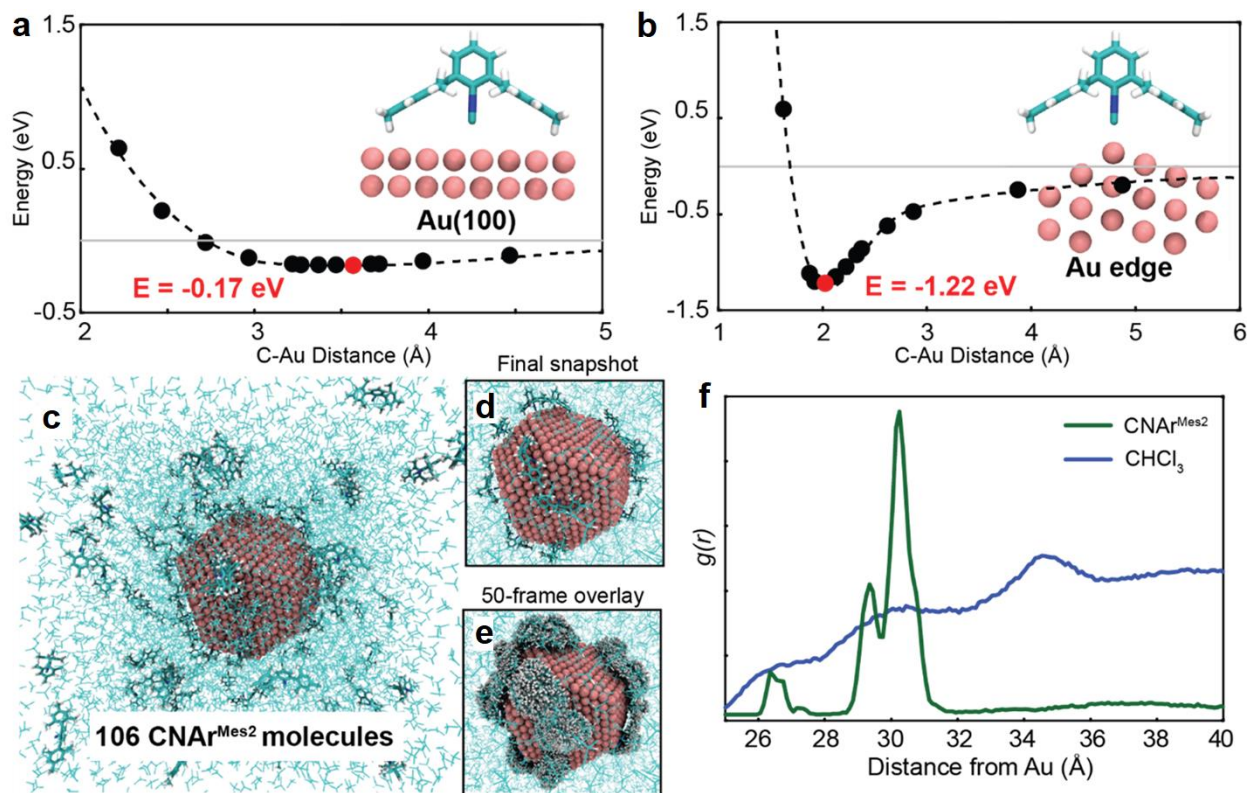


Figure 5.2 $\text{CNAr}^{\text{Mes}2}$ binding to Au nanocrystals. QM/DFT interaction energy plots of binding to (a) a flat Au(001) surface and (b) an Au edge site. The data (solid circles) are connected with a dashed line to guide the eye. The most favorable distance and energy are indicated in red. (Inset) atomistic model of the lowest energy configuration. (c) Final snapshot from the equilibrium MD simulation at 298K in CHCl_3 . (d) Zoom-in of the Au nanocrystal with bound $\text{CNAr}^{\text{Mes}2}$ and (e) an overlay of the last 50 frames of the MD trajectory, illustrating edge-specific binding and diffusion. (f) Radial distribution function of $\text{CNAr}^{\text{Mes}2}$ (green) and CHCl_3 (blue) taken with the AuNS center of mass as the origin. AuNS facets are located at 21-24 Å away and AuNS edges are located at 26-27 Å away. The peaks for $\text{CNAr}^{\text{Mes}2}$ at 29-30 Å correspond to adsorbed $\text{CNAr}^{\text{Mes}2}$ at edge sites, consistent with our DFT results. The peaks for $\text{CNAr}^{\text{Mes}2}$ at <28 Å correspond to diffusive motion of $\text{CNAr}^{\text{Mes}2}$ on the AuNS surface, which results in some $\text{CNAr}^{\text{Mes}2}$ mass crossing over to the flat surface, as seen in (e).

of radial distribution functions showed that $\text{CNAr}^{\text{Mes}2}$ selectively binds to the edges of the Au nanocrystal (Figure 5.2c-f). Our simulations also reveal that while the binding of $\text{CNAr}^{\text{Mes}2}$ to the solvated nanocrystal is strong (with no observed $\text{CNAr}^{\text{Mes}2}$ desorption), the molecules selectively

diffuse along the edge sites. (**Figure 5.2e**) Along with accelerated MD simulations (**Figure 5.4**), as detailed in Section 5.3.3.6., these computational results are consistent with a predicted 150-fold increased $\text{CNAr}^{\text{Mes}_2}$ binding to the edge sites.

Microscopic insights into the ligand exchange process were also quantified, using accelerated MD simulations of $\text{CNAr}^{\text{Mes}_2}$ bound to AuNSs in water. These simulations revealed that $\text{CNAr}^{\text{Mes}_2}$ binding free energies in water are reduced on the edge sites, in sharp contrast to the energetics in chloroform. We also calculated an unfavorable free energy of $\text{CNAr}^{\text{Mes}_2}$ transfer from chloroform to water based on the solvation free energies of the solvated ligand ($A_{\text{CNAr}^{\text{Mes}_2}|\text{CHCl}_3}$: -1.01eV and $A_{\text{CNAr}^{\text{Mes}_2}|\text{water}}$: -0.37eV). As the results, in a water | chloroform mixture solution, $\text{CNAr}^{\text{Mes}_2}$ favors transfer from aqueous phase into chloroform phase (**Figure 5.5**). Thus, the solvent-philic forces between $\text{CNAr}^{\text{Mes}_2}$ and chloroform are the major thermodynamic driving force for the complete transfer of $\text{CNAr}^{\text{Mes}_2}$ -bound AuNSs into the chloroform phase and our calculations support our hypothesis that it is unlikely that that any $\text{CNAr}^{\text{Mes}_2}$ -bound AuNSs remain in the aqueous phase.

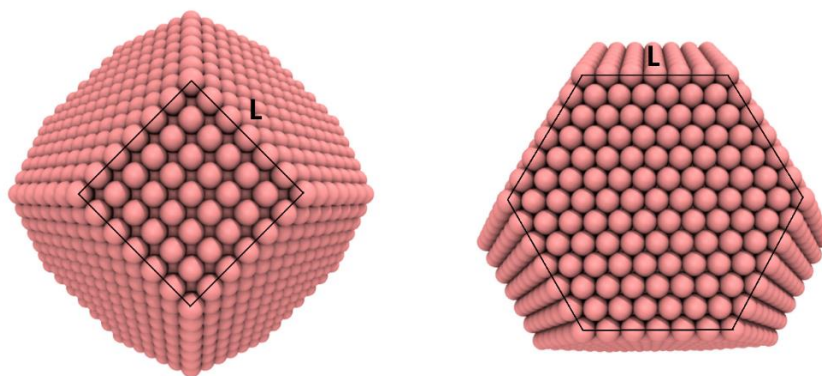


Figure 5.3 Initial AuNS structure used in MD simulations. The diameter is ~5 nm and edge length, L, is ~1.7 nm. The distances from the AuNS center of mass to the Au(001) surfaces, the Au(111) surfaces, the Au(001/111) edges, the Au(111/111) edges, and the corners of Au(001/111/111) facets, are 24.5 Å, 21.5 Å, 26 Å, 26 Å, 27 Å, respectively.

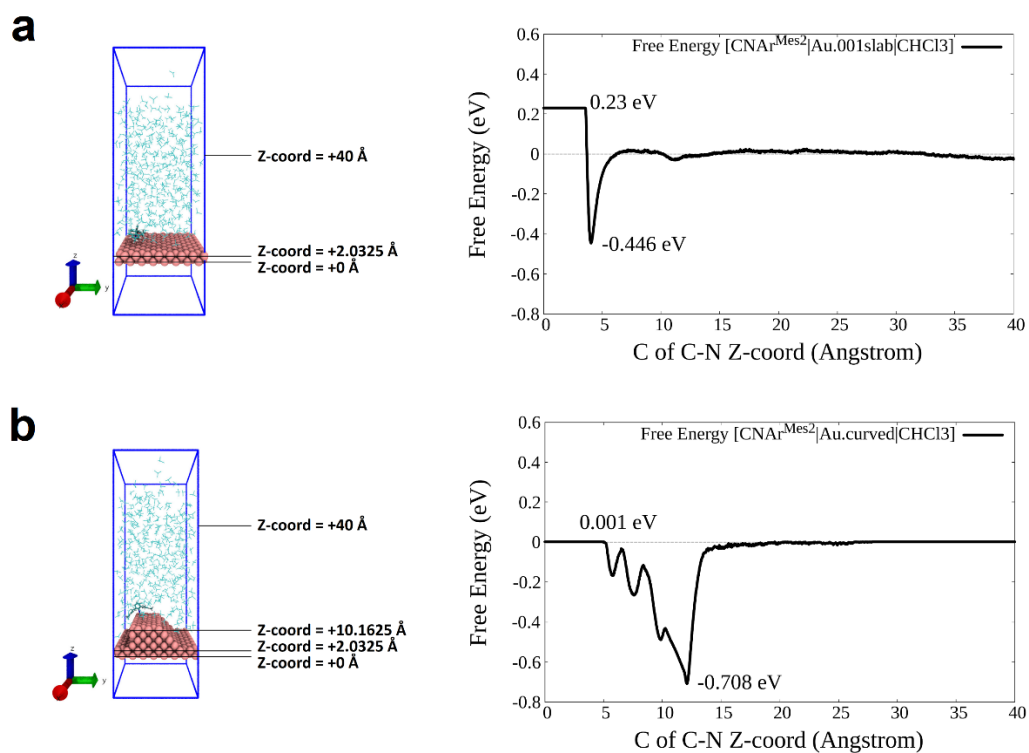


Figure 5.4 Free energy of binding of $\text{CNAr}^{\text{Mes}_2}$ to (a) Au(001) slab and (b) Au(curved) slab. All calculations employed Metadynamics accelerated sampling in CHCl_3 at 298K. The distance, Z , was computed between the carbon of $\text{CNAr}^{\text{Mes}_2}$ $\text{C}\equiv\text{N}$ group and the bottom of the Au-slab (Z coordinate = 0 Å).

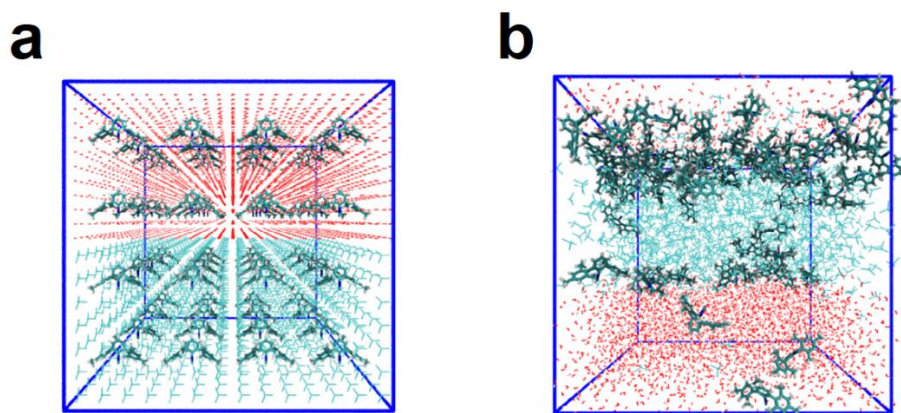


Figure 5.5 (a) Initial snapshot of 64 $\text{CNAr}^{\text{Mes}_2}$ molecules randomly distributed in a box containing 4484 water molecules (red) and 1096 CHCl_3 molecules (blue). (b) Final snapshot after equilibrium MD simulation at 298K and 1atm, showing $\text{CNAr}^{\text{Mes}_2}$ ligands transferring to the organic CHCl_3 phase.

5.3.2. Investigation of CNXyl, CNAr^{Dipp2}, and CNAr^{Tripp2} on Au

We computationally screened two additional *m*-terphenyl isocyanide ligands that were expected to exhibit increased ligand-surface steric pressures: CNAr^{Dipp2} (Ar^{Dipp2} = 2,6-(2,6-(*i*-Pr)₂C₆H₃)₂C₆H₃); *i*-Pr = *iso*-propyl)[173] and CNAr^{Tripp2} (Ar^{Tripp2} = 2,6-(2,4,6-(*i*-Pr)₃C₆H₂)₂C₆H₃)). [174] The results for CNXyl, for which we experimentally observed uninhibited AuNS binding across all AuNS sizes, are also shown for comparison. The calculated QM interaction energies indicate that both CNAr^{Dipp2} and CNAr^{Tripp2} ligands exhibit weaker Au edge-site binding than CNAr^{Mes2}, with binding energies of -0.89 eV and -0.58 eV, respectively (**Figure 5.6a-c**). CNAr^{Dipp2}, which lacks a substituent in the *para*-position of the flanking arene ring, exhibited stronger binding to facet sites than CNAr^{Mes2}, with E = -0.29 eV. The more encumbering and functionalized arene groups in CNAr^{Dipp2} and CNAr^{Tripp2} also increased the oleophilicity of the ligands.

To better correlate these calculated free energies (**Table 5.1**) with experimental ligand exchange and LLE outcomes, as detailed in Section 5.4., we considered four computational descriptors for optimizing nanocurvature selectivity binding and solvent extraction of AuNSs using various ligand anchoring chemistries (**Table 5.2**). First is the site-binding ratio (*SBR*) calculated as the difference between the DFT interaction energies at the edge sites and a flat surface. This term describes a ligand's ability to selectively bind to high-curvature surface sites. Second is the nanocrystal edge-binding factor (*EBF*), calculated as the difference between the DFT interaction energy, corrected for zero-point energy and differential entropy of binding effects, at an edge site and the ligand solvation energy. This term accounts explicitly for solvent entropic effects. Third is the solubility factor (*SF*), calculated as the difference between the solvation free

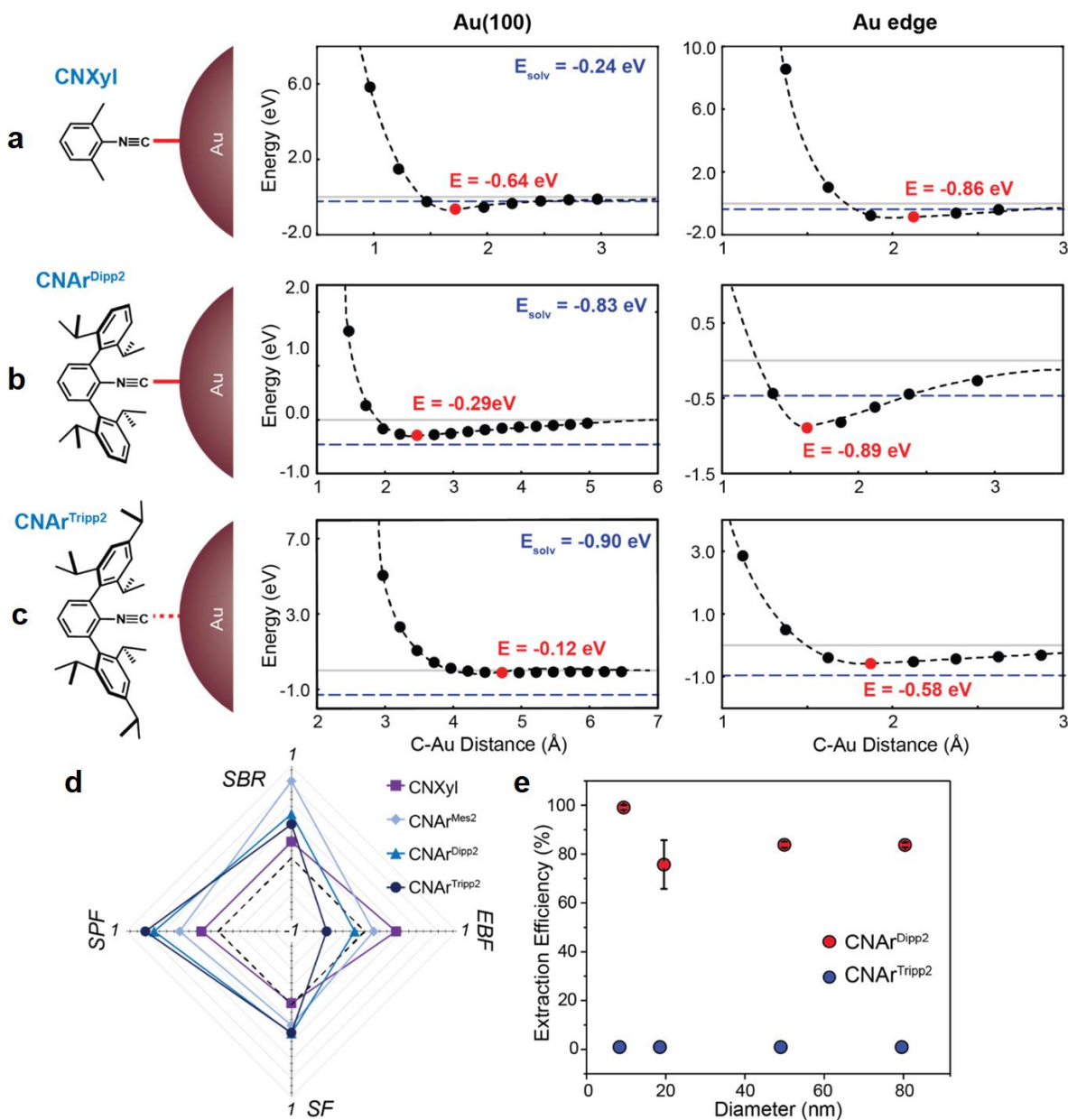


Figure 5.6 Surface-ligand steric pressure by design. Schematics of AuNS binding and QM/DFT interaction energy plots of binding for (a) CNXyl, (b) CNAr^{Dipp2} and (c) CNAr^{Tripp2}, which possess organic substituents with varying degrees of bulkiness. For interaction energy plots, the data (solid circles) are connected with a dashed line to guide the eye. The most favorable distance and energy indicated in red, and solvation energies are indicated by the dashed blue line. (d) Spider plot showing site-binding ratio (SBR), edge-binding factor (EBF), solubility factor (SF), and solvent partition factor (SPF) values for CNAr^{Mes2} and the ligands in (a-c). Normalized values range from -1 to 1, with the black dashed line indicating a value of 0. (e) Experimental extraction efficiencies for CNAr^{Dipp2} and CNAr^{Tripp2} for AuNS with varying diameters. Error bars for CNAr^{Tripp2} are not shown because they are smaller than the size of the data point.

Table 5.1 Solvation free energies difference of various Isocyanide ligands in CHCl₃ and water, and cohesive free energy (self-solvation energy) from Free Energy Perturbation calculations.

Ligand	$A_{\text{ligand CHCl}_3}$ (eV)	$A_{\text{ligand water}}$ (eV)	A_{cohesive} (eV)
CNXyl	-0.24	-0.01	0.06
CNA _r ^{Dipp2}	-0.83	0.04	-0.44
CNA _r ^{Mes2}	-1.01	-0.37	-0.62
CNA _r ^{Tripp2}	-0.90	0.09	-0.52

Table 5.2 Values of computational descriptors for various isocyanide ligands.

Ligand	SBR	EBF	SF	SPF
CNXyl	0.22	0.43	-0.02	0.23
CNA _r ^{Dipp2}	0.60	-0.14	0.40	0.87
CNA _r ^{Mes2}	1.00	0.12	0.28	0.52
CNA _r ^{Tripp2}	0.46	-0.52	0.38	1.00

energy in chloroform and the partition factor (*SPF*) calculated as the difference in solvation energy of the free ligand in chloroform and cohesive free energy of the corresponding amorphous solid. This term is a thermodynamic factor related to the average concentration of the ligands located near the nanocrystal. The final descriptor is the solvent water. This last term is related to the efficiency of the LLE process. **Figure 5.6d** plots these parameters for the *m*-terphenyl isocyanide ligands studied here, where we adopted the convention of normalized functions ranging from -1 (unfavorable) to 1 (favorable), with 0 representing the threshold.

For $\text{CNAr}^{\text{Dipp}2}$, we calculated a reduced site-binding ratio of $SBR \approx 0.6$ (compared to 1.0 for $\text{CNAr}^{\text{Mes}2}$) and an unfavorable EBF of -0.1 (compared to 0.1 for $\text{CNAr}^{\text{Mes}2}$), that would preclude binding to smaller AuNSs dominated by edge and corner sites. On the other hand, the higher SPF is predicted to increase the affinity of $\text{CNAr}^{\text{Dipp}2}$ for chloroform. LLE experiments using $\text{CNAr}^{\text{Dipp}2}$ were consistent with our predictions, exhibiting relatively high extraction efficiencies (**Figure 5.6e**) that were particularly pronounced for larger AuNSs. In fact, we found that in this larger size regime, $\text{CNAr}^{\text{Dipp}2}$ outperformed $\text{CNAr}^{\text{Mes}2}$ in facilitating AuNS LLE. The effects of steric encumbrance were even more pronounced with $\text{CNAr}^{\text{Tripp}2}$, where the large, negative edge-binding factor ($EBF = -0.5$) predicted unfavorable binding to nanocrystal surface sites (even regions of high curvature). Indeed, we measured extraction efficiencies of $<10\%$, even for the smallest 10 nm AuNSs and Raman measurements indicated limited-to-no binding. Across the four isocyanide ligands studied in our experiments, tuning the steric profiles of the flanking arenes of the *m*-terphenyl group provides only moderate differentiation of ligation via SPF and SF , with all ligands providing sufficient solubility for nanocrystal post-processing.

5.3.3. Computational Details

Both Quantum Mechanics (QM) calculations and Molecular Dynamics (MD) simulations were used to study the binding thermodynamics and kinetics of the various ligands to the Au nanosphere surfaces. QM calculations were performed using the Q-Chem 5.2,[2] and Quantum Espresso (QE) [3, 4] electronic structure packages to determine the optimized ligand structure and the ligand-gold interaction energies, respectively. The MD simulations were performed with

LAMMPS [1] simulation engine. In MD, the Au nanoparticles were described using EAM/Fs potential of Ackland et. al. [175]. Ligands were described using either the GAFF [176] or OPLS/AA [177] forcefields, except for the critical C≡N bond stretching and the aromatic rings torsions, which were determined from QM to reproduce the CNXyl and CNAr^{Mes2} intra-molecular motion. The CHCl₃ solvent was modelled using the Kamath et al. forcefield [178], while the SPC/E potential was used for water [34].

5.3.3.1. Parameterization of the ligand C≡N/AuNS Interactions

Au-ligand(s) interaction was optimized by developing a forcefield based on fitting the binding energy curves obtained from QM calculations, detailed in **Table 5.3**. The ligand(s) structure was first at the 6-31G/MP2 level using DFT using Q-Chem. Various Au slabs were constructed from the fcc crystal structures and the binding energy of the rigid ligand in QE was calculated with ultrasoft pseudopotentials [179], a kinetic energy cutoff of 30 Ry, and a (5,5,1) K-point grid. In each case, a ligand was initially placed far from the Au slab and gradually moved onto the Au slab. The energy vs distance curve for the various ligand(s)|Au configurations were obtained. The associated binding energy curve was further fitted to Lennard-Jones 12-6 / Morse potentials in determining the ligand(s) atoms | Au atoms interaction parameters, using a nonlinear regression approach.

Table 5.3 The CNXyl, CNAr^{Dipp2}, CNAr^{Tripp2}, and CNAr^{Mes2} - gold interaction energies via QM calculations.

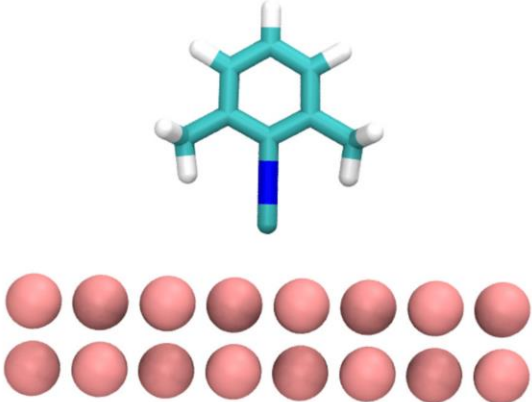
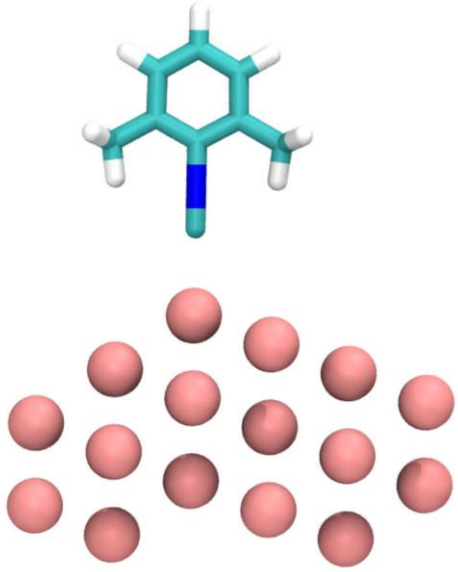
CNXyl			
CNXyl on Au(001)		CNXyl on Au-edge site	
			
<u>C-Au Distance (Å)</u>	<u>QM (eV)</u>	<u>C-Au Distance (Å)</u>	<u>QM (eV)</u>
0.9675	5.83818	1.3726	8.55542
1.2175	1.48167	1.6226	1.01988
1.4675	-0.24781	1.8726	-0.77072
1.7175	-0.63530	2.1226	-0.85800
1.9675	-0.53263	2.3726	-0.61226
2.2175	-0.34628	2.6226	-0.40139
2.4675	-0.21614		
2.7175	-0.14591		
2.9675	-0.10773		

Table 5.3 The CNXyl, CNAr^{Dipp2}, CNAr^{Tripp2}, and CNAr^{Mes2} - gold interaction energies via QM calculations. (Continued)

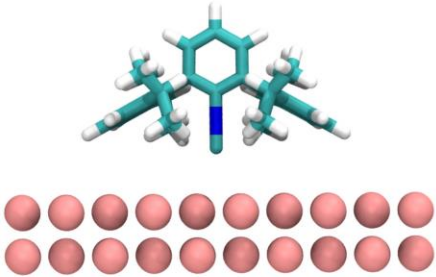
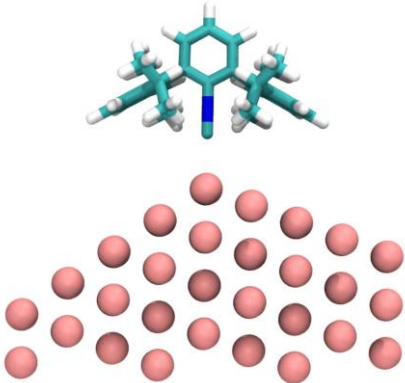
CNAr ^{Dipp2}			
CNAr ^{Dipp2} on Au(001)		CNAr ^{Dipp2} on Au-edge site	
			
C-Au Distance (Å)	QM (eV)	C-Au Distance (Å)	QM (eV)
1.4675	1.64788	1.372601	-0.43597
1.7175	0.26573	1.622601	-0.89239
1.9675	-0.16599	1.872601	-0.82114
2.2175	-0.26878	2.122601	-0.61563
2.4675	-0.28790	2.372601	-0.44592
2.7175	-0.27858	2.872601	-0.26696
2.9675	-0.25340		
3.2175	-0.21845		
3.4675	-0.18370		
3.7175	-0.15629		
3.9675	-0.13564		
4.2175	-0.11965		
4.4675	-0.10310		
4.7175	-0.08488		
4.9675	-0.06193		

Table 5.3 The CNXyl, CNAr^{Dipp2}, CNAr^{Tripp2}, and CNAr^{Mes2} - gold interaction energies via QM calculations. (Continued)

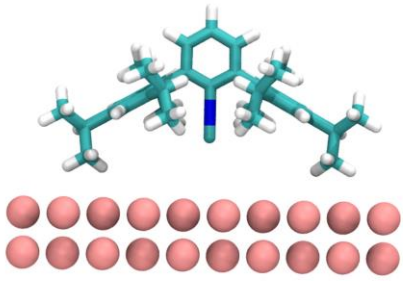
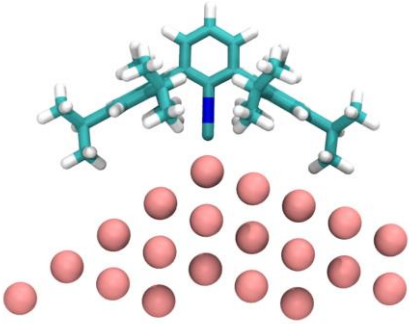
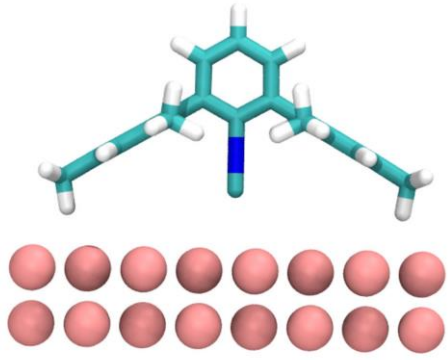
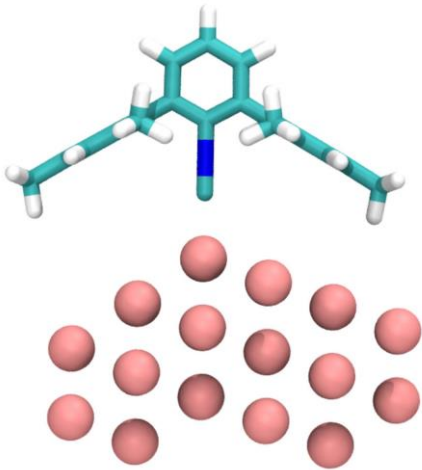
CNAr ^{Tripp2}			
CNAr ^{Tripp2} on Au(001)		CNAr ^{Tripp2} on Au-edge site	
			
C-Au Distance (Å)	QM (eV)	C-Au Distance (Å)	QM (eV)
2.9675	5.04476	1.122601	2.84628
3.2175	2.31487	1.372601	0.49711
3.4675	1.0565	1.622601	-0.39581
3.7175	0.42969	1.872601	-0.58182
3.9675	0.11674	2.122601	-0.52317
4.2175	-0.03641	2.372601	-0.43464
4.4675	-0.10215	2.622601	-0.36343
4.7175	-0.11909	2.872601	-0.30916
4.9675	-0.11157		
5.2175	-0.0942		
5.4675	-0.07795		
5.7175	-0.06892		
5.9675	-0.06608		
6.2175	-0.06437		
6.4675	-0.06028		

Table 5.3 The CNXyl, CNAr^{Dipp}₂, CNAr^{Tripp}₂, and CNAr^{Mes}₂ - gold interaction energies via QM calculations. (Continued)

CNAr ^{Mes} ₂			
CNAr ^{Mes} ₂ on Au(001)		CNAr ^{Mes} ₂ on Au-edge site	
			
C-Au Distance (Å)	QM (eV)	C-Au Distance (Å)	QM (eV)
2.2175	0.64502	1.6226	0.59733
2.4675	0.20792	1.8726	-1.11521
2.7175	-0.01283	1.9226	-1.19700
2.9675	-0.11798	2.0226	-1.21695
3.2175	-0.15908	2.1226	-1.14940
3.2675	-0.16807	2.2226	-1.04553
3.3675	-0.16624	2.3226	-0.92301
3.4675	-0.16727	2.3726	-0.85965
3.5675	-0.16899	2.6226	-0.62050
3.6675	-0.16151	2.8726	-0.47079
3.7175	-0.15908	3.8726	-0.24495
3.9675	-0.14169	4.8726	-0.19437
4.4675	-0.10072		

5.3.3.2. Description of Systems in MD Simulations

A Chamfered cube AuNS with 4033 atoms was constructed containing equal edge lengths of 12 hexagons and 6 squares faces. (**Figure 5.3**) The system was solvated by inserting the AuNS into a $100 \times 100 \times 100 \text{ \AA}^3$ box of CHCl_3 molecules and removing the solvent molecules within 2 \AA of the AuNS. Afterwards, ligands were then distributed randomly in the simulation box and overlapping solvent molecules were removed as necessary. The vacuum systems (**Figure 5.1b** and **Figure 5.7**), which were conducted to demonstrate the selective adsorption, did not contain CHCl_3 solvent and the simulation box was set as $100 \times 100 \times 100 \text{ \AA}^3$. The composition of the various systems is detailed in **Table 5.4**.

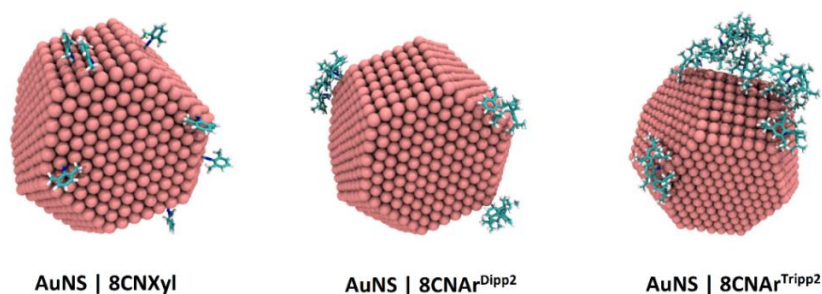


Figure 5.7 Final snapshot from equilibrium MD simulations in vacuum at 298K of (left to right) CNXyl , $\text{CNAr}^{\text{Dipp}2}$, $\text{CNAr}^{\text{Tripp}2}$ on a 5nm AuNS.

Table 5.4 Composition of simulation cells used in various MD simulations. The associated figures are indicated.

System	Ligand(s)	# of Ligands	# of AuNSs	# CHCl_3
$\text{CNAr}^{\text{Mes}2}$ on AuNS (Figure 5.1b)	$\text{CNAr}^{\text{Mes}2}$	8	1	0 (Vacuum)
$\text{CNAr}^{\text{Mes}2}$ -AuNS in CHCl_3 (Figure 5.2)	$\text{CNAr}^{\text{Mes}2}$	106	1	7337
Isocyanides on AuNS (Figure 5.7)	CNXyl , $\text{CNAr}^{\text{Dipp}2}$, $\text{CNAr}^{\text{Tripp}2}$	8	1	0 (Vacuum)

5.3.3.3. Equilibrium MD Simulations and Vibrational Spectral Analysis

The van der Waals and real space coulomb cutoffs in the MD simulations were 10Å. A cubic spline was applied to the van der Waals to ensure smooth convergence and vanishing energies and forces at the cutoff (inner cutoff distance of 9Å). The reciprocal space coulomb interactions were computed with a particle-particle-particle-mesh solver, with an error tolerance of 10^{-6} [180]. Each MD simulation was initiated with 500 conjugated gradient steps, followed by gradual heating to 298K using 0.5 ns (500,000 steps with an integration timestep of 1 fs) dynamics in the canonical ensemble (NVT – constant number of particles N, volume V and temperature T) at 298K. A Nose-Hoover thermostat was used with a temperature relaxation window of 100 fs. Afterwards, the system was equilibrated at the correct density by performing dynamics in the isobaric isothermal (NPT: constant N, pressure P and temperature T) ensemble. The Shinoda et al. [152] equations of motion, which incorporates the Martyna et al [153] hydrostatic equations and the strain energy formulism of Parrinello and Rahman [154] were adopted. The time-reversible measure-preserving Verlet integrators derived by Tuckerman et al. [155] was applied for the time integration. After density equilibration, the system was simulated in the NVT ensemble for at least 5ns of NVT dynamics. Starting with snapshots of each system every 1 ns, additional 40 ps NVT simulation were run, and the velocities and coordinates were saved every 4 fs (10,000 frames in the corresponding trajectory). The vibrational density of states function was calculated, based on Fourier transform of the velocity autocorrelation functions, to analyze the ligand C≡N spectra (**Figure 5.8**) [109, 181], which performed the same trend (blueshift) as the experimental SERS and FTIR spectrums (**Table 5.5**).

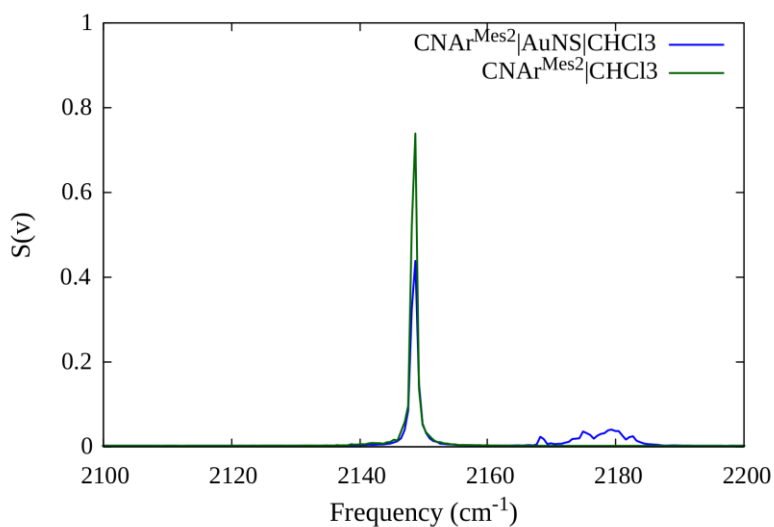


Figure 5.8 Simulated C≡N vibrational spectrum of CNAr^{Mes2} as a free molecule in CHCl₃ (green) and as a bound-molecule to the AuNSs surface (blue). A blueshift of ~ 30 cm⁻¹ is observed upon binding, in good agreement with both experimental FTIR and surface-enhanced Raman spectroscopic (SERS) data.

Table 5.5 Simulated and experimental isocyanide stretching frequencies, $\nu(\text{CN})$, of Au-bound and free CNAr^{Mes2}.

Simulated $\nu(\text{CN})$ in CHCl ₃		Experimental $\nu(\text{CN})$	
Free CNAr ^{Mes2}	Adsorbed CNAr ^{Mes2}	Free CNAr ^{Mes2}	Adsorbed CNAr ^{Mes2}
2149 cm ⁻¹	2170-2185 cm ⁻¹	2119 cm ⁻¹ (FTIR)	2166.5 cm ⁻¹ (SERS)

5.3.3.4. Radial Distribution Function Analysis

The radial distribution function, $g(r)$, was used to calculate the ligand densities at various distance from the AuNS center of mass. The $g(r)$ can be expressed as:

$$g(r) = \frac{d\langle N_{ij}(r) \rangle}{\rho_{ij} dV(r)}, \quad (5.1)$$

where $dV(r)$ is the volume of the shell being considered $d\langle N_{ij}(r) \rangle$ is the average number of either atom in $dV(r)$ within a distance dr of the other atom and ρ_{ij} is the atomic bulk density factor. In this analysis, the AuNS and each ligand molecule were taken as individual super atoms defined by the respective centers of mass and the closest contact point for each ligand is defined by the radius of the AuNS, $\sim 25 \text{ \AA}$.

5.3.3.5. Ligand Solvation Free Energy Calculations

Free Energy Perturbation (FEP), based on the advancements of Zwanzig [182], is a statistical approach to compute the free energy difference between two states:

$$\begin{aligned} \Delta A (\text{from state1 to state2}) &= A(\text{state2}) - A(\text{state1}) \\ &= -k_B T \ln \left\langle \exp \left(-\frac{U(\text{state2}) - U(\text{state1})}{k_B T} \right) \right\rangle, \quad (5.2) \end{aligned}$$

where A denotes free energy, k_B is the Boltzmann constant, and U is energy.

The solvation energies of the various isocyanide ligands were calculated as the sum of multi-stages free energy changes. Here, a coupling parameter λ ($0 \leq \lambda \leq 1$) is introduced to

gradually change the ligand – solvent interaction energy, such that the free energy [183] is obtained as:

$$\Delta_0^1 A = \sum_{i=0}^{n-1} \Delta_{\lambda_i}^{\lambda_{i+1}} A = -kT \sum_{i=0}^{n-1} \ln \left\langle \exp \left(-\frac{U(\lambda_{i+1}) - U(\lambda_i)}{kT} \right) \right\rangle_{\lambda_i}, \quad (5.3)$$

In this study, $\lambda = 0.01$ was used and the interaction energies were modified in 100 stages (windows) over 100 ps NPT per window. These results are presented in **Table 5.1**.

5.3.3.6. Free Energy of Isocyanide Binding to Solvated AuNSs

Using accelerated MD simulations, the free energy kinetics of isocyanide ligand binding to AuNS was computed. Metadynamics [184] was employed to enhance the sampling and explore regions of the potential energy surfaces characterized by deep local minima. Two types of systems were considered: 1) a Au (100) slab, representative of the larger NPs with large radius of curvatures and 2) an edge site comprising a Au(110) motif on the Au (100) slab, representative of smaller NPs with small radius of curvatures (**Figure 5.4**). Each system was first solvated and equilibrated according to the procedure above. Afterwards, Metadynamics simulations, where the carbon of the isocyanide group ($C \equiv NR$) to the Au surface was chosen as the collective variable (colvar), were performed. Each simulation was biased by depositing Gaussian functions every 0.2 ps with a height of 0.02 kcal/mol and a width of 1.25 Å. The system was evolved for a minimum of 200 ns. Convergence was checked by monitoring colvar distance until it showed ballistic behavior.

5.3.3.7. Computation of Normalized Descriptors

To straightforwardly compare the binding and solvation energies, DFT interaction energies were corrected for zero-point energy (ZPE) and entropy of binding (TΔS) effects:

$$\Delta G_{DFT-bind} = \Delta E_{DFT-bind} + \Delta ZPE + T\Delta S , \quad (5.4)$$

where the ΔZPE is obtained from vibrational frequency calculations of the isolated and bound isocyanides, and TΔS is taken as difference between the free (ideal gas) and bound isocyanides. Generally, it was found that these corrections account for ~ +0.2 eV for the various structures.

For the various descriptors (X), relative energies (ΔY) were calculated and divided by the norm of the largest value if it exceeds 1:

$$X = \frac{\Delta Y}{\max |\Delta Y|} , \quad (5.5)$$

The various descriptors thus range from -1 (unfavorable) – +1 (favorable), with a favorable/unfavorable threshold taken as 0:

$$\begin{aligned} SBR &= \Delta G_{DFT-bind}^{flat} - \Delta G_{DFT-bind}^{edge} \\ EBF &= \Delta G_{DFT-bind}^{edge} - \Delta G_{solvation}^{CHCl_3} \\ SF &= \Delta G_{cohesive} - \Delta G_{solvation}^{CHCl_3} , \\ SPF &= \Delta G_{solvation}^{H_2O} - \Delta G_{solvation}^{CHCl_3} \end{aligned} \quad (5.6)$$

where *SBR* is site binding ratio, *EBF* is edge-binding factor, *SF* is solubility factor and *SPF* is solvent partition factor.

5.4. Experimental Analysis

In addition to the theoretical concepts, experimental investigations were conducted to confirm the hypothesis on the ligand selectivity characteristics over nanocurvatures, where the experiments were completed by our collaborated groups of Prof. Andrea Tao and Prof. Joshua Figueroa. Details were mentioned in our published paper on the year of 2022 [185]. Here, an overview of the experimental analysis was provided.

5.4.1. Investigation of selective binding by *m*-terphenyl-based anchoring groups

Ligand exchange reactions using pseudospherical Au nanocrystals (AuNSs) and the *m*-terphenyl isocyanide ligand $\text{CNAr}^{\text{Mes}_2}$ ($\text{Ar}^{\text{Mes}_2} = 2,6\text{-}(2,4,6\text{-Me}_3\text{C}_6\text{H}_2)_2\text{C}_6\text{H}_3$) [172, 174] indicate that ligand binding is selective for nanocurvature and is consistent with ligand-surface steric interference as the dominant mechanism for selectivity. We first carried out ligand exchange of 10 nm citrate-stabilized AuNSs using the $\text{CNAr}^{\text{Mes}_2}$ ligand to facilitate nanocrystal transfer from an aqueous phase to chloroform. Importantly, unencumbered alkyl and aryl isocyanides have been well established to bind to Au surfaces and nanoparticles, [186-192] and can exhibit surface binding energies competitive with thiols. [189, 192] Successful $\text{CNAr}^{\text{Mes}_2}$ complexation to the AuNSs was accompanied by a corresponding color change of the aqueous phase (raffinate) from red to colorless. Upon transfer into chloroform, the $\text{CNAr}^{\text{Mes}_2}$ -bound AuNSs aggregated to form a grey precipitate that was readily extracted via solvent evaporation or centrifugation. Binding of $\text{CNAr}^{\text{Mes}_2}$ could be characterized by surface-enhanced Raman spectroscopy (SERS) (**Figure 5.9a**), showing complete displacement of citrate by $\text{CNAr}^{\text{Mes}_2}$ and a sharp peak at 2166 cm^{-1} corresponding to the $\nu(\text{CN})$ stretching vibrations of Au-bound isocyanide. [172, 173, 186, 187, 190, 193, 194] Complete transfer of the AuNSs into chloroform was confirmed by extinction

measurements (**Figure 5.9b**) of the raffinate, where the optical density (*OD*) goes to near-zero after ligand exchange.

The metal-proximal steric properties of $\text{CNAr}^{\text{Mes}_2}$ are expected to result in less favorable binding energies for larger AuNSs, for which surface curvature is lower and steric interactions begin to dominate surface-ligand interactions. Because AuNSs possess pseudospherical morphologies with irregular faceting, the surface selectivity of $\text{CNAr}^{\text{Mes}_2}$ is expected to depend not only on AuNS size, but the relative number of edge and corner sites to facet sites available for

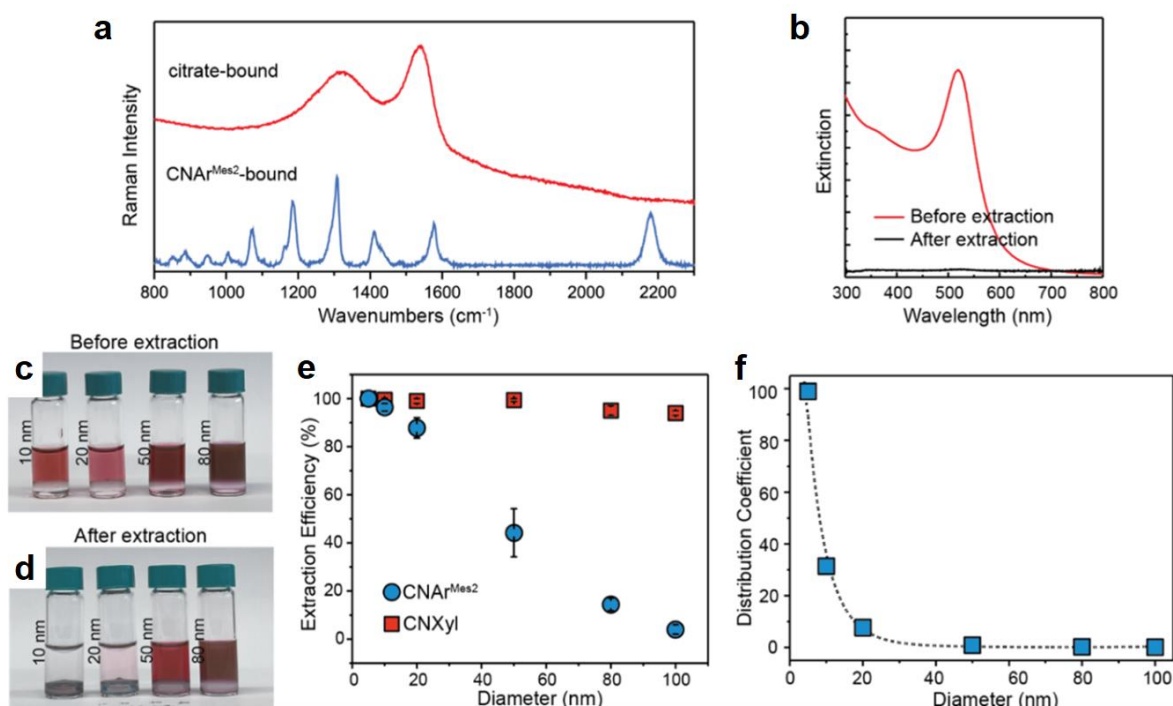


Figure 5.9 Experimental investigation on nanocurvature selectivity by surface-ligand sterics. **(a)** Surface-enhanced Raman spectra for the AuNSs before and after ligand exchange with $\text{CNAr}^{\text{Mes}_2}$ indicating complete displacement of citrate. **(b)** UV-Vis extinction spectra of the aqueous raffinate before and after ligand exchange showing near complete transfer of the AuNSs into the solvent phase. **(c, d)** Photo showing the ligand exchange and solvent transfer of AuNSs of varying diameters, where the top phase is the aqueous raffinate and the bottom phase is chloroform. **(e)** Plot comparing the extraction efficiencies for $\text{CNAr}^{\text{Mes}_2}$ and for the unencumbered CNXyl ligand. **(f)** Plot of the equilibrium distribution coefficient for extraction of the AuNSs into chloroform by $\text{CNAr}^{\text{Mes}_2}$ binding.

ligand adsorption, with larger AuNSs possessing a lower ratio for edge and corner sites than smaller AuNSs. To confirm this, we measured the phase transfer efficiencies for AuNSs with varying diameters, which is dictated by the ligand exchange equilibrium between citrate and $\text{CNAr}^{\text{Mes}_2}$ at the water/chloroform interface. (**Figure 5.9c-e**) The equilibrium distribution coefficient exhibits an asymptotic decay with AuNS diameter consistent with inhibition of isocyanide binding to low-curvature Au surface sites. (**Figure 5.9f**) In contrast, phase transfer using 2,6-dimethylphenyl isocyanide (CNXyl ; $\text{Xyl} = 2,6\text{-Me}_2\text{C}_6\text{H}_3$), which possesses an unencumbered isocyanide head group, exhibits a high exchange efficiency for all AuNS sizes, consistent with indiscriminate Au surface binding.

5.4.2. Investigation of liquid-liquid extraction (LLE)

Classical LLE is often used to separate molecular transition-metal complexes based on their relative solubilities, and involves transfer/partitioning of the desired isolate from liquid phases of differing polarity.[195] In our LLE method, AuNSs serve as the isolate and are partitioned between immiscible aqueous and chloroform phases using $\text{CNAr}^{\text{Mes}_2}$ to facilitate selective solvent transfer based on nanocrystal size.

For size-focusing, we used a starting feedstock of citrate-capped AuNSs with an average particle diameter of 56 ± 6 nm, as obtained by the TEM image analysis (**Figure 5.10a**). After LLE, the extracted AuNSs show a significant reduction in the average diameter and distribution at 54 ± 2 nm. In addition, no AuNSs larger than 64 nm are observed in the chloroform extract, demonstrating the ability to selectively retain larger AuNSs in the aqueous raffinate (**Figure 5.10b**). For size-separation, we used an aqueous feedstock containing a mixture of two AuNS

populations with different average sizes. For a 10/80 nm feedstock, TEM analysis showed that 10 nm particles were the predominant population in the chloroform extract, while 80 nm AuNSs were the exclusive population of the corresponding raffinate (**Figure 5.10c**). OD measurements indicate that 96% of the 80 nm AuNSs remain in the raffinate, which we take as the overall separation efficiency for the 10/80 nm feedstock. We measured the separation efficiency of three additional binary feedstocks (20/80, 10/50, and 20/50 nm), with our results indicating a separation resolution of ~40 nm for our LLE method (**Figure 5.10d**).

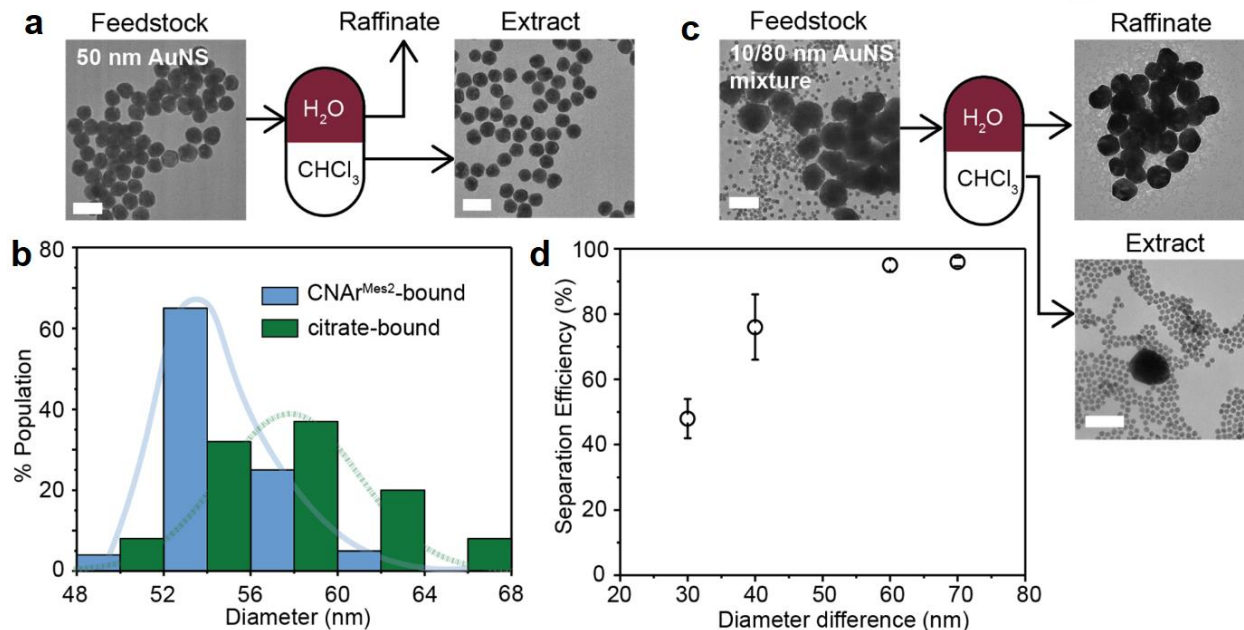


Figure 5.10 Size-selective LLE of AuNS dispersions. **(a)** TEM images of a AuNS dispersion before and after size-focusing. The final AuNS population is extracted from the chloroform phase. **(b)** Size distributions for an AuNS dispersion before (citrate-bound) and after (CNAr^{Mes2}-bound) size-focusing. Tick labels denote a bin size of 4 nm. **(c)** TEM images of AuNSs in the raffinate and extract after LLE was carried out on a binary feedstock of 10 nm and 80 nm citrate-coated AuNSs. **(d)** Plot of separation efficiencies for LLE experiments carried out with the following binary feedstocks: 10/80, 20/80, 10/50, and 20/50 nm AuNS mixtures. Scale bars = 100 nm.

5.5. Conclusions

Combined, our experimental and computational results demonstrate that the steric profile of *m*-terphenyl isocyanides can enable nanocurvature-dependent binding on Au nanocrystal surfaces. We demonstrate that it is the molecular topology of the ligand anchoring group — rather than the ligand coronas — that is responsible for selective isocyanide ligation to edge and corner sites. Articulation of the ligand design principles developed in this work can now be expanded to a vast library of ligands that have already been studied for molecular metal coordination complexes. Importantly, we also find that for colloidal nanocrystals, solvent plays a critical role in not only dictating whether this steric differentiation occurs during the ligand exchange process, but also in determining the dynamics of ligand diffusion, molecular desorption, and solvent extraction after ligand exchange has occurred. Molecular topology of nanocrystal ligands must be co-designed for surface site selectivity *and* solubility. That solvent is capable of fine-tuning ligand-surface interactions perhaps explains why precise nanocrystal surface modification is so difficult to achieve in practice, given that it is only recently that computational approaches have been accurate and efficient enough to obtain microscopic insights into binding, thereby predicting the outcomes of these many-body, complex systems.

5.6. Acknowledgments

Chapter 5, in full, is a modified version of the published materials - Yufei Wang*, Amanda A. Chen*, Krista P. Balto*, Yu Xie, Joshua S. Figueroa, Tod A. Pascal, and Andrea R. Tao. “Curvature-Selective Nanocrystal Surface Ligation Using Sterically-Encumbered Metal-

Coordinating Ligands” (2022), on ACS Nano. The dissertation author is the co-first author who conducts the computational investigation on this work.

CHAPTER 6 : Conclusion

This research centers on investigating molecular behaviors via computational approaches with the thermodynamics backbone to resolve challenges encountered in the environment and industry. Research started from exploring the properties of Carbon Dioxide (CO₂), a dominant heat trapping gas in atmosphere, using both Quantum Mechanics (QM) and Molecular Dynamics (MD) simulations. With Two-Phase Thermodynamic (2PT) theory, we demonstrated our CO₂-Fq forcefield, which was developed based on QM data, was able to perform great agreement with experiments. Afterwards, with the ideas to directly reduce the greenhouse gases amount from daily human life, we put efforts on the battery development. As the results, we showed that fluoromethane (FM), also a type of heat trapping gases, enabled a cell to be operated at low-temperature condition inside Metal-Organic frameworks (MOFs). In addition, the widespread uses of nanoparticle technology caught our attention. For better understanding in nanoparticles-based design, efforts were done for developing an easy control approach toward nanoparticle assembly, which could be achieved by designing a type of curvature-selective adsorption ligands.

Consequently, we introduced general procedures on developing a reliable forcefield, on investigating the characteristics of confined molecules inside MOFs, and on analyzing the selective adsorption by controlling the steric effect of ligands. Future work can be relevant to the forcefield development using the fluctuating atom charge assumption in multi-component systems, the analysis of MOF's flexibility effect in adsorption capacity computations, and the investigation of nanoparticle assembly in a large-scale system, etc.

REFERENCES

- [1] S. Plimpton, Fast Parallel Algorithms for Short-Range Molecular Dynamics, *Journal of Computational Physics* 117 (1995) 1-19.
- [2] Y. Shao, Z. Gan, E. Epifanovsky, A.T. Gilbert, M. Wormit, J. Kussmann, A.W. Lange, A. Behn, J. Deng, X. Feng, Advances in molecular quantum chemistry contained in the Q-Chem 4 program package, *Molecular Physics* 113 (2015) 184-215.
- [3] P. Giannozzi, S. Baroni, N. Bonini, M. Calandra, R. Car, C. Cavazzoni, D. Ceresoli, G.L. Chiarotti, M. Cococcioni, I. Dabo, A.D. Corso, S.d. Gironcoli, S. Fabris, G. Fratesi, R. Gebauer, U. Gerstmann, C. Gougoussis, A. Kokalj, M. Lazzeri, L. Martin-Samos, N. Marzari, F. Mauri, R. Mazzarello, S. Paolini, A. Pasquarello, L. Paulatto, C. Sbraccia, S. Scandolo, G. Sclauzero, A.P. Seitsonen, A. Smogunov, P. Umari, R.M. Wentzcovitch, QUANTUM ESPRESSO: a modular and open-source software project for quantum simulations of materials, *Journal of Physics: Condensed Matter* 21 (2009) 395502.
- [4] P. Giannozzi, O. Andreussi, T. Brumme, O. Bunau, M.B. Nardelli, M. Calandra, R. Car, C. Cavazzoni, D. Ceresoli, M. Cococcioni, N. Colonna, I. Carnimeo, A.D. Corso, S.d. Gironcoli, P. Delugas, R.A.D.J.A.F.A. Floris, G. Fratesi, G. Fugallo, R. Gebauer, U. Gerstmann, F. Giustino, T. Gorni, J. Jia, M. Kawamura, H.-Y. Ko, A. Kokalj, E. Küçükbenli, M. Lazzeri, M. Marsili, N. Marzari, F. Mauri, N.L. Nguyen, H.-V. Nguyen, A. Otero-de-la-Roza, L. Paulatto, S. Poncé, D. Rocca, R. Sabatini, B. Santra, M. Schlipf, A.P. Seitsonen, A. Smogunov, I. Timrov, T. Thonhauser, P. Umari, N. Vast, X. Wu, S. Baroni, Advanced capabilities for materials modelling with Quantum ESPRESSO, *Journal of Physics: Condensed Matter* 29 (2017) 465901.
- [5] M. Etminan, G. Myhre, E. Highwood, K. Shine, Radiative forcing of carbon dioxide, methane, and nitrous oxide: A significant revision of the methane radiative forcing, *Geophysical Research Letters* 43 (2016) 12,614-612,623.
- [6] D.S. Lee, D.W. Fahey, P.M. Forster, P.J. Newton, R.C. Wit, L.L. Lim, B. Owen, R. Sausen, Aviation and global climate change in the 21st century, *Atmospheric Environment* 43 (2009) 3520-3537.
- [7] C. Aymonier, A. Loppinet-Serani, H. Reverón, Y. Garrabos, F. Cansell, Review of supercritical fluids in inorganic materials science, *Journal of Supercritical Fluids* 38 (2006) 242-251.
- [8] F. Lin, D. Liu, S. Maiti Das, N. Prempeh, Y. Hua, J. Lu, Recent progress in heavy metal extraction by supercritical CO₂ fluids, *Industrial & Engineering Chemistry Research* 53 (2014) 1866-1877.

- [9] M. Ohde, H. Ohde, C.M. Wai, Catalytic hydrogenation of arenes with rhodium nanoparticles in a water-in-supercritical CO₂ microemulsion, *Chemical Communications* (2002) 2388-2389.
- [10] H. Ohde, F. Hunt, C.M. Wai, Synthesis of silver and copper nanoparticles in a water-in-supercritical-carbon dioxide microemulsion, *Chemistry of Materials* 13 (2001) 4130-4135.
- [11] M.J. Clarke, K.L. Harrison, K.P. Johnston, S.M. Howdle, Water in supercritical carbon dioxide microemulsions: spectroscopic investigation of a new environment for aqueous inorganic chemistry, *Journal of the American Chemical Society* 119 (1997) 6399-6406.
- [12] S.-D. Yeo, E. Kiran, Formation of polymer particles with supercritical fluids: A review, *Journal of Supercritical Fluids* 34 (2005) 287-308.
- [13] A.K. Rappe, W.A. Goddard III, Charge equilibration for molecular dynamics simulations, *Journal of Physical Chemistry* 95 (1991) 3358-3363.
- [14] D.S. Chiou, H.J. Yu, T.H. Hung, Q. Lyu, C.K. Chang, J.S. Lee, L.C. Lin, D.Y. Kang, Highly CO₂ selective metal–organic framework membranes with favorable coulombic effect, *Advanced Functional Materials* 31 (2021) 2006924.
- [15] H. Li, K. Wang, Y. Sun, C.T. Lollar, J. Li, H.-C. Zhou, Recent advances in gas storage and separation using metal–organic frameworks, *Materials Today* 21 (2018) 108-121.
- [16] J.A. Mason, M. Veenstra, J.R. Long, Evaluating metal–organic frameworks for natural gas storage, *Chemical Science* 5 (2014) 32-51.
- [17] S. Nitopi, E. Bertheussen, S.B. Scott, X. Liu, A.K. Engstfeld, S. Horch, B. Seger, I.E. Stephens, K. Chan, C. Hahn, Progress and perspectives of electrochemical CO₂ reduction on copper in aqueous electrolyte, *Chemical Reviews* 119 (2019) 7610-7672.
- [18] Q. Lu, F. Jiao, Electrochemical CO₂ reduction: Electrocatalyst, reaction mechanism, and process engineering, *Nano Energy* 29 (2016) 439-456.
- [19] C. Kim, H.S. Jeon, T. Eom, M.S. Jee, H. Kim, C.M. Friend, B.K. Min, Y.J. Hwang, Achieving selective and efficient electrocatalytic activity for CO₂ reduction using immobilized silver nanoparticles, *Journal of the American Chemical Society* 137 (2015) 13844-13850.
- [20] C. Kim, T. Eom, M.S. Jee, H. Jung, H. Kim, B.K. Min, Y.J. Hwang, Insight into electrochemical CO₂ reduction on surface-molecule-mediated Ag nanoparticles, *ACS Catalysis* 7 (2017) 779-785.
- [21] Q.-L. Zhu, Q. Xu, Metal–organic framework composites, *Chemical Society Reviews* 43 (2014) 5468-5512.

- [22] D.W. Agnew, M. Gembicky, C.E. Moore, A.L. Rheingold, J.S. Figueroa, Robust, Transformable, and Crystalline Single-Node Organometallic Networks Constructed from Ditopic m-Terphenyl Isocyanides, *Journal of the American Chemical Society* 138 (2016) 15138-15141.
- [23] D. Astruc, F. Lu, J.R. Aranzaes, Nanoparticles as recyclable catalysts: the frontier between homogeneous and heterogeneous catalysis, *Angewandte Chemie International Edition* 44 (2005) 7852-7872.
- [24] A.H. Faraji, P. Wipf, Nanoparticles in cellular drug delivery, *Bioorganic & Medicinal Chemistry* 17 (2009) 2950-2962.
- [25] B.J. Alder, T.E. Wainwright, Phase transition for a hard sphere system, *The Journal of chemical physics* 27 (1957) 1208-1209.
- [26] J.A. McCammon, B.R. Gelin, M. Karplus, Dynamics of folded proteins, *Nature* 267 (1977) 585-590.
- [27] M. Müller, Microdialysis in clinical drug delivery studies, *Advanced drug delivery reviews* 45 (2000) 255-269.
- [28] J.A.R. Willemsen, I.C. Bourg, Molecular dynamics simulation of the adsorption of per- and polyfluoroalkyl substances (PFASs) on smectite clay, *Journal of Colloid Interface Science* 585 (2021) 337-346.
- [29] B. Ravikumar, M. Mynam, B. Rai, Effect of salt concentration on properties of lithium ion battery electrolytes: a molecular dynamics study, *The Journal of Physical Chemistry C* 122 (2018) 8173-8181.
- [30] J. Kadupitiya, G.C. Fox, V. Jadhao, Machine learning for performance enhancement of molecular dynamics simulations, *International Conference on Computational Science*, Springer, 2019, pp. 116-130.
- [31] A.K. Rappi, C.J. Casewit, K.S. Colwell, W.A.G. III, W.M. Skid, UFF, a Full Periodic Table Force Field for Molecular Mechanics and Molecular Dynamics Simulations *J. Am. Chem. Soc.* 114 (1992) 10024-10035.
- [32] R. Salomon-Ferrer, D.A. Case, R.C. Walker, An overview of the Amber biomolecular simulation package, *Wiley Interdisciplinary Reviews: Computational Molecular Science* 3 (2013) 198-210.
- [33] S.L.M.B.D. Olafson, W.A. Goddard, DREIDING: a generic force field for molecular simulations, *Journal of Physical Chemistry* 94 (1990) 8897-8909.

- [34] P. Mark, L. Nilsson, Structure and Dynamics of the TIP3P, SPC, and SPC/E Water Models at 298 K, *Journal of Physical Chemistry A* 105 (2001) 9954-9960.
- [35] J.G. Harris, K.H. Yung, Carbon dioxide's liquid-vapor coexistence curve and critical properties as predicted by a simple molecular model, *Journal of Physical Chemistry* 99 (1995) 12021-12024.
- [36] L.E. Ballentine, *Quantum mechanics: a modern development*, World Scientific Publishing Company 2014.
- [37] C. Davisson, L.H. Germer, The scattering of electrons by a single crystal of nickel, *Nature* 119 (1927) 558-560.
- [38] L. de Broglie, The reinterpretation of wave mechanics, *Foundations of Physics* 1 (1970) 5-15.
- [39] F.T. Hioe, J.H. Eberly, N-level coherence vector and higher conservation laws in quantum optics and quantum mechanics, *Physical Review Letters* 47 (1981) 838.
- [40] F. Weinert, Franck—Hertz Experiment, *Compendium of Quantum Physics*, Springer 2009, pp. 241-243.
- [41] P.M. Koch, L. Moorman, B.E. Sauer, E.J. Galvez, K.A.H. van Leeuwen, D. Richards, Experiments in quantum chaos: microwave ionization of hydrogen atoms, *Physica Scripta* 1989 (1989) 51.
- [42] M.D. Feit, J.A. Fleck Jr., A. Steiger, Solution of the Schrödinger equation by a spectral method, *Journal of Computational Physics* 47 (1982) 412-433.
- [43] M. Born, Statistical interpretation of quantum mechanics, *Science* 122 (1955) 675-679.
- [44] E.O. Brigham, *The fast Fourier transform and its applications*, Prentice-Hall, Inc. 1988.
- [45] B.J.B. Crowley, R. Bingham, R.G. Evans, D.O. Gericke, O.L. Landen, C.D. Murphy, P.A. Norreys, S.J. Rose, T. Tschentscher, C.H.-T. Wang, J.S. Wark, G. Gregori, Testing quantum mechanics in non-Minkowski space-time with high power lasers and 4th generation light sources, *Scientific Reports* 2 (2012) 1-4.
- [46] P. Kruit, R.G. Hobbs, C.-S. Kim, Y. Yang, V.R. Manfrinato, J. Hammer, S. Thomas, P. Weber, B. Klopfer, C. Kohstall, T. Juffmann, M.A. Kasevich, P. Hommelhoff, K.K. Berggren, Designs for a quantum electron microscope, *Ultramicroscopy* 164 (2016) 31-45.
- [47] S.F. Keevil, Magnetic resonance imaging in medicine, *Physics Education* 36 (2001) 476.

- [48] B. Robson, J.S. Clair, Principles of Quantum Mechanics for artificial intelligence in medicine. Discussion with reference to the Quantum Universal Exchange Language (Q-UEL), *Computers in Biology and Medicine* (2022) 105323.
- [49] J. Cheng, X. Yuan, L. Zhao, D. Huang, M. Zhao, L. Dai, R. Ding, GCMC simulation of hydrogen physisorption on carbon nanotubes and nanotube arrays, *Carbon* 42 (2004) 2019-2024.
- [50] Y.R. Tao, G.H. Zhang, H.J. Xu, Grand canonical Monte Carlo (GCMC) study on adsorption performance of metal organic frameworks (MOFs) for carbon capture, *Sustainable Materials and Technologies* 32 (2022) e00383.
- [51] P. Cosoli, M. Ferrone, S. Pricl, M. Fermeglia, Hydrogen sulphide removal from biogas by zeolite adsorption: Part I. GCMC molecular simulations, *Chemical Engineering Journal* 145 (2008) 86-92.
- [52] M. Shadman, S. Yeganegi, M.R. Galugahi, Hydrogen physisorption and selectivity in single-walled silicon carbon nanotubes: a grand canonical Monte-Carlo study, *Journal of the Iranian Chemical Society* 13 (2016) 207-220.
- [53] D. Lüthi, M. Le Floch, B. Bereiter, T. Blunier, J.-M. Barnola, U. Siegenthaler, D. Raynaud, J. Jouzel, H. Fischer, K. Kawamura, High-resolution carbon dioxide concentration record 650,000–800,000 years before present, *Nature* 453 (2008) 379-382.
- [54] G.L. Schott, Shock-compressed carbon dioxide: liquid measurements and comparisons with selected models, *International Journal of High Pressure Research* 6 (1991) 187-200.
- [55] W.J. Nellis, A.C. Mitchell, F.H. Ree, M. Ross, N.C. Holmes, R.J. Trainor, D.J. Erskine, Equation of state of shock-compressed liquids: Carbon dioxide and air, *Journal of Chemical Physics* 95 (1991) 5268-5272.
- [56] S. Root, K.R. Cochrane, J.H. Carpenter, T. Mattsson, Carbon dioxide shock and reshock equation of state data to 8 Mbar: Experiments and simulations, *Physical Review B* 87 (2013) 224102.
- [57] T.T. Trinh, T.J.H. Vlugt, S. Kjelstrup, Thermal conductivity of carbon dioxide from non-equilibrium molecular dynamics: A systematic study of several common force fields, *Journal of Chemical Physics* 141 (2014) 134504.
- [58] A.Z. Panagiotopoulos, Direct determination of phase coexistence properties of fluids by Monte Carlo simulation in a new ensemble, *Molecular Physics* 61 (1987) 813-826.
- [59] T. Yagasaki, M. Matsumoto, H. Tanaka, Phase diagrams of TIP4P/2005, SPC/E, and TIP5P water at high pressure, *Journal of Physical Chemistry B* 122 (2018) 7718-7725.

- [60] D. Frenkel, B. Smit, *Understanding molecular simulation: from algorithms to applications*, Academic press 2001.
- [61] M.M. Conde, C. Vega, Determining the three-phase coexistence line in methane hydrates using computer simulations, *Journal of Chemical Physics* 133 (2010) 064507.
- [62] P.M. Piaggi, M. Parrinello, Calculation of phase diagrams in the multithermal-multibaric ensemble, *Journal of Chemical Physics* 150 (2019) 244119.
- [63] S.-N. Huang, T.A. Pascal, W.A. Goddard III, P.K. Maiti, S.-T. Lin, Absolute Entropy and Energy of Carbon Dioxide Using the Two-Phase Thermodynamic Model, *Journal of Chemical Theory and Computation* 7 (2011) 1893-1901.
- [64] S.-T. Lin, M. Blanco, W.A. Goddard III, The two-phase model for calculating thermodynamic properties of liquids from molecular dynamics: Validation for the phase diagram of Lennard-Jones fluids, *Journal of Chemical Physics* 119 (2003) 11792-11805.
- [65] S.-T. Lin, P.K. Maiti, W.A. Goddard III, Two-phase thermodynamic model for efficient and accurate absolute entropy of water from molecular dynamics simulations, *Journal of Physical Chemistry B* 114 (2010) 8191-8198.
- [66] M.P. Desjarlais, First-principles calculation of entropy for liquid metals, *Physical Review E* 88 (2013) 062145.
- [67] C. Zhang, L. Spanu, G. Galli, Entropy of liquid water from ab initio molecular dynamics, *Journal of Physical Chemistry B* 115 (2011) 14190-14195.
- [68] M.S. Shell, *Thermodynamics and statistical mechanics: an integrated approach*, Cambridge University Press 2015.
- [69] G.A. Mansoori, N.F. Carnahan, K.E. Starling, T.W. Leland Jr, Equilibrium thermodynamic properties of the mixture of hard spheres, *Journal of Chemical Physics* 54 (1971) 1523-1525.
- [70] N.F. Carnahan, K.E. Starling, Thermodynamic properties of a rigid-sphere fluid, *Journal of Chemical Physics* 53 (1970) 600-603.
- [71] P.H. Berens, D.H.J. Mackay, G.M. White, K.R. Wilson, Thermodynamics and Quantum Corrections from Molecular-Dynamics for Liquid Water, *Journal of Chemical Physics* 79 (1983) 2375-2389.
- [72] H. Eyring, T. Ree, Significant liquid structures, VI. The vacancy theory of liquids. , *Proceedings of the National Academy of Sciences* 47 (1961) 526-537.

- [73] T.A. Pascal, W.A. Goddard III, Interfacial thermodynamics of water and six other liquid solvents, *Journal of Physical Chemistry B* 118 (2014) 5943-5956.
- [74] T.A. Pascal, S.-T. Lin, W.A. Goddard III, Thermodynamics of liquids: standard molar entropies and heat capacities of common solvents from 2PT molecular dynamics, *Physical Chemistry Chemical Physics* 13 (2011) 169-181.
- [75] A. Warshel, M. Kato, A.V. Pisliakov, Polarizable force fields: History, test cases, and prospects, *Journal of Chemical Theory and Computation* 3 (2007) 2034-2045.
- [76] G. Lamoureux, B. Roux, Modeling induced polarization with classical Drude oscillators: Theory and molecular dynamics simulation algorithm, *Journal of chemical physics* 119 (2003) 3025-3039.
- [77] T.A. Halgren, W. Damm, Polarizable force fields, *Current Opinion in Structural Biology* 11 (2001) 236-242.
- [78] P. Ren, J.W. Ponder, Consistent treatment of inter-and intramolecular polarization in molecular mechanics calculations, *Journal of Computational Chemistry* 23 (2002) 1497-1506.
- [79] J.W. Ponder, C. Wu, P. Ren, V.S. Pande, J.D. Chodera, M.J. Schnieders, I. Haque, D.L. Mobley, D.S. Lambrecht, R.A. DiStasio Jr, Current status of the AMOEBA polarizable force field, *Journal of Physical Chemistry B* 114 (2010) 2549-2564.
- [80] O. Borodin, Polarizable force field development and molecular dynamics simulations of ionic liquids, *Journal of Physical Chemistry B* 113 (2009) 11463-11478.
- [81] R.T. Sanderson, *Chemical bonds and bond energy*, Academic Press, New York, 1976.
- [82] R.S. Mulliken, A new electroaffinity scale; together with data on valence states and on valence ionization potentials and electron affinities, *Journal of Chemical Physics* 2 (1934) 782-793.
- [83] W.J. Mortier, K. Van Genechten, J. Gasteiger, Electronegativity equalization: application and parametrization, *Journal of the American Chemical Society* 107 (1985) 829-835.
- [84] S.W. Rick, S.J. Stuart, B. Berne, Dynamical fluctuating charge force fields: Application to liquid water, *Journal of chemical physics* 101 (1994) 6141-6156.
- [85] J. Chen, T.J. Martínez, QTPIE: Charge transfer with polarization current equalization. A fluctuating charge model with correct asymptotics, *Chemical Physics Letters* 438 (2007) 315-320.

- [86] J.J. Oppenheim, S. Naserifar, W.A. Goddard III, Extension of the polarizable charge equilibration model to higher oxidation states with applications to Ge, As, Se, Br, Sn, Sb, Te, I, Pb, Bi, Po, and at elements, *Journal of Physical Chemistry A* 122 (2017) 639-645.
- [87] S. Naserifar, D.J. Brooks, W.A. Goddard III, V. Cvicek, Polarizable charge equilibration model for predicting accurate electrostatic interactions in molecules and solids, *Journal of Chemical Physics* 146 (2017) 124117.
- [88] G. Bergerhoff, I. Brown, F. Allen, *Crystallographic databases*, International Union of Crystallography, Chester 360 (1987) 77-95.
- [89] D. Zagorac, H. Müller, S. Ruehl, J. Zagorac, S. Rehme, Recent developments in the Inorganic Crystal Structure Database: theoretical crystal structure data and related features, *Journal of applied crystallography* 52 (2019) 918-925.
- [90] E. Lemmon, *Thermophysical Properties of Fluid Systems*, NIST chemistry WebBook, NIST standard reference database number 69, <http://webbook.nist.gov>, 2005.
- [91] <https://github.com/atlas-nano/2PT>
- [92] S. Naserifar, J.J. Oppenheim, H. Yang, T. Zhou, S. Zybin, M. Rizk, W.A. Goddard III, Accurate non-bonded potentials based on periodic quantum mechanics calculations for use in molecular simulations of materials and systems, *Journal of Chemical Physics* 151 (2019) 154111.
- [93] S. Naserifar, W.A. Goddard III, The quantum mechanics-based polarizable force field for water simulations, *Journal of Chemical Physics* 149 (2018) 174502.
- [94] H.M. Aktulga, J.C. Fogarty, S.A. Pandit, A.Y. Grama, Parallel reactive molecular dynamics: Numerical methods and algorithmic techniques, *Parallel Computing* 38 (2012) 245-259.
- [95] M. Ceriotti, G. Bussi, M. Parrinello, Colored-noise thermostats à la carte, *Journal of Chemical Theory and Computation* 6 (2010) 1170-1180.
- [96] M. Ceriotti, G. Bussi, M. Parrinello, Nuclear quantum effects in solids using a colored-noise thermostat, *Physical Review Letters* 103 (2009) 030603.
- [97] Generated at <http://cosmo-epfl.github.io/gle4md>
- [98] S.M. Valone, S.R. Atlas, An empirical charge transfer potential with correct dissociation limits, *Journal of Chemical Physics* 120 (2004) 7262-7273.
- [99] A.W. Nowicki, M. Ghosh, S.M. McClellan, D.T. Jacobs, Heat capacity and turbidity near the critical point of succinonitrile–water, *Journal of Chemical Physics* 114 (2001) 4625-4633.

- [100] J.A. Lipa, C. Edwards, M.J. Buckingham, Specific heat of CO₂ near the critical point, *Physical Review A* 15 (1977) 778-789.
- [101] A.H. Harvey, R.D. Mountain, Correlations for the Dielectric Constants of H₂S, SO₂, and SF₆, *International Journal of Thermophysics* 38 (2017) 147.
- [102] E.J. Beckman, Supercritical and near-critical CO₂ in green chemical synthesis and processing, *Journal of Supercritical Fluids* 28 (2004) 121–191.
- [103] M.P. Allen, D.J. Tildesley, *Computer simulation of liquids*, Oxford university press 2017.
- [104] C. Yaws, *Chemical Properties Handbook: physical, thermodynamic, environmental, transport, safety, and health related properties for organic and inorganic chemicals*, McGraw-Hill: 1999.
- [105] T.A. Pascal, C.P. Schwartz, K.V. Lawler, D. Prendergast, The purported square ice in bilayer graphene is a nanoscale, monolayer object, *Journal of Chemical Physics* 150 (2019) 231101.
- [106] B.R. Shrestha, S. Pillai, A. Santana, S.H. Donaldson Jr, T.A. Pascal, H. Mishra, Nuclear quantum effects in hydrophobic nanoconfinement, *Journal of Physical Chemistry Letters* 10 (2019) 5530-5535.
- [107] T.A. Pascal, K.H. Wujcik, D.R. Wang, N.P. Balsara, D. Prendergast, Thermodynamic origins of the solvent-dependent stability of lithium polysulfides from first principles, *Physical Chemistry Chemical Physics* 19 (2017) 1441-1448.
- [108] T.A. Pascal, I. Villaluenga, K.H. Wujcik, D. Devaux, X. Jiang, D.R. Wang, N. Balsara, D. Prendergast, Liquid sulfur impregnation of microporous carbon accelerated by nanoscale interfacial effects, *Nano letters* 17 (2017) 2517-2523.
- [109] T.A. Pascal, D. Schärf, Y. Jung, T.D. Kühne, On the absolute thermodynamics of water from computer simulations: A comparison of first-principles molecular dynamics, reactive and empirical force fields, *Journal of Chemical Physics* 137 (2012) 244507.
- [110] J. Sun, D.D. Klug, R. Martoňák, J.A. Montoya, M.-S. Lee, S. Scandolo, E. Tosatti, High-pressure polymeric phases of carbon dioxide, *Proceedings of the National Academy of Sciences* 106 (2009) 6077-6081.
- [111] F. Datchi, M. Moog, F. Pietrucci, A.M. Saitta, Polymeric phase V of carbon dioxide has not been recovered at ambient pressure and has a unique structure, *Proceedings of the National Academy of Sciences* 114 (2017) E656-E657.
- [112] D. Mathieu, Split charge equilibration method with correct dissociation limits, *Journal of Chemical Physics* 127 (2007) 224103.

- [113] M.C. Smart, B.V. Ratnakumar, R.C. Ewell, S. Surampudi, F.J. Puglia, R. Gitzendanner, The use of lithium-ion batteries for JPL's Mars missions, *Electrochimica Acta* 268 (2018) 27-40.
- [114] K.B. Chin, E.J. Brandon, R.V. Bugga, M.C. Smart, S.C. Jones, F.C. Krause, W.C. West, G.G. Bolotin, Energy storage technologies for small satellite applications, *Proceedings of the IEEE* 106 (2018) 419-428.
- [115] M.-T.F. Rodrigues, G. Babu, H. Gullapalli, K. Kalaga, F.N. Sayed, K. Kato, J. Joyner, P.M. Ajayan, A materials perspective on Li-ion batteries at extreme temperatures, *Nature Energy* 2 (2017) 1-14.
- [116] J. Jaguemont, L. Boulon, Y. Dubé, A comprehensive review of lithium-ion batteries used in hybrid and electric vehicles at cold temperatures, *Applied Energy* 164 (2016) 99-114.
- [117] A. Gupta, A. Manthiram, Designing advanced lithium-based batteries for low-temperature Conditions, *Advanced Energy Materials* 10 (2020) 2001972.
- [118] X. Fan, X. Ji, L. Chen, J. Chen, T. Deng, F. Han, J. Yue, N. Piao, R. Wang, X. Zhou, All-temperature batteries enabled by fluorinated electrolytes with non-polar solvents, *Nature Energy* 4 (2019) 882-890.
- [119] X. Dong, Y. Lin, P. Li, Y. Ma, J. Huang, D. Bin, Y. Wang, Y. Qi, Y. Xia, High-energy rechargeable metallic lithium battery at -70 C enabled by a cosolvent electrolyte, *Angewandte Chemie International Edition* 58 (2019) 5623-5627.
- [120] G. Cai, J. Holoubek, D. Xia, M. Li, Y. Yin, X. Xing, P. Liu, Z. Chen, An ester electrolyte for lithium-sulfur batteries capable of ultra-low temperature cycling, *Chemical Communications* 56 (2020) 9114-9117.
- [121] Q. Li, D. Lu, J. Zheng, S. Jiao, L. Luo, C.-M. Wang, K. Xu, J.-G. Zhang, W. Xu, Li⁺-desolvation dictating lithium-ion battery's low-temperature performances, *ACS Applied Materials Interfaces* 9 (2017) 42761-42768.
- [122] Y. Ji, C.Y. Wang, Heating strategies for Li-ion batteries operated from subzero temperatures, *Electrochimica Acta* 107 (2013) 664-674.
- [123] C.-Y. Wang, G. Zhang, S. Ge, T. Xu, Y. Ji, X.-G. Yang, Y. Leng, Lithium-ion battery structure that self-heats at low temperatures, *Nature* 529 (2016) 515-518.
- [124] W.C. West, A. Shevade, J. Soler, J. Kulleck, M. Smart, B. Ratnakumar, M. Moran, R. Haiges, K.O. Christe, G.S. Prakash, Sulfuryl and thionyl halide-based ultralow temperature primary batteries, *Journal of The Electrochemical Society* 157 (2010) A571.

- [125] A.J. Hills, N.A. Hampson, The Li-SOCl₂ cell—a review, *Journal of Power Sources* 24 (1988) 253-271.
- [126] C.R. Schlaikjer, F. Goebel, N. Marincic, Discharge reaction mechanisms in Li/SOCl₂ cells, *Journal of the Electrochemical Society* 126 (1979) 513.
- [127] C.S. Rustomji, Y. Yang, T.K. Kim, J. Mac, Y.J. Kim, E. Caldwell, H. Chung, Y.S. Meng, Liquefied gas electrolytes for electrochemical energy storage devices, *Science* 356 (2017) eaal4263.
- [128] Y. Yang, D.M. Davies, Y. Yin, O. Borodin, J.Z. Lee, C. Fang, M. Olguin, Y. Zhang, E.S. Sablina, X. Wang, High-efficiency lithium-metal anode enabled by liquefied gas electrolytes, *Joule* 3 (2019) 1986-2000.
- [129] Y. Yang, Y. Yin, D.M. Davies, M. Zhang, M. Mayer, Y. Zhang, E.S. Sablina, S. Wang, J.Z. Lee, O. Borodin, Liquefied gas electrolytes for wide-temperature lithium metal batteries, *Energy Environmental Science* 13 (2020) 2209-2219.
- [130] L.R. Fisher, J.N. Israelachvili, Direct experimental verification of the Kelvin equation for capillary condensation, *Nature* 277 (1979) 548-549.
- [131] A.C. Mitropoulos, The kelvin equation, *Journal of Colloid Interface Science* 317 (2008) 643-648.
- [132] L. Li, J.J. Sheng, Nanopore confinement effects on phase behavior and capillary pressure in a Wolfcamp shale reservoir, *Journal of the Taiwan Institute of Chemical Engineers* 78 (2017) 317-328.
- [133] E. Barsotti, S.P. Tan, S. Saraji, M. Piri, J.-H. Chen, A review on capillary condensation in nanoporous media: Implications for hydrocarbon recovery from tight reservoirs, *Fuel* 184 (2016) 344-361.
- [134] T. Horikawa, D.D. Do, D. Nicholson, Capillary condensation of adsorbates in porous materials, *Advances in Colloid and Interface Science* 169 (2011) 40-58.
- [135] P.N. Aukett, N. Quirke, S. Riddiford, S.R. Tennison, Methane adsorption on microporous carbons—a comparison of experiment, theory, and simulation, *Carbon* 30 (1992) 913-924.
- [136] B. Li, H.-M. Wen, W. Zhou, J.Q. Xu, B. Chen, Porous metal-organic frameworks: promising materials for methane storage, *Chem* 1 (2016) 557-580.
- [137] A.B. Grommet, M. Feller, R. Klajn, Chemical reactivity under nanoconfinement, *Nature Nanotechnology* 15 (2020) 256-271.

- [138] H. Furukawa, K.E. Cordova, M. O’Keeffe, O.M. Yaghi, The chemistry and applications of metal-organic frameworks, *Science* 341 (2013) 1230444.
- [139] H.-C. Zhou, S. Kitagawa, Metal–organic frameworks (MOFs), *Chemical Society Reviews* 43 (2014) 5415-5418.
- [140] G. Cai, M. Ding, Q. Wu, H.-L. Jiang, Encapsulating soluble active species into hollow crystalline porous capsules beyond integration of homogeneous and heterogeneous catalysis, *National Science Review* 7 (2020) 37-45.
- [141] Y. Peng, Y. Li, Y. Ban, H. Jin, W. Jiao, X. Liu, W. Yang, Metal-organic framework nanosheets as building blocks for molecular sieving membranes, *Science* 346 (2014) 1356-1359.
- [142] Z. Chen, P. Li, R. Anderson, X. Wang, X. Zhang, L. Robison, L.R. Redfern, S. Moribe, T. Islamoglu, D.A. Gómez-Gualdrón, Balancing volumetric and gravimetric uptake in highly porous materials for clean energy, *Science* 368 (2020) 297-303.
- [143] S. Li, Y. Dong, J. Zhou, Y. Liu, J. Wang, X. Gao, Y. Han, P. Qi, B. Wang, Carbon dioxide in the cage: manganese metal–organic frameworks for high performance CO₂ electrodes in Li–CO₂ batteries, *Energy & Environmental Science* 11 (2018) 1318-1325.
- [144] J.M.M.d. Maia, J. Mota, Molecular simulation of gas adsorption equilibria in nanoporous materials, 2014.
- [145] P.G. Boyd, S.M. Moosavi, M. Witman, B. Smit, Force-Field Prediction of Materials Properties in Metal-Organic Frameworks, *J. Phys. Chem. Lett.* 8 (2017) 357-363.
- [146] H. Böhm, C. Meissner, R. Ahlrichs, Molecular dynamics simulation of liquid CH₃F, CHF₃, CH₃Cl, CH₃CN, CO₂ and CS₂ with new pair potentials, *Molecular Physics* 53 (1984) 651-672.
- [147] C.G. Aimoli, E.J. Maginn, C.R.A. Abreu, Force field comparison and thermodynamic property calculation of supercritical CO₂ and CH₄ using molecular dynamics simulations, *Fluid Phase Equilibria* 368 (2014) 80-90.
- [148] M.G. Martin, MCCCSTowhee: a tool for Monte Carlo molecular simulation, *Molecular Simulation* 39 (2013) 1212-1222.
- [149] G.E. Cmarik, M. Kim, S.M. Cohen, K.S. Walton, Tuning the adsorption properties of UiO-66 via ligand functionalization, *Langmuir* 28 (2012) 15606-15613.
- [150] J.H. Cavka, C.A. Grande, G. Mondino, R. Blom, High pressure adsorption of CO₂ and CH₄ on Zr-MOFs, *Industrial & Engineering Chemistry Research* 53 (2014) 15500-15507.

- [151] M.S. Shell, *Thermodynamics and statistical mechanics: an integrated approach*, Cambridge University Press 2015.
- [152] W. Shinoda, M. Shiga, M. Mikami, Rapid estimation of elastic constants by molecular dynamics simulation under constant stress, *Physical Review B* 69 (2004) 134103.
- [153] G.J. Martyna, D.J. Tobias, M.L. Klein, Constant pressure molecular dynamics algorithms, *The Journal of Chemical Physics* 101 (1994) 4177-4189.
- [154] M. Parrinello, A. Rahman, Polymorphic transitions in single crystals: A new molecular dynamics method, *Journal of Applied physics* 52 (1981) 7182-7190.
- [155] M.E. Tuckerman, J. Alejandre, R. López-Rendón, A.L. Jochim, G.J. Martyna, General, A Liouville-operator derived measure-preserving integrator for molecular dynamics simulations in the isothermal–isobaric ensemble, *Journal of Physics A: Mathematical* 39 (2006) 5629.
- [156] G. Cai, Y. Yin, D. Xia, A.A. Chen, J. Holoubek, J. Scharf, Y. Yang, K.H. Koh, M. Li, D.M. Davies, M. Mayer, T.H. Han, Y.S. Meng, T.A. Pascal, Z. Chen, Sub-nanometer confinement enables facile condensation of gas electrolyte for low-temperature batteries, *Nature Communications* 12 (2021).
- [157] P. Chiochan, X. Yu, M. Sawangphruk, A. Manthiram, A metal organic framework derived solid electrolyte for lithium–sulfur batteries, *Advanced Energy Materials* 10 (2020) 2001285.
- [158] S. Bai, X. Liu, K. Zhu, S. Wu, H. Zhou, Metal–organic framework-based separator for lithium–sulfur batteries, *Nature Energy* 1 (2016) 1-6.
- [159] R. Zhao, Z. Liang, R. Zou, Q. Xu, Metal-organic frameworks for batteries, *Joule* 2 (2018) 2235-2259.
- [160] V. Kovalenko Maksym, M. Scheele, V. Talapin Dmitri, Colloidal Nanocrystals with Molecular Metal Chalcogenide Surface Ligands, *Science* 324 (2009) 1417-1420.
- [161] H. Kim Byung, J. Heo, S. Kim, F. Reboul Cyril, H. Chun, D. Kang, H. Bae, H. Hyun, J. Lim, H. Lee, B. Han, T. Hyeon, A.P. Alivisatos, P. Ercius, H. Elmlund, J. Park, Critical differences in 3D atomic structure of individual ligand-protected nanocrystals in solution, *Science* 368 (2020) 60-67.
- [162] C. Yi, H. Liu, S. Zhang, Y. Yang, Y. Zhang, Z. Lu, E. Kumacheva, Z. Nie, Self-limiting directional nanoparticle bonding governed by reaction stoichiometry, *Science* 369 (2020) 1369-1374.

- [163] Y. Nagaoka, R. Tan, R. Li, H. Zhu, D. Eggert, Y.A. Wu, Y. Liu, Z. Wang, O. Chen, Superstructures generated from truncated tetrahedral quantum dots, *Nature* 561 (2018) 378-382.
- [164] P.J. Santos, P.A. Gabrys, L.Z. Zornberg, M.S. Lee, R.J. Macfarlane, Macroscopic materials assembled from nanoparticle superlattices, *Nature* 591 (2021) 586-591.
- [165] E. Villarreal, G.G. Li, Q. Zhang, X. Fu, H. Wang, Nanoscale Surface Curvature Effects on Ligand–Nanoparticle Interactions: A Plasmon-Enhanced Spectroscopic Study of Thiolated Ligand Adsorption, Desorption, and Exchange on Gold Nanoparticles, *Nano Letters* 17 (2017) 4443-4452.
- [166] N.C. Anderson, P.E. Chen, A.K. Buckley, J.D. Roo, J.S. Owen, Stereoelectronic Effects on the Binding of Neutral Lewis Bases to CdSe Nanocrystals, *Journal of the American Chemical Society* 140 (2018) 7199-7205.
- [167] P.P. Power, Some highlights from the development and use of bulky monodentate ligands, *Journal of Organometallic Chemistry* 689 (2004) 3904-3919.
- [168] P.P. Power, Stable Two-Coordinate, Open-Shell (d1–d9) Transition Metal Complexes, *Chemical Reviews* 112 (2012) 3482-3507.
- [169] E. Rivard, P.P. Power, Multiple Bonding in Heavier Element Compounds Stabilized by Bulky Terphenyl Ligands, *Inorganic Chemistry* 46 (2007) 10047-10064.
- [170] J.A.C. Clyburne, N. McMullen, Unusual structures of main group organometallic compounds containing m-terphenyl ligands, *Coordination Chemistry Reviews* 210 (2000) 73-99.
- [171] D.L. Kays, The stabilisation of organometallic complexes using m-terphenyl ligands, *Organometallic Chemistry* 36 (2010) 56-76.
- [172] B.J. Fox, Q.Y. Sun, A.G. Dipasquale, A.R. Fox, A.L. Rheingold, J.S. Figueroa, Solution behavior and structural properties of Cu(I) complexes featuring m-terphenyl isocyanides, *Inorganic Chemistry* 47 (2008) 9010-9020.
- [173] T. Ditri, B. Fox, C. Moore, A. Rheingold, J. Figueroa, Effective Control of Ligation and Geometric Isomerism: Direct Comparison of Steric Properties Associated with Bis-mesityl and Bis-diisopropylphenyl m-Terphenyl Isocyanides, *Inorganic Chemistry* 48 (2009) 8362-8375.
- [174] A.E. Carpenter, C.C. Mokhtarzadeh, D.S. Ripatti, I. Havrylyuk, R. Kamezawa, C.E. Moore, A.L. Rheingold, J.S. Figueroa, Comparative Measure of the Electronic Influence of Highly Substituted Aryl Isocyanides, *Inorganic Chemistry* 54 (2015) 2936-2944.

- [175] G.J. Ackland, G. Tichy, V. Vitek, M.W. Finnis, Simple N-body potentials for the noble metals and nickel, *Philosophical Magazine A* 56 (1987) 735-756.
- [176] J. Wang, R.M. Wolf, J.W. Caldwell, P.A. Kollman, D.A. Case, Development and testing of a general amber force field, *Journal of Computational Chemistry* 25 (2004) 1157-1174.
- [177] G.A. Kaminski, R.A. Friesner, J. Tirado-Rives, W.L. Jorgensen, Evaluation and reparametrization of the OPLS-AA force field for proteins via comparison with accurate quantum chemical calculations on peptides, *The Journal of Physical Chemistry B* 105 (2001) 6474-6487.
- [178] G. Kamath, G. Georgiev, J.J. Potoff, Molecular Modeling of Phase Behavior and Microstructure of Acetone-Chloroform-Methanol Binary Mixtures, *Journal of Physical Chemistry B* 109 (2005) 19463-19473.
- [179] M. Karg, N. Schelero, C. Oppel, M. Gradzielski, T. Hellweg, R. von Klitzing, Versatile phase transfer of gold nanoparticles from aqueous media to different organic media, *Chemistry* 17 (2011) 4648-4654.
- [180] Hockney, Eastwood, *Computer Simulation Using Particles*, Adam Hilger, NY (1989).
- [181] A.A. Chen, A. Do, T.A. Pascal, The Phase Diagram of Carbon Dioxide from Correlation Functions and a Many-body Potential, *Journal of Chemical Physics* 155 (2021) 024503.
- [182] R.W. Zwanzig, High-Temperature Equation of State by a Perturbation Method. I. Nonpolar Gases, *Journal of Chemical Physics* 22 (1954) 1420.
- [183] H. Liu, J. Holoubek, H. Zhou, A. Chen, N. Chang, Z. Wu, S. Yu, Q. Yan, X. Xing, Y. Li, T.A. Pascal, P. Liu, Ultrahigh coulombic efficiency electrolyte enables Li||SPAN batteries with superior cycling performance, *Materials Today* 42 (2021) 17-28.
- [184] P. Mahinthichaichan, Q.N. Vo, C.R. Ellis, J. Shen, Kinetics and Mechanism of Fentanyl Dissociation from the μ -Opioid Receptor, *American Chemical Society* 1 (2021) 2208-2215.
- [185] Y. Wang, A.A. Chen, K.P. Balto, Y. Xie, J.S. Figueroa, T.A. Pascal, A.R. Tao, Curvature-Selective Nanocrystal Surface Ligation Using Sterically-Encumbered Metal-Coordinating Ligands, *ACS Nano* 16 (2022) 12747-12754.
- [186] M.J. Robertson, R.J. Angelici, Adsorption of Aryl and Alkyl Isocyanides on Powdered Gold, *Langmuir* 10 (1994) 1488-1492.
- [187] K.-C. Shih, R.J. Angelici, Equilibrium and Saturation Coverage Studies of Alkyl and Aryl Isocyanides on Powdered Gold, *Langmuir* 11 (1995) 2539-2546.

- [188] A.C. Ontko, R.J. Angelici, Effects of Alkyl Chain Length on the Adsorption of n-Alkyl Isocyanides (RN:C) on Gold Powder, *Langmuir* 14 (1998) 1684-1691.
- [189] B.R. Martin, D.J. Dermody, B.D. Reiss, M. Fang, L.A. Lyon, M.J. Natan, T.E. Mallouk, Orthogonal Self-Assembly on Colloidal Gold-Platinum Nanorods, *Advanced Materials* 11 (1999) 1021-1025.
- [190] J.I. Henderson, S. Feng, T. Bein, C.P. Kubiak, Adsorption of Diisocyanides on Gold, *Langmuir* 16 (2000) 6183-6187.
- [191] S.J. Bae, C.-r. Lee, I.S. Choi, C.-S. Hwang, M.-s. Gong, K. Kim, S.-W. Joo, Adsorption of 4-Biphenylisocyanide on Gold and Silver Nanoparticle Surfaces: Surface-Enhanced Raman Scattering Study, *The Journal of Physical Chemistry B* 106 (2002) 7076-7080.
- [192] J. Ahn, S. Shi, B. Vannatter, D. Qin, Comparative Study of the Adsorption of Thiol and Isocyanide Molecules on a Silver Surface by in Situ Surface-Enhanced Raman Scattering, *The Journal of Physical Chemistry C* 123 (2019) 21571-21580.
- [193] A. Arroyave, M. Gembicky, A.L. Rheingold, J.S. Figueroa, Aqueous Stability and Ligand Substitution of a Layered Cu(I)/Isocyanide-Based Organometallic Network Material with a Well-Defined Channel Structure, *Inorganic Chemistry* 59 (2020) 11868-11878.
- [194] K.P. Balto, M. Gembicky, A.L. Rheingold, J.S. Figueroa, Crystalline Hydrogen-Bonding Networks and Mixed-Metal Framework Materials Enabled by an Electronically Differentiated Heteroditopic Isocyanide/Carboxylate Linker Group, *Inorganic Chemistry* 60 (2021) 12545-12554.
- [195] J. Yang, J.Y. Lee, J.Y. Ying, Phase transfer and its applications in nanotechnology, *Chemical Society Reviews* 40 (2011) 1672-1696.